Resolution Studies
of a
GEM-Based TPC

Von der Fakultät für Mathematik, Informatik und
Naturwissenschaften der Rheinisch-Westfälischen
Technischen Hochschule Aachen zur Erlangung
des akademischen Grades eines Doktors der
Naturwissenschaften genehmigte Dissertation

vorgelegt von

Diplom-Physiker Martin Killenberg

aus Soest

Berichter: Prof. Dr. Joachim Mnich
Prof. Dr. Achim Stahl

Tag der mündlichen Prüfung: 15. Dezember 2006

Diese Dissertation ist auf den Internetseiten
der Hochschulbibliothek online verfügbar.

Abstract

The next large collider to be build after the Large Hadron Collider LHC is the electron-positron International Linear Collider ILC. Both collider concepts complement each other. The LHC, reaching centre of mass energies of up to 14 TeV, has a high discovery potential, while the ILC with its well known initial state allows high precision measurements.

A detector at the ILC will need a finely segmented calorimeter and a tracking detector with high efficiency and momentum resolution, as well as good particle identification. Currently there are four different concept studies trying to optimise the detector for the requirements at the ILC. In three of these detector concepts a time projection chamber (TPC) is foreseen as the main tracking device.

A TPC allows the measurement of several hundred points per track, providing a very good tracking efficiency. With only 3 % of a radiation length in the barrel region, the amount of material introduced into the detector is small compared to silicon sensors. This minimises multiple scattering and improves the energy measurement in the calorimeters. The TPC also provides a good measurement of the specific energy loss $\mathrm{d}E/\mathrm{d}x$ for particle identification.

To achieve the intended spatial resolution of 100 µm, micro pattern gas detectors (MPGD) are considered for gas amplification. These devices consist of structures with a size of a few hundred µm, in contrary to an anode wire readout with a pitch of typically a few millimetres. This improves the granularity of the measurement and minimises $E \times B$ effects, resulting in an enhanced spatial and two track resolution. Furthermore the backdrift of ions into the sensitive volume of the TPC is intrinsically suppressed. This is essential, as the established method of gating away the ions after each recorded event will not work at the ILC. Due to the bunch structure there will be data from 150 bunch crossings simultaneously in the TPC. The two different MPGDs discussed for the ILC TPC are Micro-Mesh Gaseous Detectors (Micromegas) and Gas Electron Multiplier foils (GEMs).

The current thesis shows resolution studies with a TPC prototype equipped with a triple GEM readout structure. A hodoscope made up of silicon strip sensors gives a precision reference track, allowing an unbiased measurement of the spatial resolution. High statistics measurements have been conducted at the DESY test beam facility, which provides positrons with a tunable energy between 1 GeV and 6 GeV.

Using the independent measurement of the hodoscope allows systematic studies of the homogeneity of the TPC's electric field. The fluctuations of the field in the chamber's central region were found to be $\Delta E/E = 8 \cdot 10^{-3}$. Field distortions have been determined and corrected, reducing the remaining deviations to a level well below the spatial resolution of the TPC.

Abstract

One important task is to reduce the number of ions drifting back into the sensitive volume. Special GEM settings with minimised ion backdrift have been examined with respect to their influence on the spatial resolution and it was found that the spatial resolution is not degraded using these special settings.

The TPC at the ILC will be operated in high magnetic fields. Thus it is mandatory to show that the anticipated performance can be achieved in magnetic fields. The TPC prototype has been operated in a 4 T magnetic field, provided by a superconducting solenoid located at DESY Hamburg. Again the spatial resolution measured with the ion backdrift optimised settings is compared to that achieved with non-optimised settings. In both cases the measured resolution is approximately 130 µm.

Zusammenfassung

Der nächste große Beschleuniger, der nach dem Large Hadron Collider LHC gebaut werden wird, ist der Elektron-Positron Linearbeschleuniger *International Linear Collider ILC*. Die Konzepte der beiden Beschleuniger ergänzen sich gegenseitig. Der LHC erreicht Schwerpunktsenergien bis zu 14 TeV und hat ein hohes Entdeckungspotential. Der ILC hingegen erlaubt Messungen von hoher Präzision durch den gut bekannten Anfangszustand.

Ein Detektor für den ILC benötigt ein fein segmentiertes Kalorimeter, einen Spurdetektor mit hoher Effizienz und guter Impulsauflösung sowie gute Teilchenidentifikation. Vier verschiedene Detektorstudien versuchen zur Zeit, den Detektor für die Anforderungen des ILC zu optimieren. In drei dieser Detektorkonzepte ist eine Zeitprojektionskammer (Time Projection Chamber, TPC) als Hauptspurdetektor vorgesehen.

Eine TPC liefert mehrere hundert Punkte pro Spur, was eine hohe Rekonstruktionseffizienz ermöglicht. Mit nur 3 % einer Strahlungslänge im Zentralbereich ist die in den Detektor eingebrachte Materialmenge klein im Vergleich zu Siliziumsensoren. Das minimiert die Vielfachstreuung und verbessert die Energiemessung in den Kalorimetern. Außerdem bietet die TPC eine gute Messung des spezifischen Energieverlustes dE/dx, die zur Teilchenidentifikation benutzt wird.

Um die angestrebte Ortsauflösung von 100 µm zu erreichen, werden Mikrostruktur-Gasdetektoren zur Gasverstärkung untersucht. Die Strukturen dieser Detektoren haben eine Größe von einigen hundert µm, im Gegensatz zu Anodendrähten, die im Abstand von einigen Millimetern gespannt sind. Das verbessert die Genauigkeit der Messung und minimiert $E \times B$-Effekte, woraus sich eine verbesserte Orts- und Doppelspurauflösung ergibt. Außerdem wird die Rückdrift von Ionen in das sensitive Volumen den TPC unterdrückt. Das ist entscheidend, da die bewährte Methode, nach jedem aufgezeichneten Ereignis zu gaten, beim ILC nicht funktioniert. Wegen der Struktur der Teilchenpakete werden die Daten von bis zu 150 Strahlkreuzungen gleichzeitig in der TPC sein. Die beiden diskutierten Mikrostruktur-Detektoren sind Micro-Mesh Gasdetektoren (Micromegas) und Gas Electron Multiplier (GEMs).

Diese Arbeit zeigt Auflösungsstudien mit einem TPC-Prototypen, der mit einer Dreifach-GEM-Struktur ausgestattet ist. Ein Hodoskop aus Silizium-Streifen-Sensoren liefert eine präzise Referenzspur, was eine unbeeinflusste Messung der Ortsauflösung ermöglicht. Am DESY-Teststrahl, der Positronen mit einer Energie zwischen 1 GeV und 6 GeV liefert, wurden Messungen mit hoher Statistik durchgeführt.

Die unabhängige Messung mit dem Hodoskop erlaubt systematische Studien der Feldhomogenität der TPC. Die ermittelten Feldfluktuationen im Zentralbereich der

Zusammenfassung

Kammer sind $\Delta E/E = 8 \cdot 10^{-3}$. Feldverzerrungen wurden gemessen und korrigiert. Die verbleibenden Abweichungen konnten so auf ein Niveau deutlich unter der Ortsauflösung der TPC reduziert werden.

Eine wichtige Aufgabe ist es, die Anzahl der Ionen zu reduzieren, die in das sensitive Volumen der TPC zurückdriften. Spezielle Einstellungen der GEM-Spannungen zur Minimierung der Ionenrückdrift wurden in Bezug auf ihren Einfluss auf die Ortsauflösung untersucht. Es wurde keine Beeinträchtigung der Auflösung durch diese speziellen Einstellungen festgestellt.

Die TPC wird am ILC in einem hohen Magnetfeld betrieben. Deshalb ist es notwendig zu zeigen, dass die angestrebte Auflösung auch im Magnetfeld erreicht wird. Die Prototyp-TPC wurde in einem 4 T Magnetfeld betrieben, das mit einem supraleitenden Solenoidmagneten am DESY in Hamburg erzeugt wurde. Auch hier wurde die Ortsauflösung der ionenrückdrift-optimierten Einstellung mit derjenigen verglichen, die mit den nicht optimierten Einstellungen erreicht wurde. In beiden Fällen liegt die gemessene Auflösung bei etwa 130 µm.

Contents

Contents

Contents

1 Introduction

Particle physics tries to answer the questions "What is matter made of?" and "What are the fundamental forces?". At the beginning of the 20th century it was found that matter is composed of particles which can chemically not be divided any more. They were named atoms, a term originating from the Greek word *atomos*, which means indivisible. However, it was later discovered that atoms are not indivisible, but consist of a nucleus and electrons. The nucleus is made up of neutrons and protons, and even these have a substructure, being composed of quarks and gluons. But is this the final word?

Within the last decades, particle physics has developed a consistent theory to describe the constituents of matter and the forces acting between them up to energies of the order of 100 GeV: The Standard Model of particle physics. This chapter gives an overview of the current understanding of elementary particles. More comprehensive introductions to particle physics and quantum field theories can be found in [1] and [2], for instance.

1.1 The Standard Model of Particle Physics

In the Standard Model of particle physics the constituents of matter are fermions, i. e. particles with spin 1/2. All interactions of particles can be described by three fundamental forces: The strong force, the electroweak force and gravitation. The Standard Model is based on three local gauge symmetries [3]. Quantum chromodynamics (QCD) describes the strong force, while the electromagnetic and the weak force are explained by the GSW theory, named after S. L. Glashow, A. Salam and S. Weinberg, who were rewarded the Nobel prize in 1979 for this theory [4][5][6]. Gravitation is not included in the Standard Model, there is no quantum field theory available for gravitation yet. In locally gauge invariant field theories the interaction between fermions is implemented by the exchange of gauge bosons. For every particle there is an anti-particle.

The fundamental fermions can be divided into two groups: leptons and quarks. The electroweak force and gravitation act on all of them, while the strong force only affects quarks. Leptons and quarks are grouped into three generations, where the second and third generation are almost exact copies of the first one. All quantum numbers are identical, only the mass of the fermions increases with the generation number. In total there are 6 fermions and 6 quarks. Their names and properties are shown in table 1.1.

Leptons

Generation	Name	Symbol	Charge [e]	Mass [MeV]
1	Electron neutrino	ν_e	0	$< 2 \cdot 10^{-6}$
	Electron	e	-1	0.511
2	Muon neutrino	ν_μ	0	< 0.19
	Muon	μ	-1	105.7
3	Tau neutrino	ν_τ	0	< 18.2
	Tau	τ	-1	1777

Quarks

Generation	Name	Symbol	Charge [e]	Mass [MeV]
1	Up	u	$+2/3$	1.5–3.0
	Down	d	$-1/3$	3–7
2	Charm	c	$+2/3$	$(1.25 \pm 0.09) \cdot 10^3$
	Strange	s	$-1/3$	95 ± 25
3	Top	t	$+2/3$	$(174.2 \pm 3.3) \cdot 10^3$
	Bottom	b	$-1/3$	$(4.20 \pm 0.07) \cdot 10^3$

Table 1.1: The fundamental fermions of the Standard Model [7]. As quarks are not freely observable, their masses depend on the theoretical model used to determine them. In this case the current masses in the $\overline{\text{MS}}$ scheme are given [7]. The top quark mass is determined from direct measurements at Tevatron.

Force	Gauge Boson	Mass [GeV]	Charge [e]
Strong	8 Gluons g	0	0
Electroweak	Photon γ	0	0
	$W^{\pm}$	80.403 ± 0.029	± 1
	Z	91.1876 ± 0.0021	0

Table 1.2: The force-mediating gauge bosons of the Standard Model [7].

1.1.1 Quantum Chromodynamics

The charge of the strong force has three states, called red, green and blue[1]. They are bound together with eight massless, coloured gauge bosons called gluons. As the gluons themselves have colour charge, there is gluon self-interaction. Free quarks cannot be observed. If two bound quarks are separated from each other, the energy content of the interchanging gluons grows with the distance. If the energy content is large enough to create a new quark-antiquark pair, the bound state is split into two, the particle hadronises. This results in the observation of so-called *hadron jets*. As the quarks are not freely observable, their masses cannot be measured directly (except for the top quark, which decays before hadronising). The masses in table 1.1 are the current quark masses [7].

1.1.2 The GSW Theory

The GSW theory is a unified theory of the electromagnetic and the weak force. Q is the electric charge, the gauge boson of the electromagnetic force is the photon γ. For the weak force the exchange bosons are called W^+, W^- and Z. All gauge bosons of the Standard Model are listed in table 1.2.

It is found that the charged weak current $W^{\pm}$ only acts on fermions with left chirality. The left-chiral quarks and leptons of each generation represent a doublet of the weak isospin T, while the right-chiral fermions are isospin singlets. The neutral current Z, however, does couple to charged, right-chiral fermions, but with a different coupling strength. This is taken into account by introducing the weak hypercharge Y, which is defined from the electric charge Q and the third component of the weak isospin T_3 by the Gell-Mann-Nishijima relation:

$$Q = T_3 + \frac{Y}{2}$$

Table 1.3 gives an overview of the electroweak multiplets and their quantum num-

---

[1]The names red, green and blue for the charges of the strong force, and the resulting name *chromodynamics*, have been chosen in analogy to the colour theory, where red, green and blue combined yields the colour white. In quantum chromodynamics, the three different states together result in a colour neutral object. A proton for instance consists of three quarks of different colour, but it carries no net colour charge.

	Generation			Quantum Numbers			
	1	2	3	Q	T	T_3	Y
Leptons	$\begin{pmatrix} \nu_e \\ e \end{pmatrix}_{\mathrm{L}}$	$\begin{pmatrix} \nu_\mu \\ \mu \end{pmatrix}_{\mathrm{L}}$	$\begin{pmatrix} \nu_\tau \\ \tau \end{pmatrix}_{\mathrm{L}}$	0 -1	1/2 1/2	+1/2 -1/2	-1 -1
	e_{R}	μ_{R}	τ_{R}	-1	0	0	-2
Quarks	$\begin{pmatrix} u \\ d' \end{pmatrix}_{\mathrm{L}}$	$\begin{pmatrix} c \\ s' \end{pmatrix}_{\mathrm{L}}$	$\begin{pmatrix} t \\ b' \end{pmatrix}_{\mathrm{L}}$	+2/3 -1/3	1/2 1/2	+1/2 -1/2	+1/3 +1/3
	u_{R}	c_{R}	t_{R}	+2/3	0	0	+4/3
	d_{R}	s_{R}	b_{R}	-1/3	0	0	-2/3

Table 1.3: The electroweak multiplets and their quantum numbers.[2]

bers. Note that the weak quark eigenstates d', s' and b' are not identical to the quarks' mass eigenstates d, s and b. They are connected by the Cabibbo-Kobayashi-Maskawa matrix V_{CKM}:

$$\begin{pmatrix} d' \\ s' \\ b' \end{pmatrix} = V_{\mathrm{CKM}} \begin{pmatrix} d \\ s \\ b \end{pmatrix}$$

At low energies the electromagnetic component is much stronger than the other interactions of the electroweak force. This is where the name *weak* force originates from. It is due to the fact that the W and Z bosons are very heavy, while the photon is massless. For energies in the range of the W and Z boson masses the electromagnetic and the weak force reach the same order of magnitude, as figure 1.1 shows.

Breaking of the Electroweak Symmetry

In local gauge symmetries all force-mediating bosons should be massless. However, the weak gauge bosons W and Z are very heavy. Local gauge symmetry can be conserved by the Higgs mechanism [11][12][13], which introduces an additional field with a non-vanishing vacuum expectation value. This gives mass to the W and Z bosons and predicts a new scalar boson, the so called Higgs particle.

The Higgs boson is the only particle of the Standard Model which has not been discovered yet. Direct searches at LEP have excluded Higgs masses below 114 GeV [14], while constraints from electroweak precision measurements predict that a standard model Higgs is below 194 GeV [7].

---

[2]Neutrino mixing experiments have shown that neutrinos are not massless [8][9]. This gives existence to right-chiral neutrinos. They do not participate in weak interactions, as they carry neither weak isospin nor charge. Note that the weak eigenstates are not identical to the mass eigenstates [7].
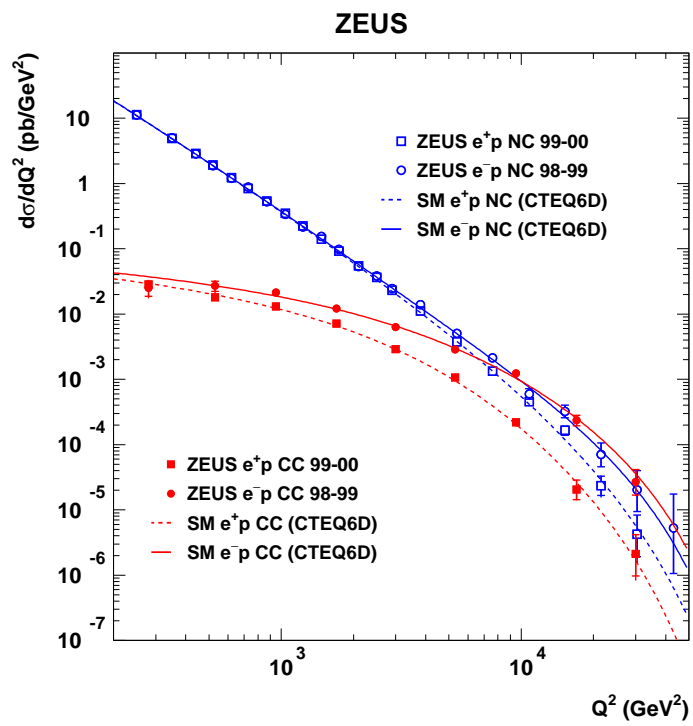
Figure 1.1: Unification of the weak and the electromagnetic force: The cross sections for charged and neutral currents become equal for high momentum transfers [10].

1.1.3 Beyond the Standard Model

The Standard Model is very successful and has been consistent with all precision measurements up to now. But in the energy range of order 1 TeV new physics is expected. Besides, the Standard Model still leaves unanswered questions. All the fermion masses for instance are free parameters, which have to be measured and are not predicted by the theory. And why are there exactly three generations of quarks and leptons? Looking at cosmology one finds that only 4 % of the matter in the universe are made up of baryons which can be observed, while 22 % are dark matter. The latter can only be seen by its gravitational effects, but we do not know what it is made of. The remaining 74 % are called dark energy, about which we know even less. A last point to be mentioned is gravitation, which is not described by the Standard Model at all.

Particle physics tries to find a common description of all particles and forces. Grand Unified Theories (GUTs), combining the strong and the electroweak force, are a next step in this direction. The most popular model is called Supersymmetry (SUSY) [15]. In supersymmetric theories every fermion has a bosonic super-partner, and vice versa, introducing a symmetry between fermions and bosons. The lightest stable SUSY particle is a good candidate for dark matter. Even incorporating gravitation into supersymmetric models is possible (supergravity) [16].

Most SUSY models predict that the lightest supersymmetric particles should be visible in the energy range of LHC and ILC.

2 The International Linear Collider

Throughout the last decades it has emerged that hadronic and leptonic colliders complement each other very well in the search for new particles at the energy frontier. Hadronic machines provide the highest possible energies available with the current accelerator technology, while e^+e^- colliders allow precision measurements due to their well known initial state of interactions.

The next large accelerator currently under construction is the Large Hadron Collider (LHC) at CERN in Geneva. It is a proton-proton collider with a centre-of-mass energy of 14 TeV. This accelerator will be the discovery machine of the next decade. There is consensus that the next accelerator built after the LHC will be an e^+e^- collider. It is very desirable to operate both machines in parallel to take maximum advantage of the complementing technologies.

Particle accelerators have often been implemented as storage rings, due to the efficient usage of the accelerating structures and the possibility to collide the particle bunches circling around over and over again. However, a charged particle on a curved trajectory emits synchrotron radiation. The energy loss due to this radiation rises with the fourth power of the energy E. It is suppressed only by the first power of the radius R, but with the forth power of the particle mass m:

$$\Delta E \sim \left(\frac{E}{m}\right)^4 \cdot \frac{1}{R}$$

This is why circular electron-positron machines were the first to face this problem, while for the hadrons, three orders of magnitude heavier than the leptons, synchrotron radiation is not an issue yet. The Large Electron Positron Collider LEP, operated at CERN until the end of 2000, probably was the e^+e^- storage ring with the highest reasonable energy, reaching up to 209 GeV centre-of-mass energy. An e^+e^- accelerator at the TeV scale will be realised as a linear collider.

Originally there were three approaches: The Global Linear Collider (GLC)[1] in Japan [17], the US American Next Linear Collider (NLC) [18] and the TeV Energy Superconducting Linear Accelerator (TESLA) [19] in Europe. Both GLC and NLC were based on normal conducting cavities, while superconducting niobium cavities have been developed for TESLA.

In 2004 the International Technology Recommendation Panel proposed to operate the linear collider on the basis of the superconducting accelerator technology of the TESLA project [20]. After this decision the different approaches in America, Asia and Europe have joint to build the International Linear Collider (ILC) project [21].

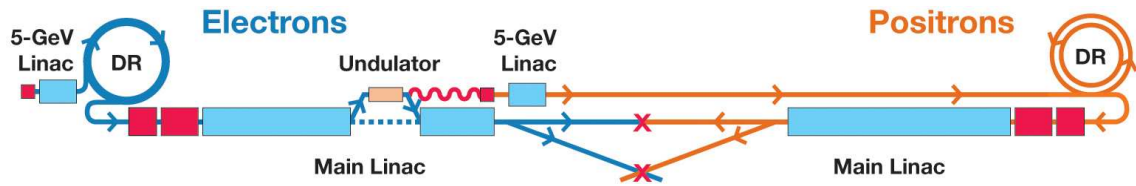[1]Until march 2003 the project was named Japanese Linear Collider (JLC)

Figure 2.1: A schematic layout of the International Linear Collider [21].

The ILC will be a truly global project with R&D from all over the world and international funding. To coordinate all activities, the Global Design Effort (GDE) has been established. A conceptual design report (CDR) is planned for the end of 2006, followed by a technical design report (TDR) in 2008.

2.1 The Accelerator

In a first phase the ILC will deliver a centre-of-mass energy of 500 GeV with an upgrade option to 1 TeV [21]. The electron and positron beams both are polarised. The ILC provides two interaction points, both at a crossing angle of 14 mrad.

Figure 2.1 shows the baseline design of the ILC. The two main accelerators have a length of 10 km each. The overall length will be about 31 km.

The electrons from the polarised electron source are accelerated to 5 GeV before they are injected into the electron damping ring (DR). The damping rings have a circumference of 6 km. By emitting synchrotron radiation in the DR, the emittance of the beam is reduced to allow the small beam size required to achieve the anticipated luminosity of $\mathcal{L} = 2 \times 10^{34}$ cm^{-2}s^{-1}.

To produce positrons, the electron beam from the main linac is directed through a 200 m long undulator. The emitted photons hit the positron production target, and the positions are likewise accelerated to 5 GeV before entering the damping rings. A thin target allows the creation of a polarised positron beam.

The main linac consists of superconducting niobium cavities. They are operated at a gradient of 31.5 MV/m in the first phase with a centre-of-mass energy of 500 GeV. To achieve 1 TeV centre-of-mass energy in the second phase, the acceleration gradient has to be increased to 36 MV/m. In addition, the tunnel will have to be extended. The accelerator is operated in a pulsed mode, providing a bunch train with 2820 particle bunches at a rate of 5 Hz. The spacing of the individual bunches within the train is 308 ns with a bunch length of 500 µm. Each bunch carries 2×10^{10} electrons or positrons.

2.2 Physics at the ILC

The Large Hadron Collider LHC with a centre-of-mass energy of 14 TeV will start operation in the end of 2007. If there is a Higgs boson or Supersymmetry at an energy of $\mathcal{O}(1$ TeV$)$, the LHC will most likely discover them. The task of the ILC

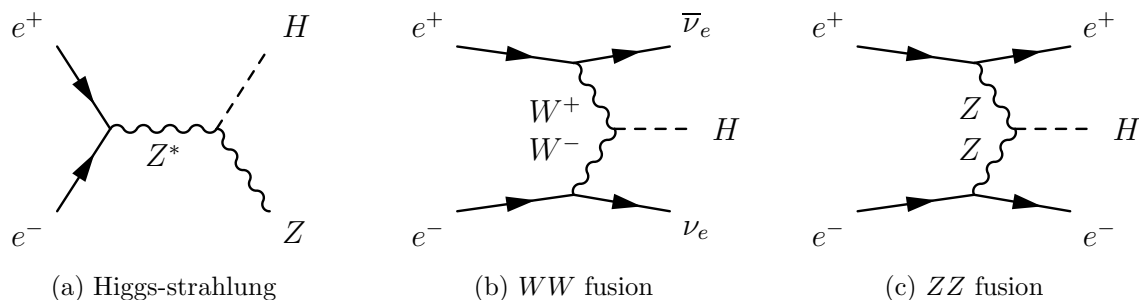(a) Higgs-strahlung   (b) WW fusion   (c) ZZ fusion

Figure 2.2: The three main Higgs production processes at e^+e^- colliders.

will be to precisely measure their properties. But not only newly discovered particles are to be addressed. The ILC will be the first e^+e^- collider to reach the $t\bar{t}$ production threshold at around 350 GeV. This allows to precisely measure the mass and the electroweak properties of the top quark.

Higgs Physics

If a Higgs boson exists, the task of the ILC will be to exactly determine its mass, lifetime, production cross section and decay channels. The main production processes at an e^+e^- collider are Higgs-strahlung and WW fusion (figure 2.2). At the production threshold the dominating process is Higgs-strahlung (figure 2.2(a)). A highly virtual Z boson produced in the e^+e^- annihilation radiates a Higgs boson. This process allows to reconstruct the Higgs mass independently of the Higgs decay, only from the Z recoil mass. A light Higgs predominantly decays into $b\bar{b}$. The Z can decay into quarks or leptons. Especially the channel $HZ \to b\bar{b}\mu^+\mu^-$ has a clear signature and low background. Figure 2.3 shows the number of expected events against the reconstructed Z recoil mass for a Standard Model Higgs with $m = 120$ GeV.

Not only the Higgs mass, but also the couplings of the Higgs will be measured. The Higgs couplings to the heavy gauge bosons W and Z are determined from the respective production cross sections. For a known Higgs mass the Standard Model predicts the branching ratios of the decay mode. The measurement of these cross sections allows to test the Standard Model and is sensitive to new physics. For higher energies the determination of the Higgs self coupling is possible.

Supersymmetry

Supersymmetry as the most popular extension of the Standard Model certainly is of major interest at the ILC. The lightest SUSY particles are predicted to be within the energy range of the ILC. It will be possible to identify the SUSY particles and determine their quantum numbers, not only from radiative corrections to the Standard Model but also from explicit energy scans around the production threshold. This is possible due to the well known initial state and the possibility to polarise
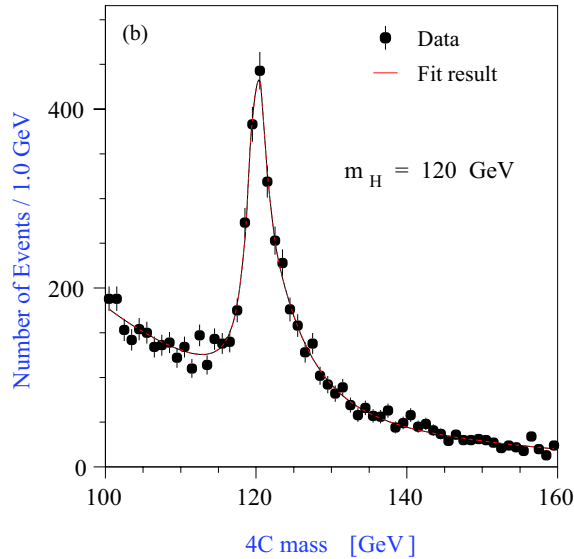
Figure 2.3: The Higgs boson mass reconstructed in the channel $HZ \rightarrow q\bar{q}l^+l^-$ for a Higgs mass of 120 GeV [22].

electrons as well as positrons. The ILC will also be able to test whether the lightest supersymmetric particle really is the sought-after candidate for dark matter.

2.3 A Detector for the ILC

2.3.1 Overview

The design of ILC detectors is driven by physics needs. To meet the requirements, all sub-detector components have to be improved compared to previous experiments. The measurement of the Higgs mass as described in section 2.2 for instance requires the momentum of electrons or muons to be measured as precisely as possible to reconstruct the Z recoil mass. With an overall track momentum resolution of $\delta(1/p_t) \leq 5 \times 10^{-5}\ (\mathrm{GeV}/c)^{-1}$ the width of the signal is mainly determined by initial state radiation and beamstrahlung, and not by the detector resolution [23]. Efficient and reliable b-tagging in the vertex detector enables the separation of b jets and c jets. As the Higgs is identified from the Z recoil, this allows to determine the $H \rightarrow b\bar{b}$ and $H \rightarrow c\bar{c}$ branching ratios. To separate Z and W in hadronic decays, an excellent jet-energy resolution is needed. This will be implemented by the particle flow concept, which tries to measure each individual particle as precisely as possible, or by the dual readout scheme based on a fibre sampling calorimeter [24].

To optimise the design, many aspects have to be taken into account. A large tracker for instance improves the tracking resolution, but it also increases the size of the calorimeter. A large high resolution calorimeter on the other hand is expensive and the number of readout channels technically feasible is limited. A full silicon tracker has a good spatial resolution, but it introduces a lot of material inside the

calorimeters. A TPC as main tracker, however, has a low material budget and gives a good measurement of the specific energy loss dE/dx, but the spatial resolution is limited.

Currently there are four different concept studies trying to optimise the detector design, with emphasis on different aspects:

- The Global Large Detector (GLD)[25][26]

- The Large Detector Concept (LDC)[27][28]

- The Silicon Detector Concept (SiD)[29][30]

- The 4th Detector Concept (4th)[31][24]

All concepts, except for the SiD, have a TPC as main tracking device. As an example the LDC will be explained in detail.

2.3.2 The Large Detector Concept

The layout of the LDC is shown in figure 2.4. An enlarged view of the tracking system can be found in figure 2.5.

- The innermost detector is a five layer silicon pixel vertex detector (VTX), followed by two layers of silicon strip sensors as intermediate tracker (SIT) between VTX and the TPC.

- In the forward region there are seven forward tracking disks (FTD). The first three disks are silicon pixel detectors, while the others are double sided silicon strip sensors.

- The main tracking device is a large time projection chamber (TPC), which allows 200 individually measured points on each track.

- A silicon external tracker (SET) around the barrel of the TPC and an end-cap tracking detector (ETD) give an additional high precision tracking point between TPC and calorimeter.

- The silicon-tungsten electromagnetic calorimeter (ECAL) has a cell size of $1{\times}1$ cm^2 and provides up to 30 samples in radial direction.

- The hadronic calorimeter (HCAL) is made up of an iron-scintillator sandwich and is segmented into $3{\times}3$ cm^2 cells.

- The superconducting magnet encloses the HCAL and provides a magnetic field of 4 T.

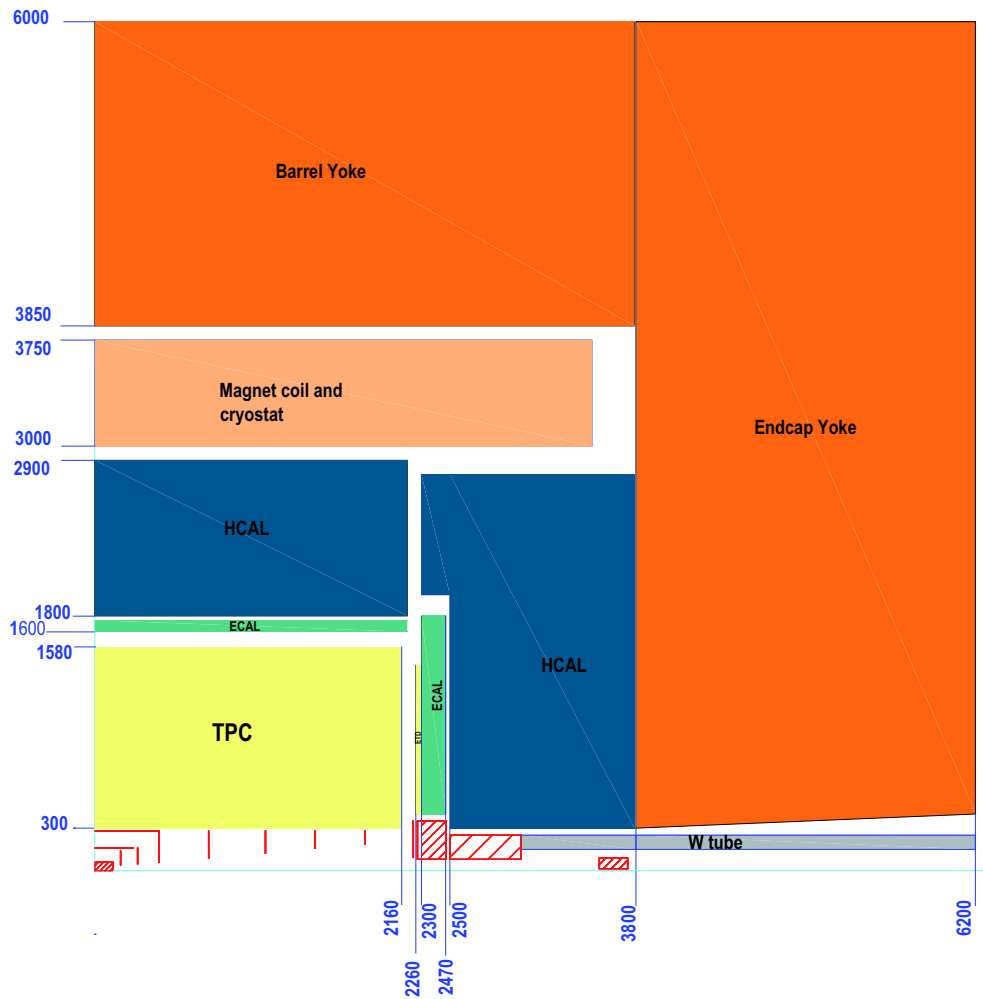- The iron return yoke is instrumented with a muon tracking system.

Figure 2.4: Sketch of the Large Detector Concept. The central tracking component is a TPC. All dimensions are in mm. [28]
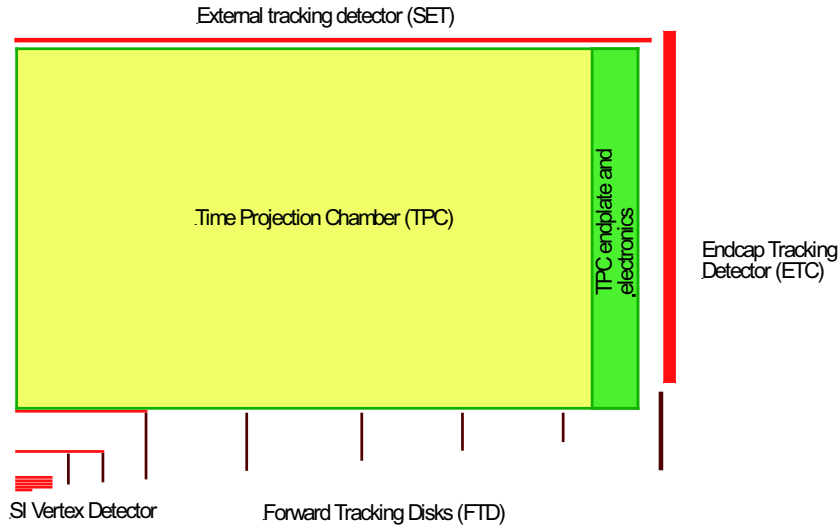
External tracking detector (SET)

Time Projection Chamber (TPC)

TPC endplate and electronics

Endcap Tracking Detector (ETC)

SI Vertex Detector

Forward Tracking Disks (FTD)

Figure 2.5: Enlarged view of the LDC tracking system [28].

The TPC

The TPC as the main tracking component of the LDC covers a radius from 300 mm to 1580 mm and has a half length of 2160 mm. Two half TPCs are mounted symmetrically on both sides of a central cathode. Table 2.1 gives an overview of the LDC TPC performance.

Many TPCs have successfully been operated in large experiments, like ALEPH [32] and DELPHI [33] at LEP. Currently a TPC is used at the STAR experiment [34] at the RHIC accelerator. All these TPCs are based on anode wires as gas amplification structures.

To improve the spatial resolution, it is planned to replace the anode wires by micro pattern gas detectors. There are two different systems available: Micro-Mesh Gaseous Detectors (Micromegas) [35] and Gas Electron Multipliers (GEMs) [36]. A Micromegas based TPC is planned for the near detector of the T2K experiment [37] at JPARK in Tokai, Japan. This thesis studies the spatial resolution of a GEM based TPC prototype.

Momentum resolution	$\delta(1/p_t) \approx 10^{-4}/(\text{GeV}/c)$ (TPC only)
Material budget	$< 0.03 \; X_0$ to outer field cage in r
	$< 0.30 \; X_0$ for readout endcap in z
Number of readout pads	$> \; 10^6$ per endcap
Pad size	$\approx 1 \times 6 \; \text{mm}^2$
Single point resolution in r-φ	$\approx 100 \; \mu\text{m}$
Single point resolution in r-z	$\approx 0.5 \; \text{mm}$
Two-track resolution in r-φ	$< 2 \; \text{mm}$
Two-track resolution in r-z	$< 5 \; \text{mm}$
$\mathrm{d}E/\mathrm{d}x$ resolution	$\approx 5 \; \%$
Field homogeneity	$\Delta E/E \leq 10^{-4}$
Tracking efficiency	$> 98 \; \%$ for $\cos\theta < 0.9$

Table 2.1: Performance requirements for the TPC in the Large Detector Concept [28].

3 Working Principle of a TPC

The *time projection chamber* (TPC) was introduced by D. R. Nygren in 1974 [38]. It is a large drift chamber with a homogeneous electric field between a drift cathode and a readout structure, which makes up the anode of the drift volume. To provide a good homogeneity of the drift field, the shell of the TPC is made up of a *field cage*. Strips of conducting material are equidistantly placed between cathode and anode, for example etched into a copper or aluminium coating of a Kapton® foil. A voltage divider chain of resistors between cathode and anode puts each of these strips to a defined potential, corresponding to the equipotential surfaces of a homogeneous field.

The working principle of a TPC is shown in figure 3.1. A charged particle passing the chamber leaves ionised atoms and free electrons along its trajectory. In the electric field the ions drift towards the cathode, the electrons towards the anode. Here the projection of the track is detected on a two-dimensionally segmented pad plane. The third spatial coordinate can be determined by measuring the time which the electrons need to drift to the readout plane. In the homogeneous field the drift velocity v_{drift} is constant, so the z coordinate can simply be calculated from the difference between the time of the particle passage t_0 and the time of the signal detection t_1 :

$$z = (t_1 - t_0)v_{\mathrm{drift}}$$

Before the signal is detected on the pads, it has to be amplified. This is done by gas amplification, using either wires or micro pattern gas detectors. Gas amplification is a crucial part of the TPC, as well as the primary ionisation process and the drift, so these topics will be discussed in detail in the following sections. For further reading see reference [39], for instance.

3.1 Ionisation in Gas

A highly energetic, charged particle traversing a gas volume collides with the gas molecules, causing excitation and ionisation. This leaves ionised gas atoms and free electrons along the particle trajectory.
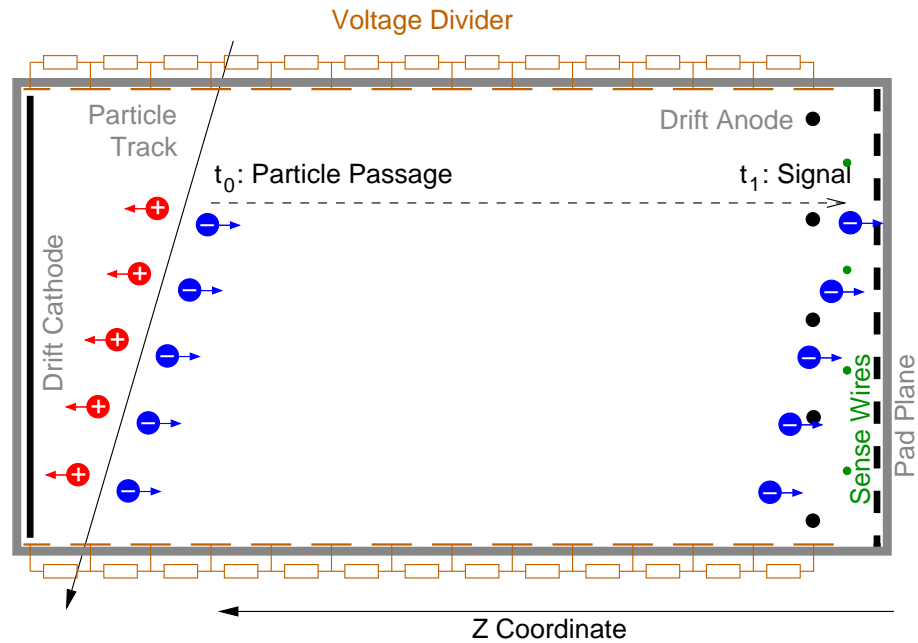
Figure 3.1: The working principle of a TPC: A particle traversing the chamber ionises the gas along its trajectory. The produced electrons drift to the readout. The projection onto the pad plane gives a two-dimensional measurement. Determining the time between particle transition and signal detection allows to calculate the z coordinate, perpendicular to the pad plane: $z = (t_1 - t_0)v_{\text{drift}}$. This allows a three-dimensional track reconstruction. The field homogeneity between cathode and anode is ensured by the field cage. In this sketch the drift anode consists of wires running perpendicular to the drawing plane.
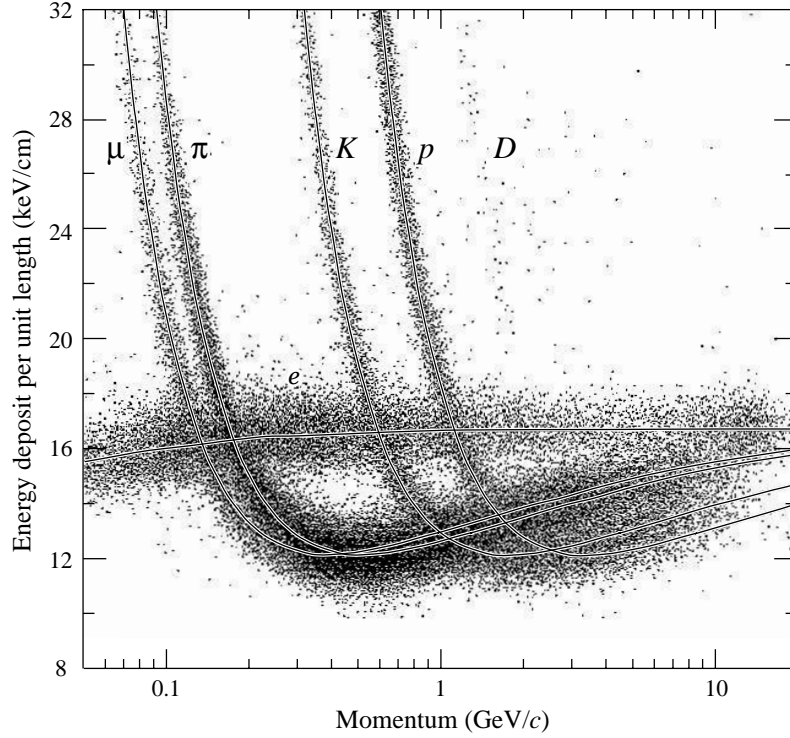
Figure 3.2: Specific energy loss of highly energetic particles, measured with the PEP4/9 TPC in Ar/CH$_4$ 80/20 gas at 8.5 atm pressure [7].

The energy loss along the path $\mathrm{d}E/\mathrm{d}x$ is approximately described by the Bethe-Bloch formula:

$$-\frac{\mathrm{d}E}{\mathrm{d}x} \; = \; 4\pi N_A\, r_e^2\, m_e\, c^2 \rho \;\frac{Z}{A} z^2 \frac{1}{\beta^2} \left(\ln\left(\frac{2m_e\, c^2 \gamma^2 \beta^2 T_{\max}}{I^2} \right) - \beta^2 - \frac{\delta}{2} \right)$$

(N_A: Avogadro's constant; $r_e = e^2/\left(4\pi\epsilon_0\, m_e\, c^2\right)$: classical electron radius; m_e: electron mass; ρ: absorber density; Z, A: atomic number and atomic mass of the absorbing material; z: charge of the travelling particle in units of e; $T_{\max}$: maximum kinetic energy which can be transferred to a free electron in one collision; I: mean excitation energy of an absorber atom; δ: density effect correction for highly relativistic particles)

For small energies, $\mathrm{d}E/\mathrm{d}x$ is proportional to $1/\beta^2$ and reaches a minimum around $\beta\gamma \approx 4$. Particles in this energy range are called *minimum ionising particles*. For higher energies the energy deposit rises due to the logarithmic term $\sim \ln\left(\gamma^2\beta^2\right)$.

For electrons and positrons the approximation of the Bethe-Bloch formula is not valid. This is due to the small electron mass and the fact that the main scattering partners in the absorber are electrons. The cross section for electron-electron scattering is different than for scattering processes of heavier particles with electrons.

Figure 3.2 shows the specific energy loss for different particles in gas. Knowing the particle momentum, this distribution allows particle identification in a certain energy range by measuring $\mathrm{d}E/\mathrm{d}x$.

The Bethe-Bloch formula only describes the mean energy loss per unit length. For short absorber distances however (a few centimetres of gas at atmospheric pressure for instance), the actual energy deposition follows a Landau distribution [40]. This distribution is asymmetric and has a tail towards higher energies. The energy deposition is non-continuous and has large fluctuations, because the energy transferred to an absorber electron in a single collision can be very high. Towards longer absorber distances or averaging over many measurements, the distribution becomes more and more Gaussian shaped, according to the central limit theorem.

3.2 Drift and Diffusion in Gases

Applying an electric field to the detector volume causes the ions and electrons from the ionisation process to move in different directions, according to their charge. This separates the electrons from the gas ions and prevents them from recombining. The positively charged gas ions start drifting towards the cathode, the electrons towards the anode. Here the electron signal is amplified and read out.

In a TPC the electrons drift long distances before detection ($\mathcal{O}(1\,\mathrm{m})$), so this section will give a closer look at drift and diffusion.

3.2.1 Drift of Electrons

The electrons are accelerated by the electric field E until their next impact with a gas molecule. In the collision the electron is scattered and looses energy. Averaging over many collisions, the mean energy loss equals the energy gain in the acceleration. Macroscopically this leads to a motion with a mean drift velocity:

$$v_{\mathrm{drift}}^- = \frac{e}{m_e}\tau E$$

Here e and m_e are the electron charge and mass, τ is the mean time between two collisions. The latter is determined by the cross section σ and the energy loss per collision.

The collision cross section has a characteristic minimum for a specific particle energy $\mathcal{E}$, for argon at $\mathcal{E} \simeq 0.25$ eV for instance. This phenomenon is known as Ramsauer effect [41] and appears if the wavelength of the electron is in the same range as the molecule radius [42]. The minimum in the cross section leads to a maximum in τ, and thus to a maximum in the drift velocity.

The energy loss per collision strongly depends on the excitation threshold of the gas. For the noble gas Argon it is 11.5 eV, while for quencher gases[1] with additional rotational states it is much lower, 0.03 eV for methane for instance. Therefore the drift velocity and the position of the maximum depend on the gas mixture [43].

Figure 3.3 shows the electron drift velocity versus the electric field for the gases used in the measurements of the present work.

---

[1]Quenchers are added to the gas mixture to allow stable gas amplification, see section 3.3.
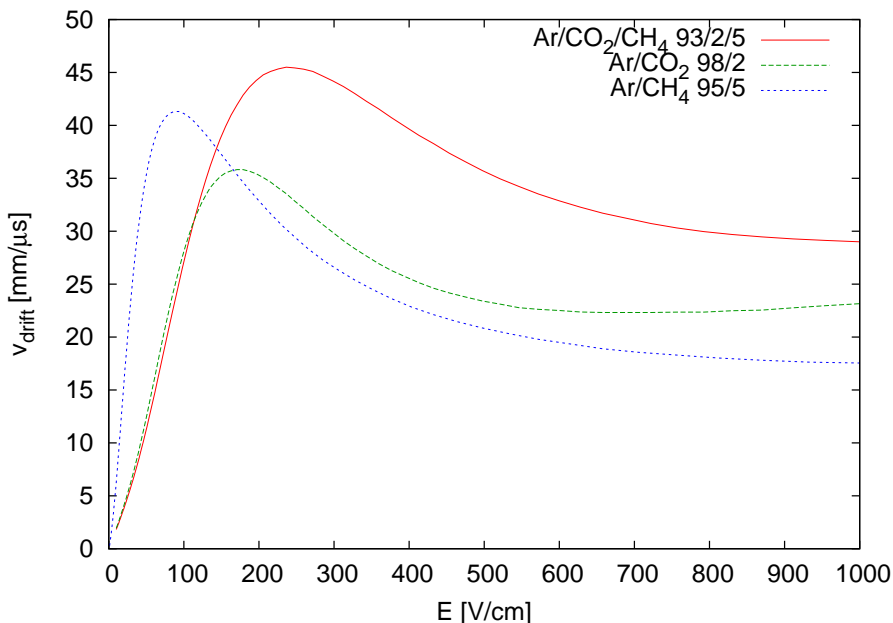
Figure 3.3: Drift velocity as function of the electric field for different gas mixtures (`Magboltz` [44] simulation).

Usually a TPC is operated at the maximal drift velocity, because here the first derivative is zero and the drift velocity does not change for small variations of the electric field.

3.2.2 Drift of Ions

Ions have much larger masses than electrons. For typical drift fields in time projection chambers, the energy gain between two collisions is of the order or below the thermal energy of the gas molecules at room temperature. This causes the ion mobility to be independent of the electric field. Thus the drift velocity is proportional to E:

$$v_{\mathrm{drift}}^+ = \mu^+ E$$

Due to the high mass, the drift velocity for ions is by a factor of $\mathcal{O}(10^{-4})$ smaller than for electrons. Table 3.1 shows the measured mobilities of noble gas ions in their parent gas. Ions can exchange electrons with neutral atoms, transferring the ionisation to another molecule. This changes the ion mobility. In gas mixtures, molecules of a different gas component with a different cross section can be ionised by this effect, also having an impact on the mobility. But again, the mobility only depends on the gas mixture, not on the electric field.

Gas	Ion	Mobility
		[cm^2 V^{-1} s^{-1}]
He	He$^+$	10.40 $\pm$ 0.10
Ne	Ne$^+$	4.14 $\pm$ 0.2
Ar	Ar$^+$	1.535 $\pm$ 0.007
Kr	Kr$^+$	0.96 $\pm$ 0.09
Xe	Xe$^+$	0.57 $\pm$ 0.05

Table 3.1: Measured ion mobilities of noble gas ions in their parent gas [39].

3.2.3 Drift in Electric and Magnetic Field

In large particle detectors for high energy physics usually a magnetic field is present. It allows to determine the momentum of the highly energetic particles from the curvature of their trajectories. As the drifting electrons and ions in the drift chamber are charged particles moving in this magnetic field, they are affected by it. Assuming the mean time between collisions τ being independent of E, the drift in electric and magnetic fields can be described by an equation of motion, known as Langevin equation:

$$m\frac{\mathrm{d}\vec{v}_{\mathrm{drift}}}{\mathrm{d}t} = e\vec{E} + e\left[\vec{v}_{\mathrm{drift}} \times \vec{B}\right] - \frac{m}{\tau}\vec{v}_{\mathrm{drift}}$$

e and m again are charge and mass of the drifting particle, the term $\frac{m}{\tau}$ corresponds to a frictional force proportional to the drift velocity.

Solving this equation for a steady state ($\frac{\mathrm{d}\vec{v}_{\mathrm{drift}}}{\mathrm{d}t} = 0$) and for times t much longer than τ gives:

$$\vec{v}_{\mathrm{drift}} = e\frac{\tau}{m}\left|\vec{E}\right|\frac{1}{1 + \omega^2\tau^2}\left(\hat{E} + \omega\tau\left[\hat{E} \times \hat{B}\right] + \omega^2\tau^2\left(\hat{E} \cdot \hat{B}\right)\hat{B}\right)$$

where $\hat{E}$ and $\hat{B}$ are the unit vectors in the direction of electric and magnetic field and $\omega = (e/m)B$ is the cyclotron frequency.

If the dimensionless term $\omega\tau$ is large, the drift direction is predominantly along $\vec{B}$. In case of $\vec{E}$ perpendicular to $\vec{B}$ the last term is zero, the particle drifts mostly along the $\hat{E} \times \hat{B}$ direction. For small $\omega\tau$ however, the drift is in $\vec{E}$ direction.

For the ILC TPC a magnetic field parallel to the electric field is planned. In this case the drift direction is not affected by the magnetic field. But neither the electric nor the magnetic field will be 100 % homogeneous, and for the long drift distances even small field distortions will have to be known to calculate the correct mapping of the particle trajectory. Especially for the high electric fields in the amplification region, $\vec{E}$ and $\vec{B}$ have an angle and can cause deviations which could degrade the spatial resolution.

3.2.4 Diffusion

The drifting electrons collide with the gas molecules and are scattered. As they are light compared to their impact partners, they are scattered isotropically. Therefore, after a few collisions the electrons in the cloud have momentum components in all directions and the electron cloud diffuses.

The density distribution of the electrons ρ_{el} satisfies the continuity equation for a conserved electron current $\vec{\Gamma}$:

$$\vec{\Gamma} = \rho_{el}\vec{v}_{drift} - D\nabla\rho_{el} = const.$$

The solution of this equation is a Gaussian density distribution with a time dependent width:

$$\rho_{el} = \left(\frac{1}{\sqrt{4\pi D t}}\right)^3 \exp\left(\frac{-r^2}{4Dt}\right)$$

Assuming a charge cloud starting at the origin and drifting along the z direction, $r^2 = x^2 + y^2 + (z - v_{drift}t)^2$ is the squared distance to the centre of the charge cloud. So the width of this distribution in any direction is

$$\sigma = \sqrt{2Dt}$$

with D being the diffusion constant.

Electric Anisotropy

The assumption of an isotropic diffusion is not correct. The energy is different for electrons in the middle of the charge cloud and at the leading edge of the distribution. If the collision cross section is a function of the electron energy, as explained in section 3.2.1, this corresponds to a change of diffusion. Detailed calculations show that the diffusion in the drift direction (*longitudinal diffusion D_{L}*) is changed, while in the perpendicular direction the diffusion (*transverse diffusion D_{T}*) behaves as in the isotropic case.

The resulting electron density distribution is

$$\rho_{el} = \left(\frac{1}{\sqrt{4\pi D_{T}t}}\right)^2 \frac{1}{\sqrt{4\pi D_{L}t}} \exp\left(-\frac{x^2 + y^2}{4D_{T}t} - \frac{(z - v_{drift}t)^2}{4D_{L}t}\right)$$

The transverse diffusion for different gases is depicted in figure 3.4.

Magnetic Anisotropy

A magnetic field also introduces an anisotropy of the diffusion. As forseen in the ILC TPC, the magnetic field is considered to be along the z axis, parallel to the drift direction. The magnetic field causes each particle trajectory to be a helix between two impacts, its projection onto the xy plane being a circle with radius
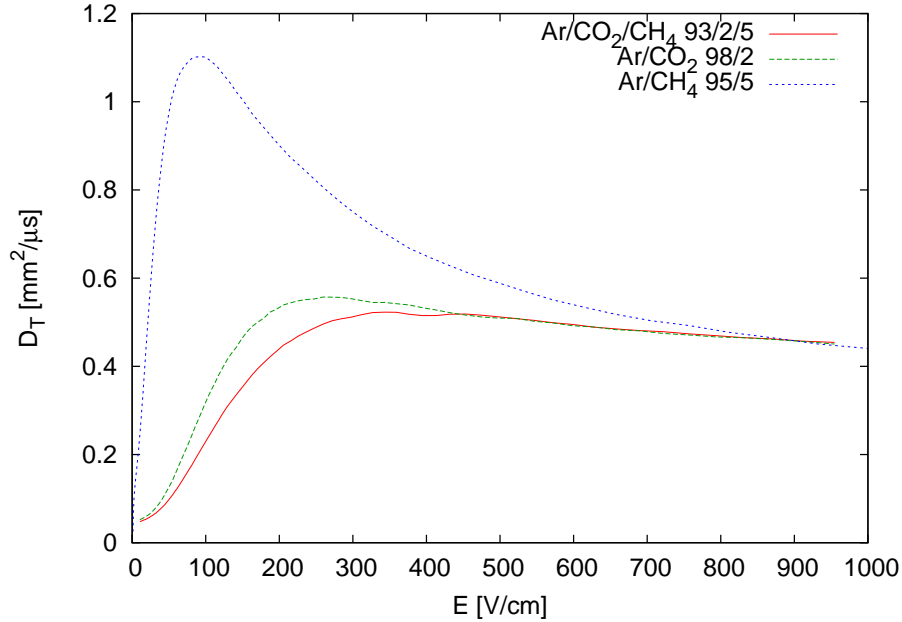
$$\rho = \frac{c}{\omega}\sin\theta$$

Figure 3.4: Transverse diffusion without magnetic field in three different gas mixtures (`Magboltz` [44] simulation).

c is the current velocity between two collisions, and θ the angle between its direction and the z axis. Again, ω is the cyclotron frequency.

Hence, the transverse components of the motion are curled up, which reduces the transverse diffusion:

$$D_\mathrm{T}(\omega) = \frac{1}{1 + \omega^2 \tau^2} D_\mathrm{T}(0)$$

The longitudinal diffusion is not changed by the magnetic field in this specific case.

3.3 Gas Amplification

For large electric fields the electrons gain sufficient energy between the collisions to ionise the gas molecules. The additional free electrons are accelerated as well and cause further ionisation, which produces an avalanche. This process is known as *gas amplification*. The number of free electrons created by the particle traversing the gas volume (*primary electrons*) is small: It is of the order of 100 electrons per cm in Argon at atmospheric pressure. Distributing these electrons across several pads would result in only a few electrons per pad. This is insufficient for an electronic amplifier to achieve a satisfactory signal to noise ratio, as the electronic noise even for the best amplifiers is of the order of a few electrons. Gas amplification provides the possibility to multiply the number of primary electrons by a factor of 10^4 to 10^5.

The number of electron-ion pairs $\mathrm{d}N$ produced per length $\mathrm{d}s$ is described by the *first Townsend coefficient* α:

$$\mathrm{d}N(s) = \alpha(s)\, N(s)\, \mathrm{d}s$$

In the strong, inhomogeneous fields of a gas amplification structure the electric field depends on s. As the ionisation cross section changes with the electric field, α also depends on s.

Assuming that the electric field is above the ionisation threshold between s_1 and s_2, the total number of electrons N after gas amplification created from the number N_0 of primary electrons is

$$
\begin{aligned}
N &= N_0 \exp \left(\int_{s_1}^{s_2} \alpha(s)\,\mathrm{d}s \right) \\
&= N_0\, G
\end{aligned}
$$

The factor $G = N/N_0$ is called gain factor.

3.3.1 Proportional Wire Readout

In proportional wire chambers the large electric fields are created near a thin wire, referred to as *amplification wire* or *sense wire*. The field amplitude goes like $1/r$, with r being the distance to the wire. In this case s_1 corresponds to the critical radius where the electric field is large enough for amplification, s_2 to the outer radius of the sense wire. Near the wire the field lines are perpendicular to its surface, which means the motion of the electrons is radial.

With increasing electric field, more and more electrons from the inner shells can be excited. Subsequently a photon is emitted, which has a long free path and can start an additional ionisation avalanche. In this case the signal is not proportional to the number of primary electrons any more. It might even lead to a continuous amplification process near the wire called *streamer*. To keep the signal proportional to the primary charge and allow stable operation for high gain factors, these photons have to be absorbed. This is achieved by adding a quencher to the noble gas. These quenchers have a high absorption cross section for the photons. Throughout the present work, carbon dioxide (CO_2) and methane (CH_4) have been used.

For a TPC, the amplification structure has often been implemented as multi-wire proportional readout. A grid of thin amplification wires is clamped near the pad plane, while an additional, grounded layer represents the anode of the drift space (figure 3.5). The sense wires are at a high positive potential. To improve the field quality in the amplification region, field wires are placed alternating with the sense wires in one plane. An electron drifting towards the readout structure passes the zero grid and enters the amplification region. The electrons are amplified at the sense wires, which induces a signal on the pads, mainly caused by the ions moving from the wires towards the pads. As the drift velocity of ions is slow compared to electrons and the time scale of the amplification process, this signal is comparatively long.
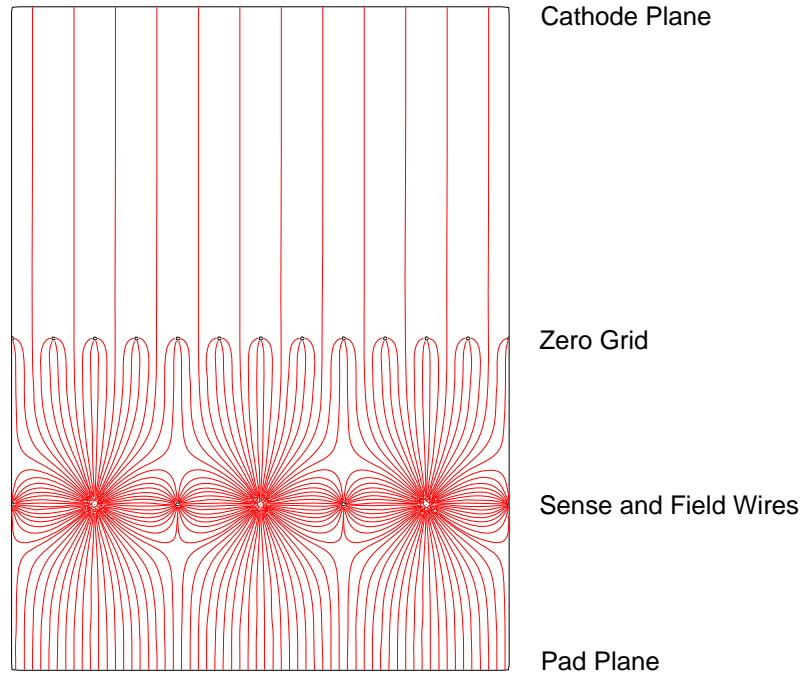
Figure 3.5: Field lines and electrode positions for a multi-wire TPC readout (simulation performed with `COMSOL Multiphysics` [45]).

3.3.2 Micro Pattern Gas Detectors

Proportional wires have been operated successfully for decades in gaseous detectors. However, they have some limitations: The wires are always oriented along one direction, which introduces an anisotropy. The minimal distance between the wires is of the order of a few millimetres, limiting the achievable position resolution. To keep the wires at their nominal position, a strong tension is needed which requires a stiff support frame. The strong electric field near the wires is not parallel to the magnetic field, which is usually perpendicular to the readout plane of a TPC. This introduces distortions known as $\vec{E} \times \vec{B}$ effects.

Most of these problems can be avoided using micro pattern gas detectors like *Micromegas* or *GEM* foils. The amplification structures of these devices have a pattern with a size of $\mathcal{O}(100\,\mu\text{m})$.

Micromegas

A **Micro**-**Me**sh **Gas**eous detector (Micromegas) [35] consists of a very fine wire mesh (micro-mesh) mounted at a small distance (50–100 µm) above a pad plane. Applying a voltage of a few hundred volts between mesh and pad plane leads to gas amplification in this region. The mesh represents the anode side of the drift region, as shown in figure 3.6. An electron drifting towards the Micromegas passes the mesh and is amplified in the high field between mesh and pads. Afterwards the electrons
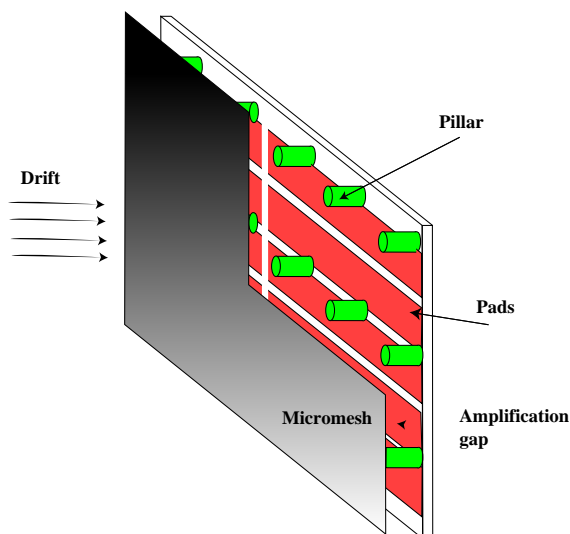
Figure 3.6: Scheme of a Micromegas detector [23].

are collected on the pad plane. To ensure a uniform gas amplification, the distance between mesh and pads has to be kept constant across the whole readout structure. This is achieved using pillars or a spacer grid. As the electron signal is much faster than the induced ion signal of wires, this device allows a better time resolution.

Gas Electron Multiplier Foils

Gas **E**lectron **M**ultipliers (GEMs) were first introduced in 1997 by CERN's Gas Detector Development Group [36]. They are made up of a usually 50 µm thick *Kapton*®[2] foil, coated with a copper layer on both sides. A pattern of holes is etched into the foil. The pitch of the pattern is of the order 100 µm. Figure 3.7(a) shows a picture of a GEM foil.

A potential difference of 300–400 V between the two copper electrodes of a GEM foil produces a high electric field in the holes, which is used for gas amplification. A GEM based amplification structure usually consists of two or three GEM foils, spaced by 1–2 mm and mounted onto a pad plane. For this detector the drift anode is represented by the surface of the uppermost GEM in the stack. To extract the electrons from one foil and transfer it to the next foil or the pad plane, an external electric field is applied. Figure 3.7(b) shows a simulation of a GEM's drift lines. Like in the case of Micromegas the electron signal is directly measured on the pads, allowing a good resolution in time.

---

[2] *Kapton*® is a polyimide foil, which is a very good electric insulator. Kapton® is a registered trademark of DuPont incorporation.
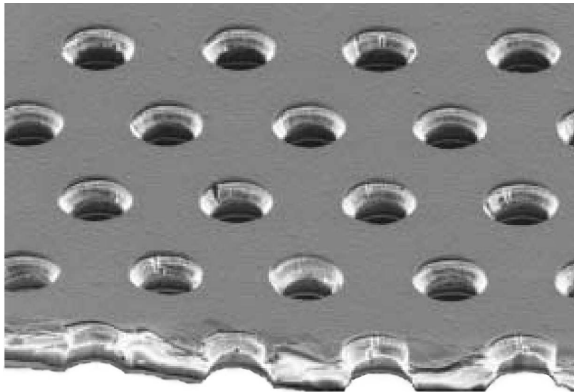
(a) Scanning electron microscope picture of a GEM foil [46].
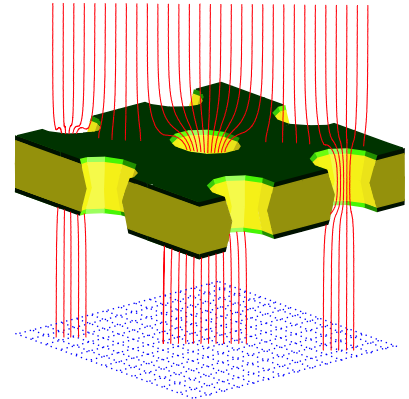
(b) The drift lines of a GEM foil, simulated with `Garfield` [47].

Figure 3.7: Detailed view of a GEM.

3.4 Ion Backdrift

3.4.1 Multi-Wire Proportional Readout and Active Gating

In a multi-wire proportional readout, many electron-ion pairs are produced near the sense wires by gas amplification. While the electrons end up on the wires, the ions drift in the opposite direction. Without any precautions, a large fraction of these slowly drifting charge carriers would end up in the sensitive volume of the TPC. On the one hand this deteriorates the electric field of the drift region, on the other hand the drifting primary electrons might combine with the ions, which would lead to a loss of primary statistics. To prevent the ions from drifting back, an additional layer of wires called *ion gate* is placed between drift volume and amplification structure. This gate has to be switched actively between its *open* and *closed* state.

In the *open* state (figure 3.8(a)) all wires are at the potential corresponding to their position so the homogeneous field is not affected. The gate is transparent for the electrons from the sensitive volume, but as well for the ions drifting back.

If the gate is *closed* (figure 3.8(b)), the wires are alternately switched to a higher and a lower potential, so that the field lines in the gating plane are perpendicular to the drift direction. All field lines end up on the wires. This prevents the ions from reaching the drift volume. On the other hand electrons cannot pass the gate either, which means the chamber is blind while the gate is closed.

In large experiments the gate usually is closed all the time, until a trigger signal from one of the other sub-detectors indicates an interesting event. There is enough time to open the gate until the primary electrons are drifted to the readout structure. After the recording of the signal the gate is closed again. This prevents for instance cosmic muons, which are not recorded, to produce backdrifting ions.

Cathode Plane

Gating Grid

Zero Grid

Sense and Field Wires

Pad Plane
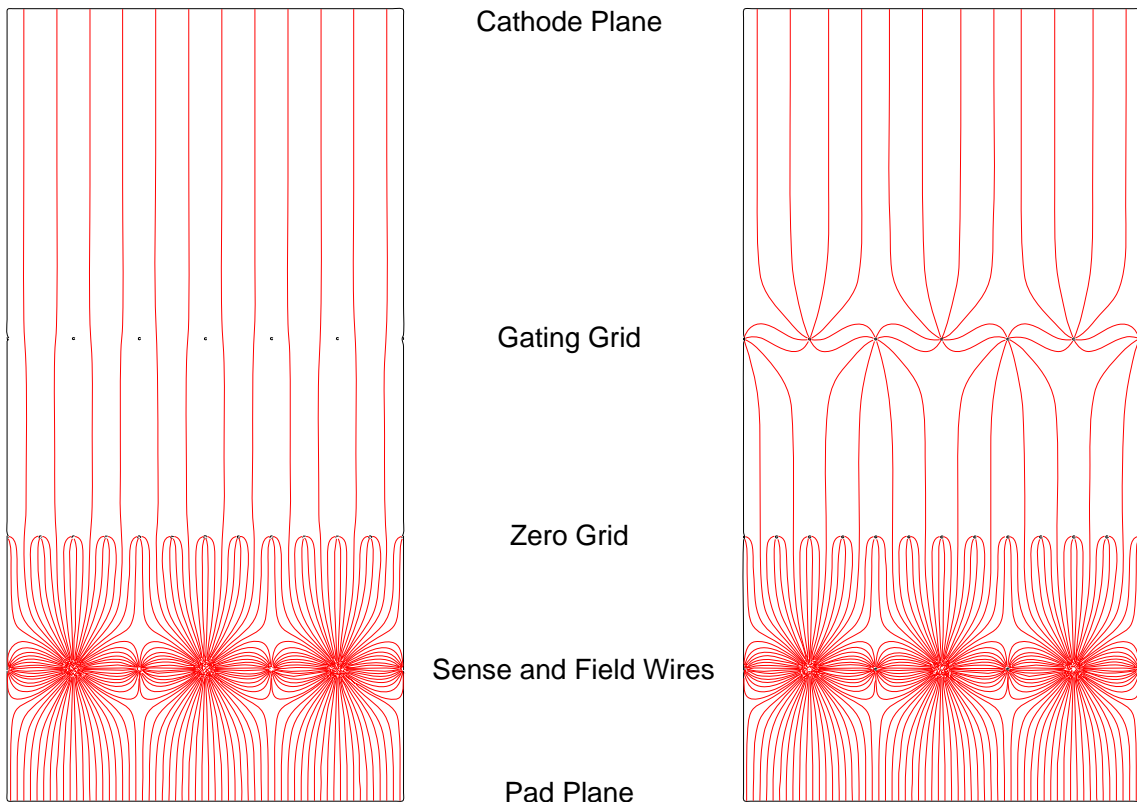
(a) Open gate: The gating plane is transparent for electrons and ions.

(b) Closed gate: Alternating potentials in the gating plane prevent ions from drifting back to the sensitive volume.

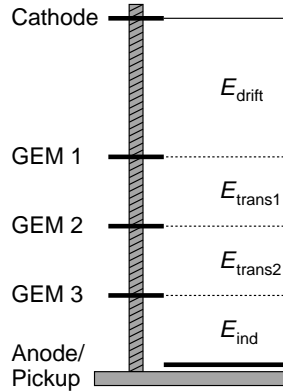Figure 3.8: Operation of a gating grid (simulation performed with `COMSOL Multiphysics` [45]).

Figure 3.9: Scheme and naming convention of a drift chamber with triple GEM readout (dimensions not to scale).

For the ILC with a bunch spacing of 308 ns there is data from about 150 bunch crossings simultaneously inside the TPC. Therefore the gate cannot be closed in between individual bunches. A different way to suppress the ion backdrift has to be found, and again the micro pattern gas detectors are a good candidate because they have an intrinsic suppression of ion backdrift.

3.4.2 Ion Backdrift Suppression in Micromegas

The Micromegas has a very high field below the mesh, causing most of the field lines in the amplification region to originate from the mesh. Most of the ions drifting back will follow these field lines and end up on the mesh. The ion backdrift suppression is determined by the field ratio between the drift field and amplification field. This means that the fraction of ions drifting back becomes smaller with higher gas amplification. For a Micromegas TPC, an ion backdrift of 2 to 3 per mill is expected [48].

3.4.3 Charge Transfer in a GEM Stack

The charge transfer in a multi-GEM structure is determined by the voltages across the GEM foils and the electric fields between the GEMs. Figure 3.9 shows the sketch of a triple GEM readout and the naming convention used below. GEM1 is the GEM facing the drift volume, the field between GEM1 and GEM2 is referred to as *first transfer field* (E_trans1). The field between GEM3 and the pad plane is called *induction field* E_ind.

For each GEM foil there are two important transfer parameters:

- Collection efficiency C: Fraction of charge carriers (electrons or ions) transferred into the GEM hole

$$C^\pm = \frac{N_{e^-,I^+} \text{ collected into GEM hole}}{N_{e^-,I^+} \text{ in front of GEM}}$$

- Extraction efficiency X: Fraction of charge carriers extracted from the GEM hole

$$X^{\pm} = \frac{N_{e^-, I^+} \text{ extracted from GEM}}{N_{e^-, I^+} \text{ in GEM hole}}$$

The index $^+$ refers to positive ions, the index $^-$ to electrons.

The gas amplification in the GEM is denoted by the gain factor G:

$$G = \frac{N_{e^-} \text{ in GEM hole}}{N_{e^-} \text{ collected into hole}}$$

The *effective gain* G_{eff} of a GEM foil is the number of electrons after passing the GEM divided by their original number in front of the GEM. It is described by the product of collection, gain and extraction:

$$G_{\text{eff}} = C^- G X^-$$

Ion backdrift ι is defined as the ratio of ions drifting back to the number of electrons recorded on the anode pads [49]:

$$\iota = \frac{N_{I^+} \text{ drifting back}}{N_{e^-} \text{ on anode}}$$

Collection and extraction of electrons and ions depend on the voltage across the GEM foil and the magnitude of the electric fields on both sides. A good understanding of these parameters can be found by studying the electrostatics of a GEM, as presented in reference [50]. Assuming the charge carriers follow the electric field lines, all transfer coefficients can be calculated from the electric flux in a GEM hole. From the results an electrostatic parametrisation has been developed. Figure 3.10 shows the results, which have also been published in [51]. Collection and extraction are plotted against the ratio of the external field to the field inside the GEM hole. For a constant GEM voltage, the field inside the hole is almost constant (neglecting the small penetration of the external field). Therefore the ratio is proportional to the external field.

The collection is 1 for small external fields and starts to drop for field ratios above 0.05. The extraction becomes better for increasing external field. A high transfer field for instance means good electron extraction from the GEM, but also good ion extraction from the next GEM and a low electron collection.

GEM Settings to Minimise Ion Backdrift

From the collection and extraction efficiencies it is not obvious at first sight which fields and voltages to chose. Reference [52] has studied the charge transfer in a GEM structure in detail and shows that ion backdrift in a triple GEM stack can be minimised following a simple set of rules:
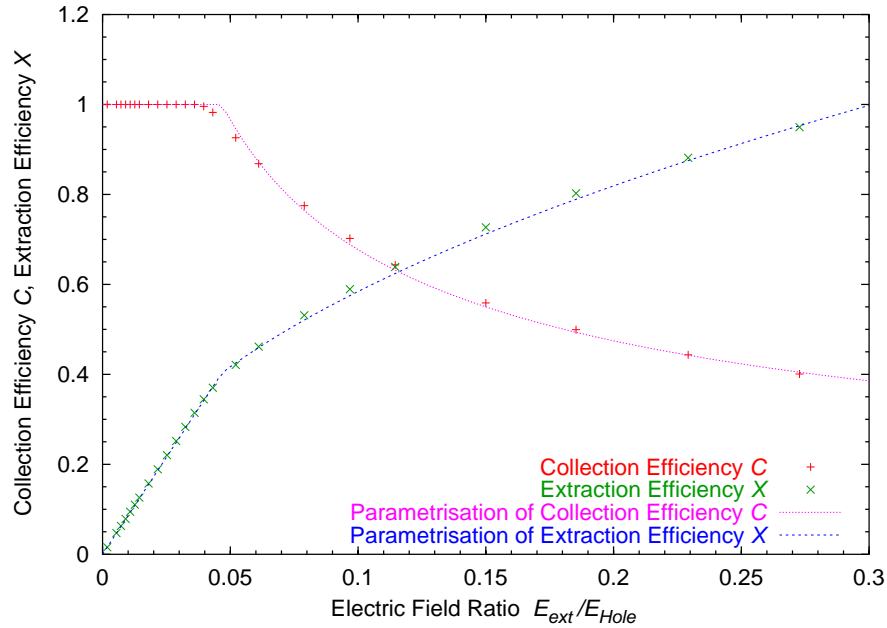
Figure 3.10: Electrostatic simulation and parametrisation of collection and extraction efficiency [50].

- The first transfer field and the induction field should be maximal.

- The second transfer field should be minimal (about 100 V/cm).

- The voltage across the third GEM should be maximal.

- The voltages across the first and second GEM have small influence on the ion backdrift and are used to set the required effective gain.

The drift field is determined by the gas mixture, as described in section 3.2.1.

The maximum values for the voltages and electric fields are dependent on the discharge probability. They should be as high as possible, which allows a better ion backdrift suppression, but the setting still has to operate reliably. An ion backdrift of 2.4 per mill has been achieved for a triple GEM structure in 4 T magnetic field [52].

In contrary to the Micromegas, the fraction of ions drifting back does not depend on the gain, but only on the applicable voltages and fields. This means the absolute number of ions drifting back is lower for lower effective gain.

The small second transfer field is crucial for the ion backdrift suppression, but also reduces the electron extraction from the second GEM. The issue that this could lead to a degradation of the signal quality is examined in chapter 8.

4 The TPC Prototype

The ILC TPC group of the III. Physics Institute at RWTH Aachen has constructed a field cage prototype which is designed to provide a field homogeneity of better than 10^{-4} [53]. This chapter introduces the field cage and the readout system of the TPC prototype.

4.1 Field Cage

One of the main tasks of the new TPC is performing measurements in high magnetic fields. To fit into the 5 T superconducting magnet at DESY (see section 4.7), the outer diameter has been set to 260 mm. An inner diameter of 231 mm leaves enough space to house the standard GEM foils and to place all cables for the high voltage supply. A drift distance of 263 mm allows fields up to 1000 V/cm using a 30 kV power supply for the cathode voltage.

The field cage itself consists of two layers of copper strips. The strip pitch is 2.8 mm and the inner layer is shifted against the outer layer by half a pitch, so that the copper of the strips overlap. This prevents the electrical field between the strips and the grounded outermost layer from penetrating into the drift volume.

Figure 4.1 shows a sketch of the field cage. Four layers of insulating Kapton® are glued onto the inner Kapton® layer holding the copper strips. The mechanical support structure is made up of aramid honeycomb and a layer of glass fibre reinforced plastics (GRP). The outermost layer is a grounded aluminium foil.

To prevent the gas from being heated by the resistors of the voltage divider, the resistor chain is placed outside the gas volume. A high voltage insulating ceramics plate provides thermal contact to the environment and dissipates the heat. A photograph of the TPC prototype is shown in figure 4.2.

4.2 Readout Plane

The readout plane consists of 1120 pads with a size of 1.27×7 mm^2 (figure 4.3). The plane is composed of five blocks with 14 rows of 16 pads each. From one block to the next the structure is shifted by one row. This is necessary due to the mechanical layout of the connectors to the preamplifiers. These connectors are directly placed on the back of the board (see figure 4.4).

With the current electronics 448 channels can be read out, which means that two of the five blocks can be equipped. For the measurements presented in this thesis,
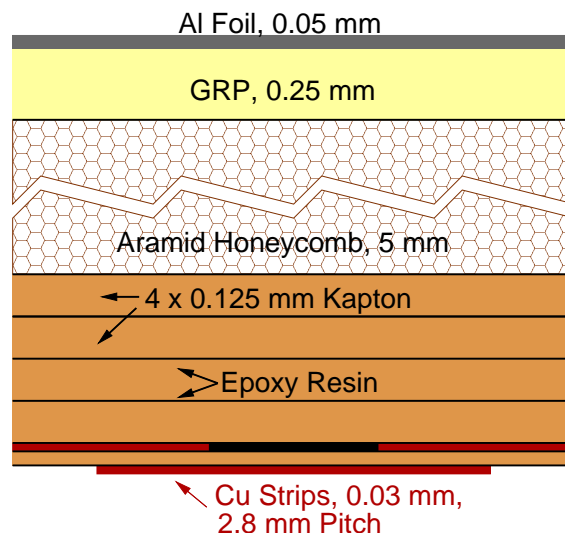
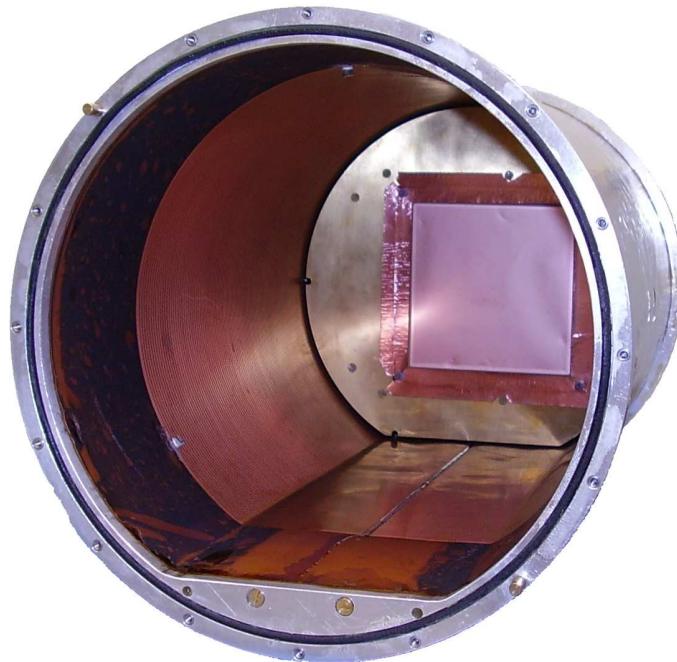Figure 4.1: The sandwich structure of the field cage [53].

Figure 4.2: The prototype TPC: Inside the chamber the inner field strips are visible. In the back part of the chamber the electrical shield surrounding the first GEM can be seen. The mounting frame of the GEM is covered with an adhesive copper foil. The resistor chain for voltage division is located outside the gas volume, in the flat part at the bottom of the chamber.
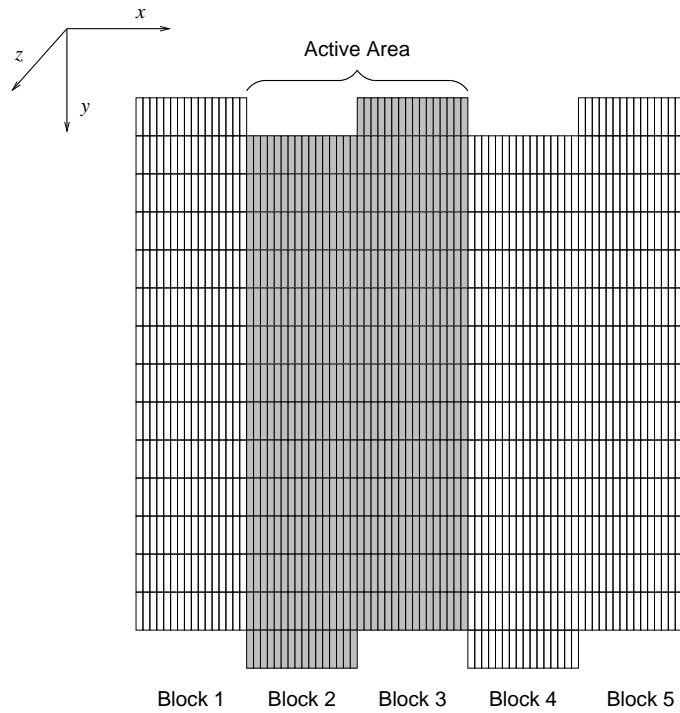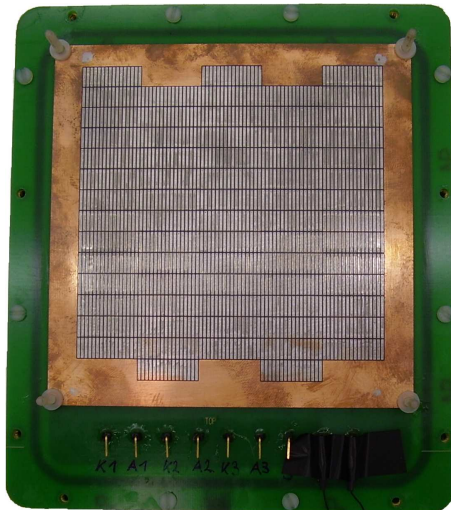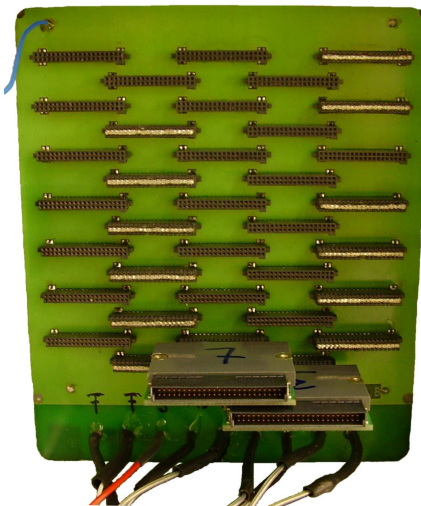
Figure 4.3: Layout of the pad plane and orientation of the coordinate system as seen from inside the chamber. The active area is shaded.

(a) The pad plane of the TPC prototype. In the corners of the copper-plated area the mounting rods of the GEM stack are visible. The connectors in the lower part provide the high voltage for the GEMs.

(b) The connectors for the preamplifiers at the back of the readout plane. Two of the Preshape32 preamplifiers are plugged in. Unused readout pads are grounded using short circuit connectors.

Figure 4.4: The readout plane and the preamplifier connectors on its back.
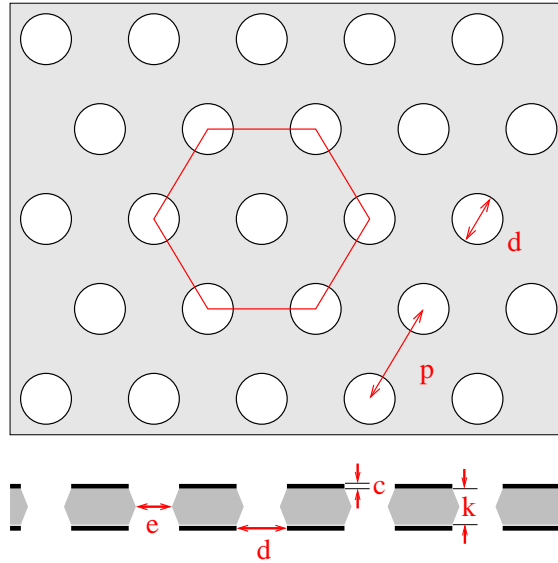
Figure 4.5: Geometry of the GEMs used for the measurements: The pitch of the hexagonal pattern is $p = 140$ µm, the inner hole radius is $e = 50$ µm, the outer radius in the copper coating is $d = 70$ µm, the Kapton® foil has a thickness of $k = 50$ µm, the copper coating of $c = 5$ µm [52].

block 2 and 3 were used. This corresponds to an active area of 40.6×104.8 mm² (with the first and the last half row being inactive). Note that the active area of a GEM foil is 100×100 mm², which means that the first and the last row are only partially covered. Therefore, a lower signal level is expected.

A stack of three GEMs is mounted onto the readout plane. The GEMs were produced by the Gas Detector Development Group at CERN [46]. They have an active area of 100×100 mm². The Kapton® foil is 50 µm thick, coated with 5 µm of copper on each side. The holes are arranged in a hexagonal pattern with 140 µm pitch. Due to the etching process used in the production, the inner diameter off 50 µm is smaller than the diameter in the copper coating, which is 70 µm. Figure 4.5 shows a sketch of the GEMs' geometric parameters.

The GEMs are glued in between two frames to stretch them. These 0.5 mm thick frames have outer dimensions of 124×124 mm². They are placed on threaded rods with spacers between them, so the transfer gaps between the GEMs and from the last GEM to the pad plane are 2 mm each. To provide a homogeneous field, the uppermost GEM is surrounded by an electrical shield made of brass. This shield is mounted on the readout board using spacers to assure the correct positioning with respect to the GEMs (figure 4.6). The GEM frame is made up of insulating glass fibre resin compound and would introduce a non conducting surface into the anode plane of the drift region. This would result in a penetration of the extremely inhomogeneous fields at the edge of the GEM stack into the drift space. To avoid this, the frame has been coated with a self adhesive copper foil. The foil is pasted onto the frame and across the small gap onto the shield. Due to its conducting
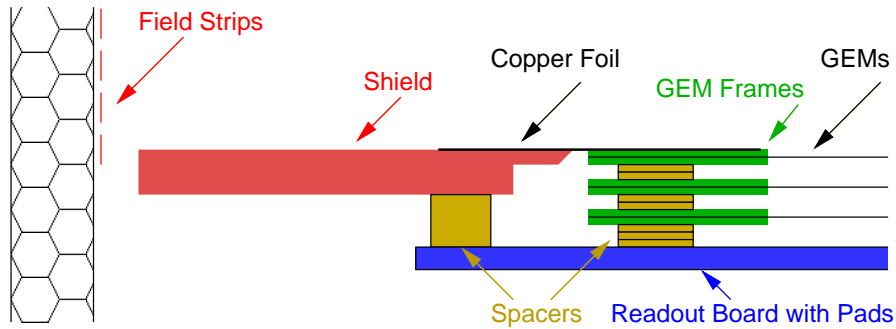
Figure 4.6: Positioning of the readout structure in the field cage: The nominal position of the shield's upper edge corresponds to centre of the field cage's first strip and the frame of the first GEM.

glue, it is at the same electric potential as the shield. Every GEM electrode as well as the shield and the first strip of the field cage are connected to a separate high voltage source. Each high voltage cable is connected to a gas tight lead-through in the readout board.

The readout board with the GEM stack and the shield is directly mounted onto the end plate of the chamber. The nominal z position of the shield corresponds to the centre of the first field strip. The shield has a mechanical offset of 0.5 mm to the cathode of GEM 1 (the uppermost GEM electrode facing the drift volume). This is because the GEM frame is 0.5 mm thick and the shield has to be in-plane with it. Due to mechanical inaccuracies the shield and GEM 1 are not precisely at their nominal position. The individual high voltage channels for the GEMs, the shield and the first strip of the field cage allow to compensate for these inaccuracies and the 0.5 mm between GEM 1 and the shield (see section 7.1.1).

4.3 Readout Electronics

The signal of each pad is electronically amplified using the Preshape32 chip [54], a 32 channel preamplifier and shaper with 45 ns rise time. Therefore, it can take advantage of the fast electron signals from a GEM amplification structure.

Cable drivers allow to transfer the signals over a distance of 8 m to the ADCs[1]. The signals are recorded using the Fastbus-based Time Projection Digitisers (TPDs), which were developed for the ALEPH experiment. They have a sampling frequency of 12.5 MHz and a resolution of 8 bits. A memory of 512 bytes per channel allows to record 40 μs per event. One TPD board contains 64 ADC channels, the Fastbus crate can house up to seven TPDs, which results in a total of 448 channels for this setup.

The clock is generated by a module called SMTPD, which was not part of the original ALEPH readout chain. It generates test pulses for debugging the TPDs.

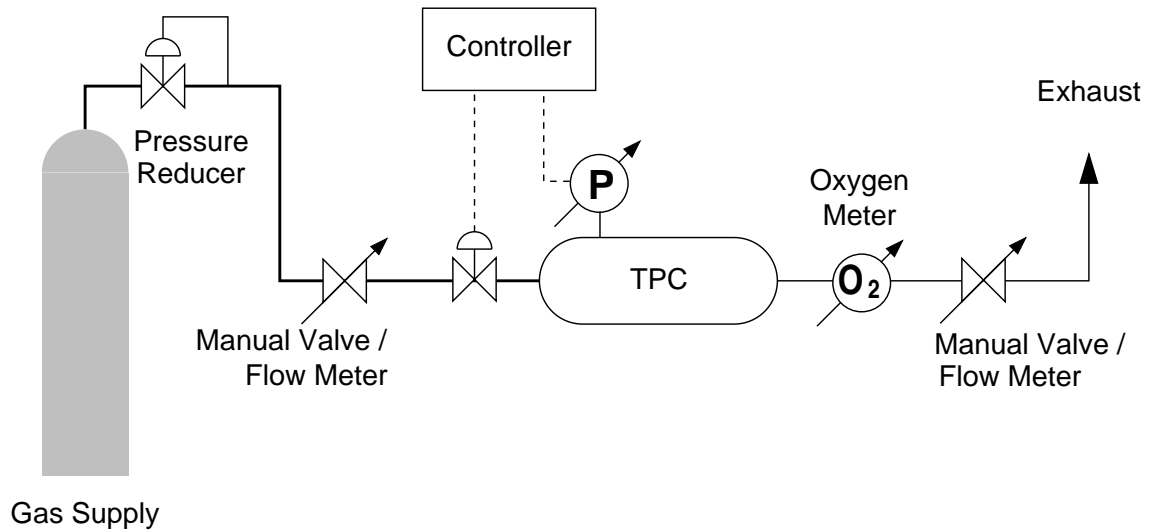[1]ADC: Analogue-Digital Converter

Figure 4.7: The gas system.

A FVSBI controller card, produced by CES, is working as bus master. It is connected to a Macintosh IIfx personal computer using the CES FVI 9214 VICbus to FASTBUS Interface [55]. The Macintosh is connected to a Linux PC via a 10 MBit-Ethernet link. This Linux PC works as a Macintosh file server, which on the one hand circumvents the problem of very limited disk space on the old Macintosh system, on the other hand provides the possibility to write steering files to the shared directories to control the data acquisition software running on the Macintosh from the Linux machine (see section 6.1.3). An overview of the readout, including the hodoscope, can be found in chapter 6.1.

All 512 samples per channel can be read out using the program `rawread`. This method produces rather large data files and is very slow. As the system is not the original ALEPH readout chain, but was used for debugging defective TPDs, it is not optimised for speed. It needs 2.5 seconds to read out all seven TPDs. Therefore `rawread` is only used for debugging and to record pedestal levels of the signal.

To reduce the data size and improve the readout speed, peak finding and zero suppression can be performed on the TPD. To do so, a threshold is set for each channel individually. All samples above this threshold are written to a "hit list", so only relevant information is saved to disk. The readout software `fastDaq` uses this method and enhances the readout rate to 20 Hz, 50 times faster than without zero suppression. This is enough to enable reasonable operation at a test beam facility.

4.4 Gas System

The TPC has a gas volume of approximately 16 l. This allows an open gas circuit with a still moderate gas consumption. Figure 4.7 shows the scheme of the gas system. First the high pressure from the gas bottle is reduced to approximately

1000 hPa above atmospheric pressure. A manual valve limits the gas flow into the TPC. To protect the chamber, it has been adjusted to allow a maximal overpressure of 25 hPa.

The gas system's main component is the Bronkhorst EL-PRESS/E-7000 controller. It measures the pressure in the TPC and keeps its absolute value constant within ± 1 hPa by controlling the gas flow into the TPC. Obviously this only works for pressures above environmental pressure.

If the atmospheric pressure changes too much, the absolute pressure in the chamber cannot be maintained. The minimal overpressure in the TPC should be approximately 8 hPa to have enough flow to ensure good gas quality. The maximal overpressure is adjusted to 25 hPa. This gives a variation range of 17 hPa for the environmental pressure without having to adapt the pressure in the TPC. Taking into account the trend of the atmospheric pressure, one can keep the same absolute pressure from minimum several hours up to some days. So a complete series of measurements can be performed under the same conditions.

To measure the oxygen content of the gas, an oxygen monitor model EC90M produced by Systech Instruments was connected to the TPC's gas outlet. The system has been operated with a gas flow of about 10 l/h, which is sufficient to keep the oxygen content in the exhaust gas below 100 ppm.

Finally another manual valve again limits the gas flow, so the dynamic pressure creates the overpressure in the TPC.

4.5 High Voltage Supply

The high voltage (HV) for the GEM stack, the shield and the first strip of the field cage is provided by a CAEN SY127 power supply (figure 4.8). It is a modular high voltage crate which can house up to ten modules with four HV channels each. Each channel monitors the current and switches off the voltage if a certain value is exceeded. To protect the GEMs in case of a discharge, a threshold of 1 µA was used. A single channel, which has been switched off, introduces a grounded electrode in the GEM stack. If all other electrodes are still on high voltage, this would trigger additional discharges. To avoid this, all channels are switched off in case one channel is tripped. This is implemented connecting the status ports of the individual channels via a daisy chain. If one of the channels is tripped, it switches the status port to ground, which switches off the other channels in turn.

The trigger system is made up of two scintillation counters (see section 6.1.1). The photomultipliers of the scintillation counters are also powered by the SY127, but they are not included in the trip chain.

The cathode plane is connected to a Wallis V.C.S 303/1 power supply, which can deliver voltages up to -30 kV. Unfortunately this device cannot be controlled remotely. The voltage is set using a multi-turn potentiometer with turn-counting dial and monitored on an analogue voltmeter. Therefore, any changes in the drift field or the total GEM stack voltage require manual adjustment of the cathode
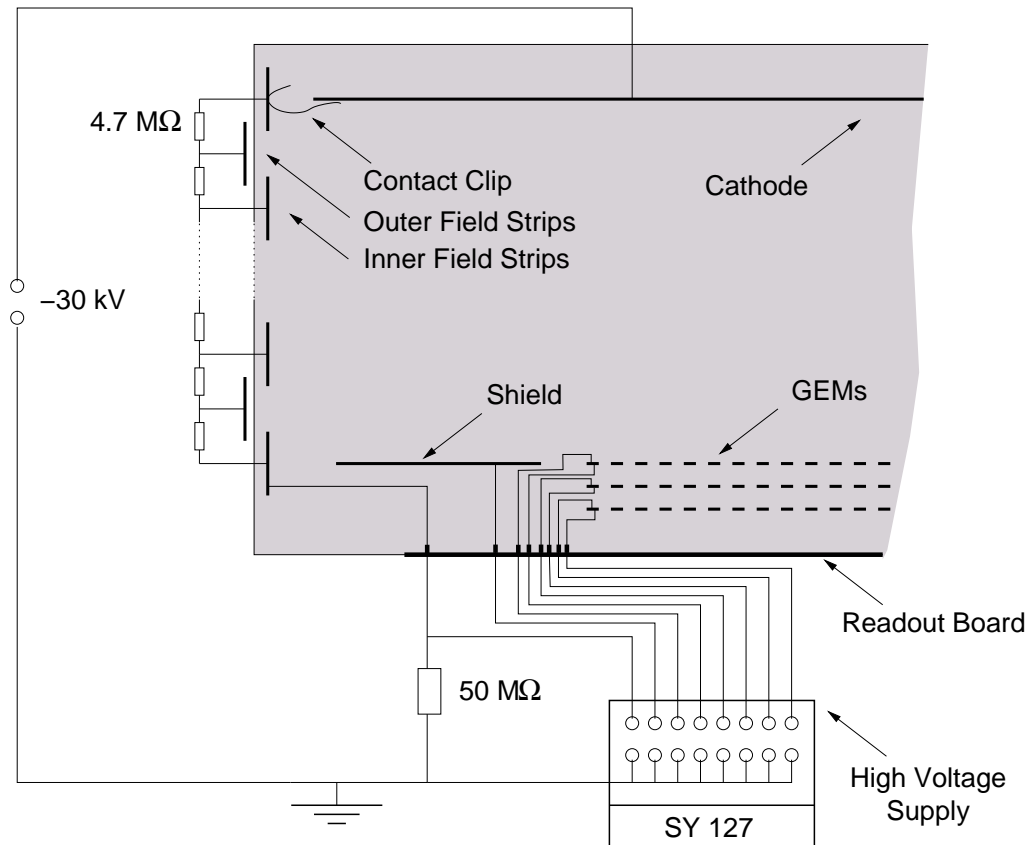
Figure 4.8: The high voltage connections of the TPC prototype. The gray shaded area represents the gas volume of the chamber. To allow a precise adjustment of the first field strip's potential, it is connected to a channel of the SY127 unit (in addition to being part of the voltage divider).
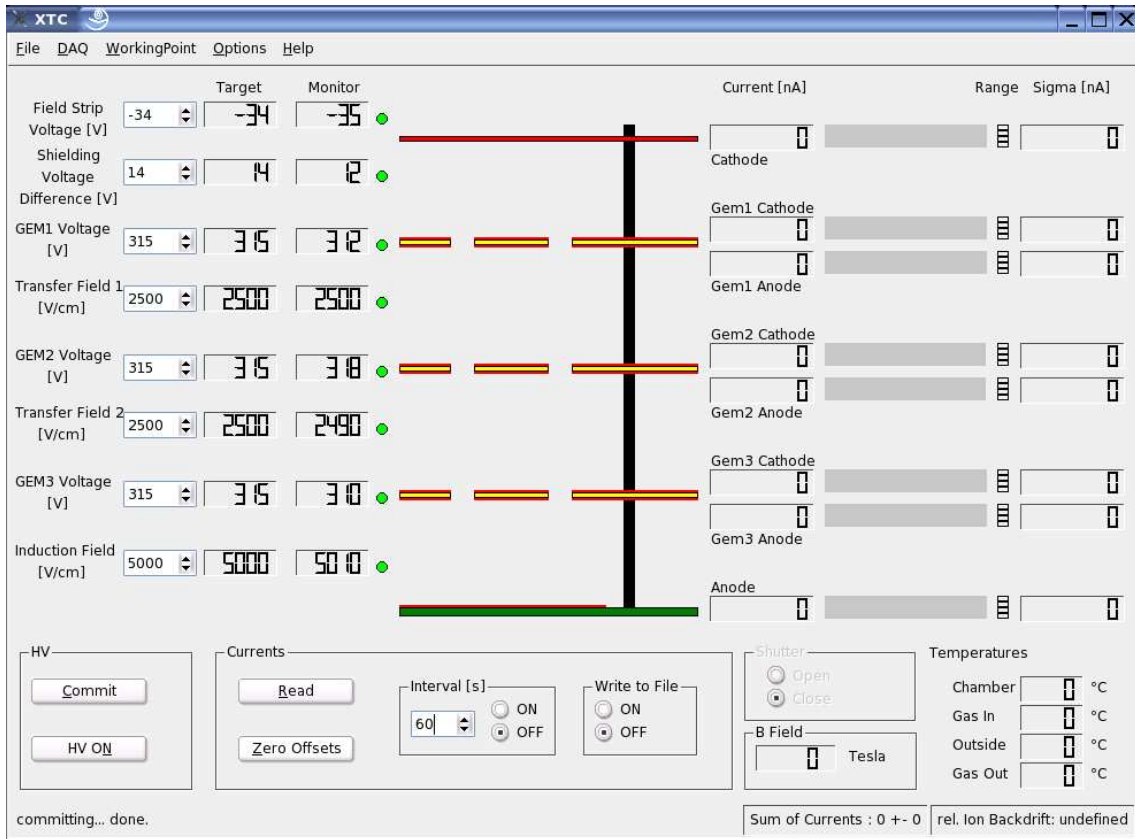
Figure 4.9: The user interface of the slow control software `xtc`. The left part of the window shows the high voltage controls. On the right side, the currents of each GEM electrode can be displayed.

potential.

The SY127 is controlled manually using a keypad on the front side of the housing. In addition, the crate can be remote-controlled via the proprietary CAENET interface or using a serial RS232 connector for a VT52 compatible terminal. The `HV_Channel` class [56] provides a convenient C++ interface to the SY127 by emulating a VT52 terminal. It is used by the **X** Window System **T**est **C**hamber software `xtc` to interface with the high voltage crate.

`xtc` was developed as slow control and data acquisition software for charge transfer measurements in GEM structures. Figure 4.9 shows the graphical user interface of the application. The section for the GEM stack settings is displayed on the left side. The `xtc` allows to enter the voltages to be applied across the GEMs and the value of the electric fields between them. The absolute voltage for each electrode is calculated internally and transferred to the SY127 unit. The target voltage and field as well as the monitored values read from the HV system are displayed next to the input box. A simulated LED shows the status of each HV channel (green = o.k., red = failure, yellow = ramping).

An *Interval* mode allows to read the status and the monitor values periodically.

In case a trip occurred, the HV channels are reset and switched on again. This allows automated long term measurements. Complete sets of selected voltages and fields can be bookmarked as "working points". Besides setting the values manually, a script can be executed. In the *Interval* mode the working directory is scanned for a default script. This script is executed once and then the file is deleted. This enables programs like the main measuring software `ligros` to easily control the high voltage settings (see section 6.1.3).

The right part of the `xtc` window can display the measured currents on each electrode, the monitored temperatures and the magnetic field at the DESY 5 T facility. The particle rate at the test beam does not suffice to produce measurable currents and the temperature is recorded by an environment monitor system. So this part of the software has been disabled during the measurements presented here. Only the HV control section was used.

4.6 Environment Monitor System

The environmental temperature and pressure as well as the air humidity are monitored throughout the measurements.

Air temperature and humidity are recorded with a Sensirion SHT71 sensor [57]. The precision of the temperature measurement is ±0.5 °C at 25 °C with a reproducibility of 0.1 °C. The humidity is measured to ±3.5 % between 20 % and 80 % relative humidity, the reproducibility is 0.1 %.

A XFAM-115KPASR sensor produced by Fujikura [58] determines the absolute atmospheric pressure with a precision of ±2.5 % of the measured value. The ADC limits the resolution to ±1.1 hPa, the reproducibility of the measurement is of the same order. Both sensors are read out using the *Cold Box Control Serial Interface "Cooli"* [59]. The *Temperature Humidity Pressure Control Daemon* `thpcd` reads all values in intervals of 15 minutes and writes them to a data base.

Details on the environment monitor system can be found in [60].

4.7 Experimental Setup for Measurements in a Magnetic Field

The TPC at the ILC detector will be operated in a 4 T magnetic field. A superconducting solenoid available for test measurements at DESY Hamburg provides a magnetic field up to 5 T. The magnet has a total length of 187 cm. Its bore has a diameter of 27.8 cm. The magnitude of the magnetic field along the solenoid's axis is depicted in figure 4.10. The active volume of the TPC has been centred in the magnet; it reaches from −13 cm to +13 cm. The magnetic field is homogeneous to a level of $5 \cdot 10^{-3}$ within this region. This is less than the inhomogeneities in the electrical field near the readout plane (see section 7.1.2) and will not be corrected for in the analyses. Figure 4.11 shows the TPC in the bore of the magnet, before
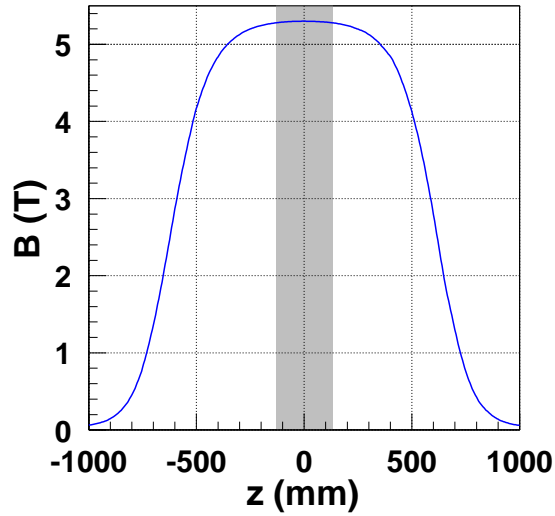
Figure 4.10: The magnetic field along the central axis of the superconducting magnet at a current of 1000 A [61]. The drift volume of the TPC reaching from -130 mm to $+130$ mm (shaded area) is in the homogeneous part of the field.

connecting the high voltage and readout cables and placing the field cage at the correct position.

Scintillator panels are mounted above and below the cryogenic vessel. They make up a trigger system for muons produced by cosmic radiation (figure 4.12). A recorded muon first passes the upper scintillator. Its trajectory is bent in the magnetic field outside the coil. When it passes the coil, the curvature changes sign. The particle track is recorded in the TPC and the particle leaves the magnet, its trajectory again being bent in the other direction before it reaches the second scintillator. An estimation shows that the minimal radius of a trajectory traversing both scintillators and the active area of the TPC is 900 mm [62]. This corresponds to a muon energy of approximately 1 GeV in a 4 T magnetic field. The sagitta of such a track within the 100 mm large active area is 1.4 mm.

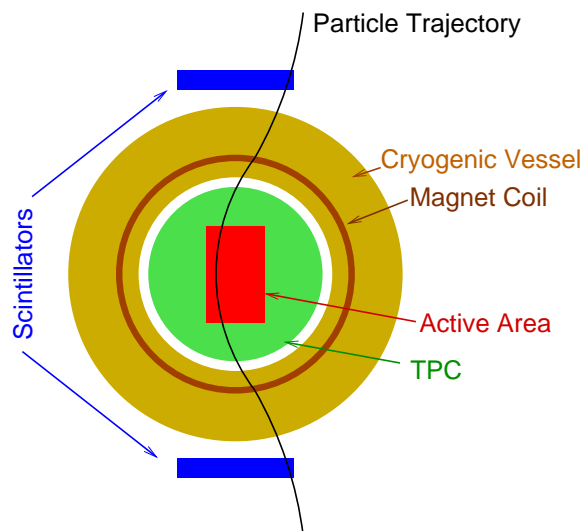Figure 4.11: The TPC in the bore of the 5 T superconducting magnet at DESY Hamburg.

Figure 4.12: Sketch of the TPC in the magnet (dimensions not to scale). A particle recorded has to pass both scintillators and the active area.

5 Data Classes and Reconstruction Software

To reconstruct the particle tracks, the modular software package `acdaq` has been developed. It is based on the ROOT data analysis framework [63]. Starting from the data provided by the TPDs, the particle track is reconstructed in three steps:

1. Reconstruct peaks in the signal of the individual channels.

2. Cluster the peaks to 3D points.

3. Find tracks and fit them.

Figure 5.1 gives an overview of the reconstruction workflow. The peak finding is either done via software or directly in the TPD. If the complete raw data has been recorded, software peak finding is executed and then the pedestal is subtracted. In case peak finding is performed in the TPD, a so called "hit list" is generated and only the relevant samples are read out. Subsequently the pedestal subtraction is run on the **z**ero **s**uppressed **r**aw data (ZSR). The resulting peaks contain charge and time information on a per-channel basis. At this stage, the time jitter between trigger and readout clock can optionally be corrected (see section 5.2). This requires an additional time marker pulse, which is generated at a fixed time after the trigger and recorded together with the signal.

In the next step, the channel information is grouped to clusters of neighbouring channels having a hit at the same time coordinate. From this information 3D space points are calculated. The points are corrected for systematic distortions if a distortion map is available.

In the last step the track finder assembles tracks from the points. For straight tracks, the track parameters are calculated by linear regression. For a helix, the parameters are fitted using a χ^2 minimisation.

A list of the data classes and their properties is shown in table 5.1, a detailed description can be found in appendix B.

5.1 Peak Finder

For every channel the pedestal p_i and its variance σ_{p_i} are determined. For this purpose special pedestal raw data files are recorded. The voltage in the GEMs is turned off and the trigger signal is generated by a pulse generator.
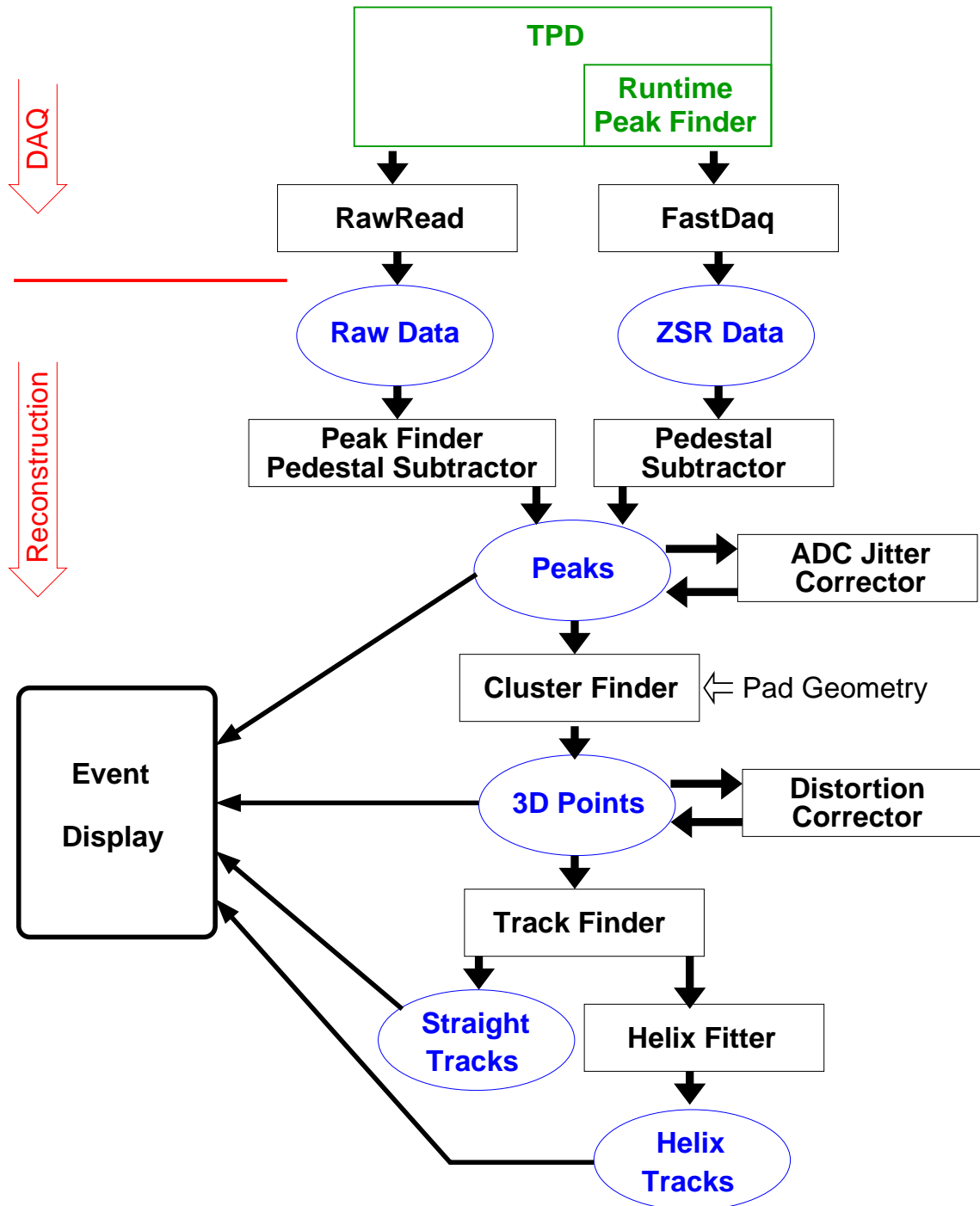
Figure 5.1: Data flow of the reconstruction software.

TPCPEAK	Pulse with charge and time information on one channel
TPCPOINT	3D point with x, y, z coordinates and charge
TPCTRACK	Straight track with parameters a, b, c, d (slope and axis intercept in xy and zy plane)
TPCHELIXTRACK	Helix with reference point, curvature, dip angle and angle in xy plane

Table 5.1: List of the data classes and their properties. A complete description can be found in appendix B.

A peak is identified if the measured ADC value is above the threshold t, which is the pedestal plus five times its variance, rounded up to the next integer:

$$t_i = \lceil p_i + 5\sigma_{p_i} \rceil$$

The peak ends when the signal falls back below the threshold.

5 σ is a rather high threshold. It has been chosen because the signals are short and many pulses consist of only one time sample. This is due to the short shaping time of the preamplifier in combination with the relatively slow ADC. Therefore all signals with only one time sample above the threshold are counted as a valid hit. A lower threshold of 4 σ for instance would produce around 14 noise hits per event in the $448 \cdot 512$ time samples. This is too much compared to a maximum of 14 measured points on the track.

After the peak finding the pedestal is subtracted, the centre of gravity in time is calculated and the charge (ADC counts) in the pulse is summed up. This information is stored in the TPCPEAK.

5.2 ADC Jitter Corrector

Clock and trigger are not synchronised in this setup. This causes a jitter of the measured time. Figure 5.2 gives a schematic illustration of the origin of the jitter and its correction. The clock runs continuously. At some point within a clock cycle a trigger signal arrives. The measurement starts at the first clock tick following the trigger. The jitter J is the time difference between the actual trigger and the start of the measurement. The recorded time is the time t' between the first clock tick after the trigger and the arrival of the signal. By recording a time marker, which is generated at an exactly known time M after the trigger, J can be determined. The time M' at which the marker signal is recorded is short by J, too. So J can be calculated as the difference between M and M', and the real time t between trigger and signal can be determined.

Figure 5.2 is simplified for illustration. Of course the signal as well as the time marker are several clock cycles long, so their time position has a resolution better than one cycle. Otherwise these signals would also have a jitter. The time marker
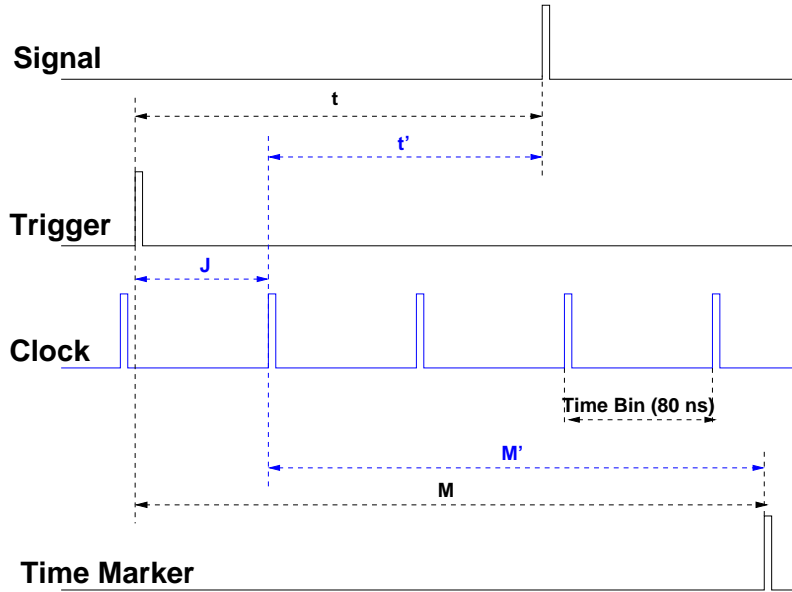
Figure 5.2: Illustration of the jitter between clock and trigger.

has been chosen to be about nine clock cycles long, so there is no bias from the phase of the clock, even with the simple centre of gravity method used for reconstruction (see appendix D for details). For the TPC signals there is some dependence on the clock phase, as shown in section 8.2.2.

The ADC jitter corrector processes the reconstructed peaks. The time marker signal is recorded in in the last 64 of the 512 time samples, so it does not interfere with the actual TPC signal. The time marker position for each event is calculated from all pulses in this time window. After the correction, the time marker information is removed from the data. This module is optional. Having the same input and output format makes its use transparent for the next reconstruction step.

5.3 Point Finder

The point finder is a row-based clustering algorithm. All peaks on neighbouring pads are grouped together, if they are in a certain time window. The width of this window is usually two times the mean length of a pulse, which means the pulses have to overlap. One empty pad within a cluster is allowed if there is a signal on the pad above or below the empty one. This might be the case if there are dead channels, for instance. Again, from the charge of all peaks in the cluster the centre of gravity in x and z direction is calculated. In the y direction, the point is placed in the middle of the pad row.

At this point the pad geometry is used to calculate the x and y coordinates in units of mm. The time coordinate z is calculated in µs, using the sampling frequency of the ADC. The z coordinate is intentionally left in time units and not converted to mm, because the drift velocity is not known at this stage. For
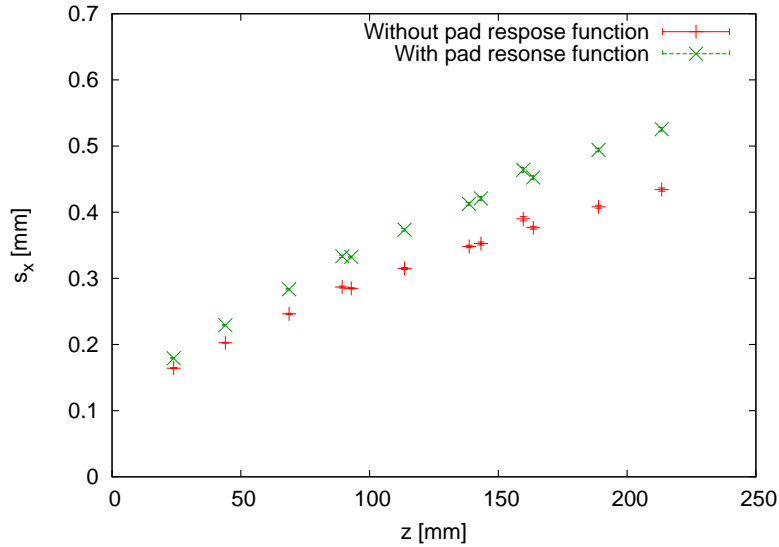
Figure 5.3: Single point resolution determined with and without pad response function. A Gaussian distribution does not describe the pad response properly. Correcting with this function even degrades the resolution. The width of the Gaussian has been calculated from the drift distance and the transverse diffusion coefficients simulated by `Magboltz` [44].

the measurements performed with the hodoscope described in chapter 6, the drift velocity is determined together with the exact position of the TPC in the hodoscope. But this requires completely reconstructed TPC tracks. For measurements without hodoscope a theoretical value has to be taken. The calculated information is saved as TPCPOINTS.

Each point has a quality word which allows to flag the point as "bad point". This is important for those points where the charge information might be incomplete. This is the case when the cluster either contains a dead channel, is next to one, or is at the edge of the readout, where only part of the signal is collected. For the calculation of the track parameters only the valid points are used, as well as for the calibration and the resolution studies.

The centre of gravity method is known to bias the position of the point towards the centre of the pad with the maximal charge deposition, especially for clusters with only two or three pads. A better estimate should be possible using a pad response function. However, a simple approach assuming a Gaussian distribution was not able to improve the results (figure 5.3). There are two factors making the charge deposition on the pads not follow a Gaussian distribution. The first is the statistical fluctuation in the GEMs' gas amplification process, which causes a non-uniform mapping of the charge distribution. The second is the threshold of the electronics, which cuts away the smaller parts of the signal. Correcting with the wrong pad response function appears to give a larger displacement than caused by the bias from the centre of gravity method.

5.4 Distortion Corrector

With the help of the hodoscope (see chapter 6) a 3D map of the systematic distortions can be generated (see section 7.2.1). For every 3D point a correction is calculated and applied. If there are too many gaps in the distortion map, this correction cannot be computed. In this case the uncorrected point is flagged as invalid. The details of the correction algorithm are described in section 7.2.2. As this is an optional module, the output format is identical to the input.

5.5 Track Finder

The track finder is a modified version of the *track following* algorithm.[1] It starts with the first and the last point of the sample and extrapolates a point in the next row, counting from the first one. If a point matching the extrapolated point is found (within a search window), it is added to the track and the track parameters are recalculated.

The track is determined by the slope and the axis intercept in two projections:

$$x = a \cdot y + b$$

$$z = c \cdot y + d$$

The track parameters are calculated by linear regression [64], for instance in the xy plane:

$$a = \frac{\sum y_i \sum x_i - n \sum y_i x_i}{\left(\sum y_i\right)^2 - n \sum y_i{}^2}$$

$$b = \frac{\sum y_i \sum y_i x_i - \sum y_i{}^2 x_i}{\left(\sum y_i\right)^2 - n \sum y_i{}^2}$$

The same calculation is done for c and d in the zy projection.

If no point is found in the next row, the algorithm tries to find a point in the next to next row. This allows single points missing within a track. If there is more than one point missing, the track is rejected. A track is valid if there are at least five points on it.

All points found to be on a valid track are flagged and the algorithm is repeated for the remaining points. This allows multiple tracks in one event.

The helixes in the measurements have a small curvature and can be approximated by a straight line. To find the points belonging to a helix, the linear track finder with wider acceptance cuts is used. Track parameters taken from the straight track are used as starting values for the helix fit.

---

[1]Usually the track following method starts with two points at the *beginning* of the track, and then extrapolates the next one. This version uses the first and the last point of the track as seed.

5.6 Helix Fitter

The helix fitter minimises the mean distance of the measured TPC points to the helix by minimising the function

$$F = \sum_i \left(x_i - x(s'_i)\right)^2 + \left(y_i - y(s'_i)\right)^2 + \left(z_i - z(s'_i)\right)^2$$

x_i, y_i and z_i are the coordinates of the point measured in the TPC. The helix is parameterised along the track length s (see description of helix in appendix B.6). s'_i is the track length of that point on the helix which has smallest distance to the TPC point p_i.

The point of closest approach on the helix cannot be calculated analytically. The point with the closest distance in the xy projection is used as approximation in this algorithm. No points are expected to fit well in the xy plane while being far off in z, as they were selected by the track finder.

5.7 Event Display

To visualise the results, an OpenGL based event display has been developed. It provides a freely rotatable 3D view and the three projections into the xy, the zy and the xz plane (figure 5.4). In all views the reconstructed points and the fitted tracks are shown. Those points belonging to a track are highlighted by using a different colour and larger point size. In the 3D view the active area of the chamber is indicated by a three-coloured box. The readout plane corresponds to the blue face in the front. The projection into the xy plane, which corresponds to the readout plane, shows the pads in addition. The maximum charge on the specific channel is shown as colour code (from blue to yellow, cyan marks "out of range"). In the top view (xz projection) and the side view (zy projection) the readout plane is located on the left side. The drift direction is along the horizontal axis, from right to left.
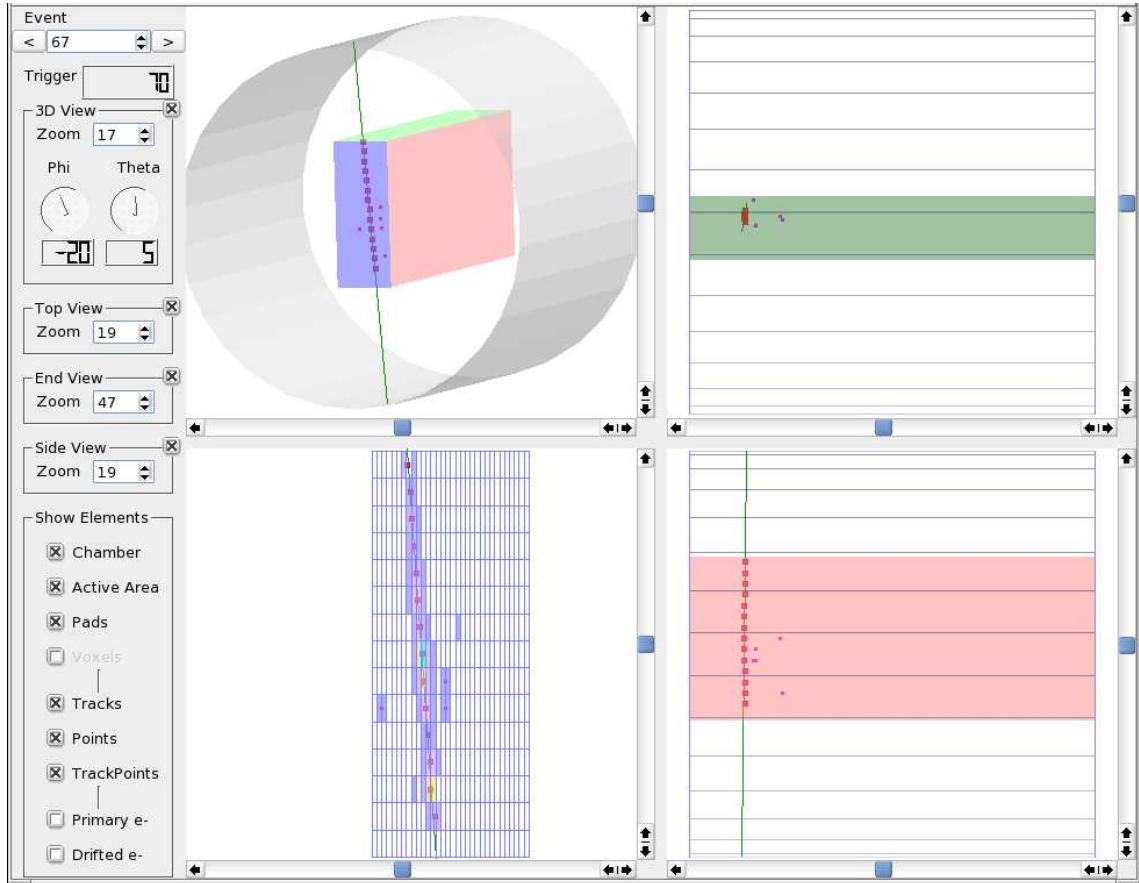
Figure 5.4: The OpenGL based event display showing the track of a positron from the test beam measurements. It provides four different views: A 3D view (top left) and the projections into the xy plane (bottom left), the zy plane (top right) and the xz plane (bottom right). The xy projection additionally shows the charge deposition on the pads.

6 The Hodoscope Test Stand

To determine the real, unbiased spatial resolution of the TPC, a second, independent measurement of the particle track is needed. This also allows studying systematic deviations in the TPC and thus a check of the drift field's homogeneity. A hodoscope measuring the particle position before entering and after leaving the field cage provides this independent track measurement. This chapter will introduce the test stand and describe the alignment of the TPC in the hodoscope.

6.1 The Hodoscope

The hodoscope is made up of silicon strip sensors with 768 parallel strips at a pitch of 122 µm. These sensors are mounted onto an aluminium precision plate (figure 6.1). As a single strip sensor is only able to do a one-dimensional measurement in one plane, two sensors are mounted on top of each other with the strips along perpendicular directions. This provides an active area of 80×93 mm^2. The measured coordinate is always perpendicular to the strips of the module. One of the sensors has the strips oriented along the drift direction of the TPC. It measures the x coordinate and is referred to as "x module" below. The other module with the strips along the x axis measures the z coordinate and thus is called "z module" (see section 6.1.2 for the orientation of the coordinate axes).

The hodoscope consists of two precision plates which are mounted at a distance of $\Delta y = 379.0$ mm onto two round steel bars. The TPC is placed between these plates (figure 6.2). The field cage is in a mounting frame with position pins. The active area of the hodoscope is only 93 mm in the z direction while the drift distance of the TPC is 26 cm. There are position holes at a distance of 60 mm in the steel rail which holds the mounting frame, so the field cage can be inserted at different z positions and the whole drift space can be examined.

The silicon modules are read out using the ARC system (**A**PV **R**eadout **C**ontroller), which was developed at the III. Physics Institute of RWTH Aachen [65]. The ARC board is the main component of the system, containing the FADCs, a 40 MHz clock generator and an input port for the trigger signal. The silicon modules are connected to the ARC board using a front end adapter board. The depletion voltage for the silicon sensor is provided by the **Dep**letion **P**ower high voltage board DEPP [66]. The ARC board as well as the DEPP can be controlled and read out via SRD[1] bus. The readout scheme of the TPC and the hodoscope is sketched in figure 6.3.

---

[1] **S**ynchroton **R**atiation **D**etector bus, a bus system developed for the SRD component of the AMS experiment
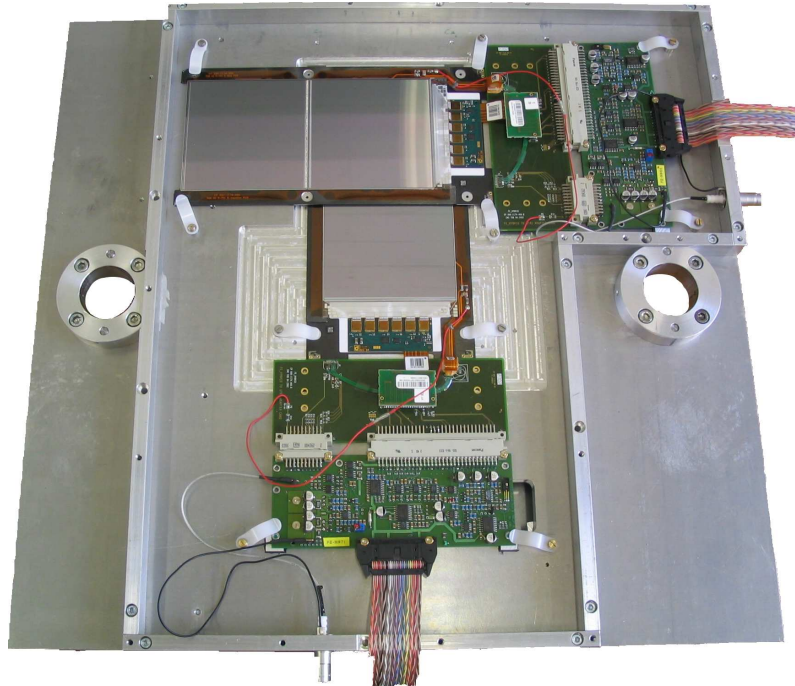
Figure 6.1: Precision plate of the hodoscope with two silicon strip modules mounted at an angle of 90 degrees with respect to each other.
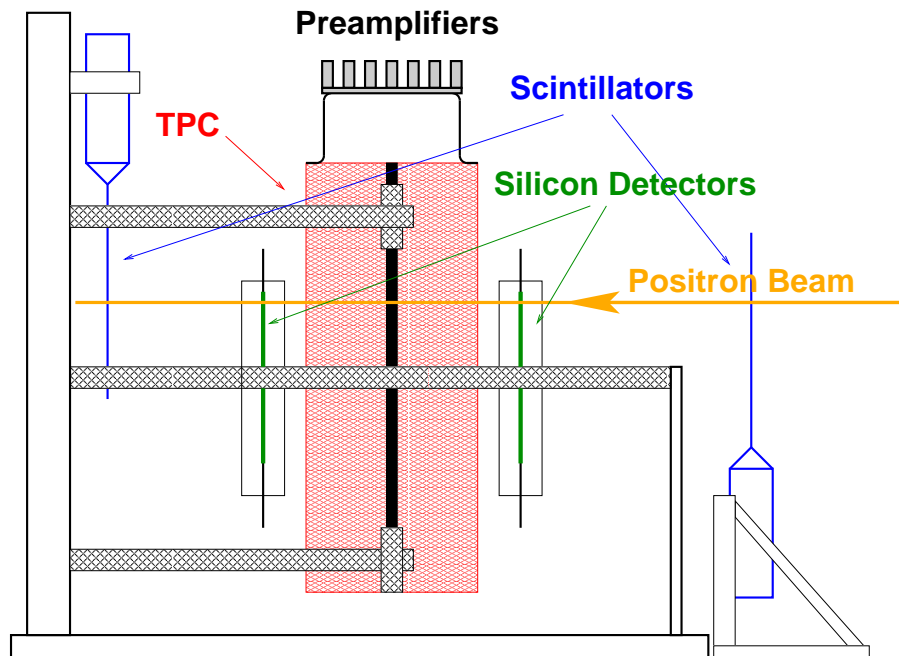

Figure 6.2: Schematics of the hodoscope test stand: The TPC is mounted between the two plates of the silicon hodoscope. Scintillation counters are used to trigger for the positrons.
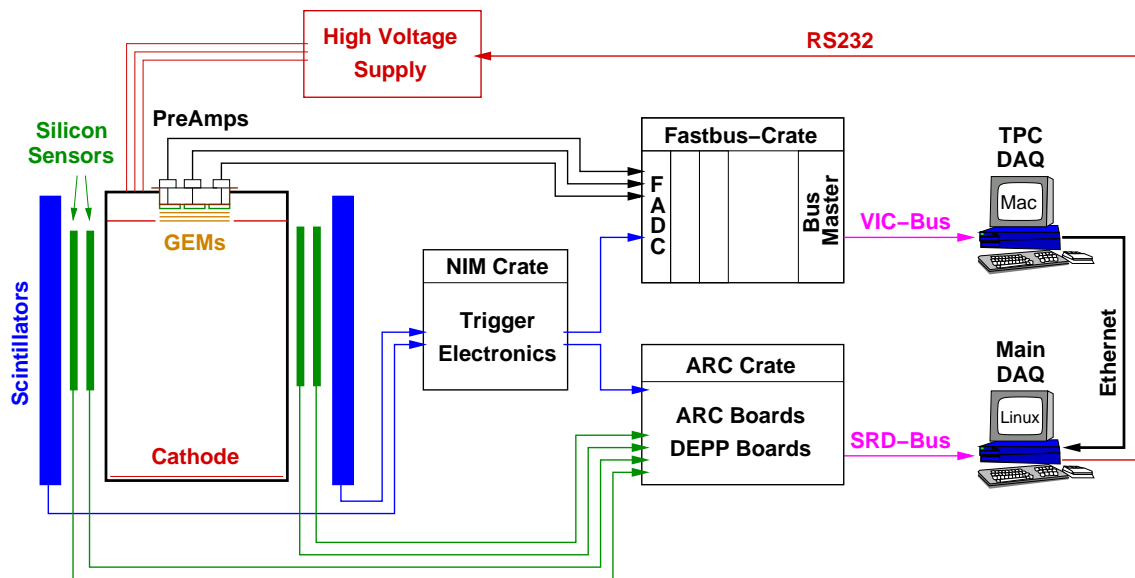
Figure 6.3: Readout scheme of the TPC and the hodoscope: The TPC is located between the silicon sensors of the hodoscope, which are surrounded by scintillation counters for triggering. The trigger signal is distributed to the FASTBUS crate, which reads out the TPC, and to the ARC crate, which takes the data from the silicon sensors. The Macintosh PC, reading the data from the FASTBUS crate, writes to the main Linux DAQ PC via Ethernet. The main DAQ PC does not only record the data of the TPC and the hodoscope, but also controls the high voltage.
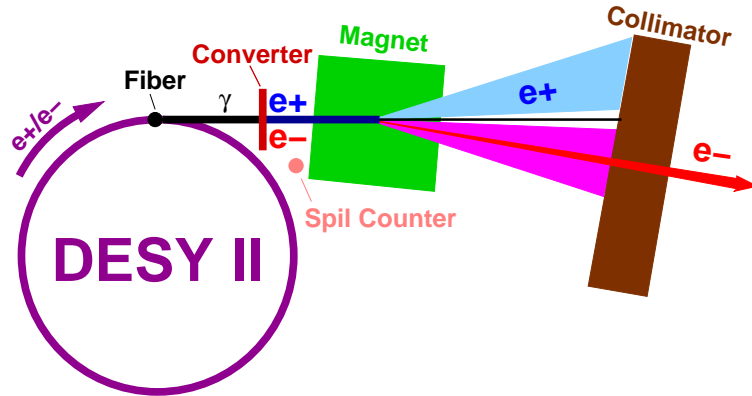
Figure 6.4: Schematic layout of the test beam generation at DESY [68].

The spatial resolution of the hodoscope was measured to be 44 μm, as described in reference [67], where a detailed description can be found.

6.1.1 Experimental Setup at the DESY Test Beam

The data presented in this thesis has been recorded at DESY Hamburg. DESY provides a test beam facility with a positron beam, which is tunable in an energy range of 1 to 6 GeV. The generation of the test beam is sketched in figure 6.4. A carbon fibre is placed in the electron/positron synchrotron DESY II. This generates bremsstrahlung, which hits an aluminium target. The electron-positron-pairs generated here are passing a spectrometer consisting of a magnet and a collimator. This allows to select one specific energy. The beam profile as measured with the hodoscope is shown figure 6.5. It has a square cross section due to the collimator shape.

The hodoscope system, including the TPC, is mounted onto translation stages, which allow to move the complete setup horizontally and vertically (figure 6.6). This corresponds to the x and the z direction of the hodoscope's coordinate system. The translation stages can be remote-controlled from the control booth, either manually or using the daemon program `testbeam_table_d`. This daemon receives commands via a TPC/IP connection, which allows the main DAQ application `ligros` to connect to the translation stage control and move the hodoscope automatically.

A bolt fixing the hodoscope on the ground plate enables the complete setup to be rotated around the centre of the TPC cylinder. This allows to vary the angle always hitting the centre of the active area in the TPC. The hodoscope has an active area of 80 mm in the x direction. Due to the lever arm of approximately 170 mm to the pivot axis this limits the rotation to small angles. In the presented measurements the angle has been varied in a range from -4° to +4°.

The trigger system is made up of two scintillation counters, one in front of and one behind the hodoscope, looking in beam direction. A simultaneous signal in both counters starts the data acquisition of both hodoscope and TPC. A mutual trigger inhibit circuit keeps both systems in sync (see section 6.2).
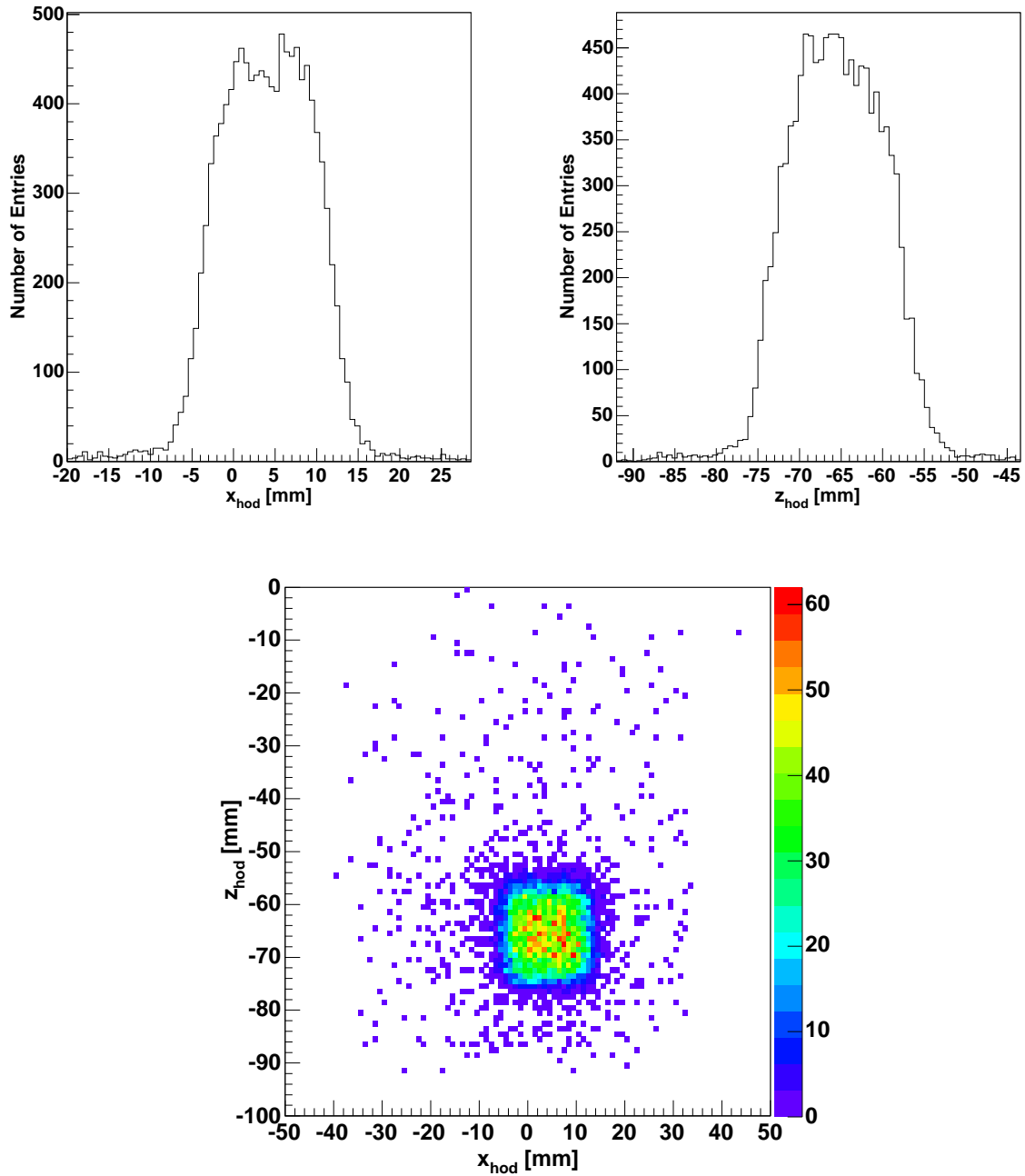
Figure 6.5: The profile of the DESY test beam measured with the hodoscope.
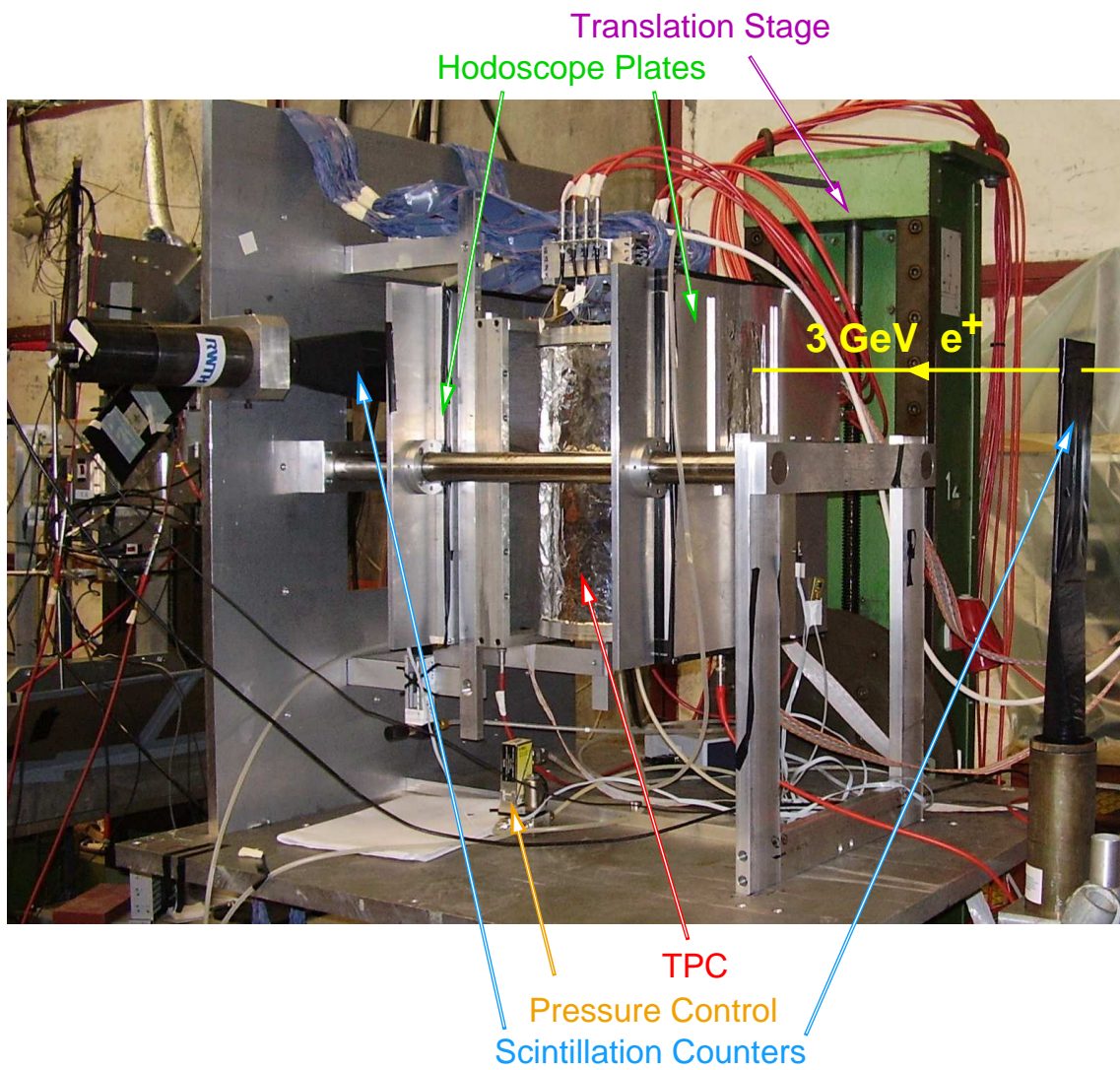
Figure 6.6: The TPC and the hodoscope mounted on a translation stage at the DESY test beam facility.
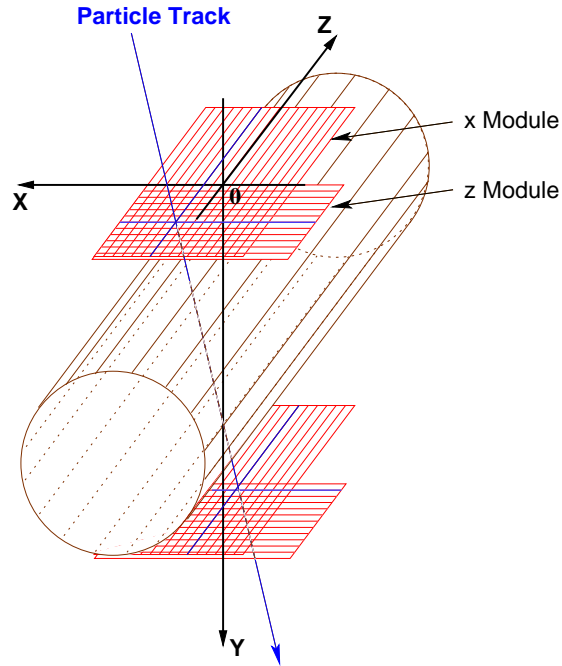
Figure 6.7: Schematic view of the four silicon strip modules. The origin is located in the upper x module.

6.1.2 Coordinate System and Track Parameters

In the y direction, the origin is placed at the position of the upper x module. The x origin is in the middle of the active x range of this module. $z = 0$ is at the back edge of the upper z module (in the perspective of figure 6.7). The orientations of the axes (x to the left, y downwards and z backwards in the figure) were chosen identical to the TPC coordinate system. Note that this is a left handed coordinate system.

As the x and the z modules are perpendicular to each other, these two coordinates are measured independently. Like in the TPC, the track is described by the two projections in the xy and in the zy plane:

$$x_{\mathrm{hod}} = a_{\mathrm{hod}} \cdot y_{\mathrm{hod}} + b_{\mathrm{hod}}$$
$$z_{\mathrm{hod}} = c_{\mathrm{hod}} \cdot y_{\mathrm{hod}} + d_{\mathrm{hod}}$$

The two measured x coordinates are just sufficient to calculate the two track parameters a and b:

$$a_{\mathrm{hod}} = \frac{x_2 - x_1}{\Delta y}$$
$$b_{\mathrm{hod}} = x_1$$

Accordingly for the z direction:

$$
\begin{aligned}
c_{\text{hod}} &= \frac{z_2 - z_1}{\Delta y} \\
d_{\text{hod}} &= z_1 - c_{\text{hod}} \cdot y_{z1}
\end{aligned}
$$

y_{z1} is the y coordinate of the upper z module.[2]

As there is no redundancy in the measurement, all four modules have to be hit. Having additional signals like noise hits causes ambiguities which cannot be resolved. Hence a valid hodoscope track can only be reconstructed if there is exactly one hit in each of the modules.

6.1.3 The Linux Graphical Readout Software `ligros`

The program `ligros` was originally developed only as slow control and DAQ software for the silicon modules [60]. For this purpose a daemon called `arcd` running on the DAQ computer controls the ARC crate. It receives commands from the `ligros` graphical user interface via TPC/IP.

To enable an extensively automated operation at the test beam, `ligros` has been expanded to be the main measuring application. It now allows to

- start and stop the `fastdaq` software of the TPC.

- transmit new voltages to the TPC's slow control software `xtc`.

- move the translation stages in the test beam area.

- read out the hodoscope.

- set the depletion voltages for the silicon modules.

The TPC programs `fastdaq` (see section 4.3) and `xtc` (see section 4.5) are stand-alone applications with their own user interface. They both can be operated in a special mode, which continuously scans for steering files containing new commands to be executed. `ligros` controls the TPC software via these files.

`arcd` can handle a script which controls all actions needed during a data run:

- Recording a given number of events

- Moving the translation stage

- Pausing, in case manual user interaction on the experiment is needed

`ligros` itself can run a master script which allows to transmit new voltages to `xtc` and start a new data run. Figure 6.8 gives an overview of the data acquisition and slow control software.

---

[2]There is no y_{x1} in the formula for the x direction as the upper x module was defined as $y = 0$.
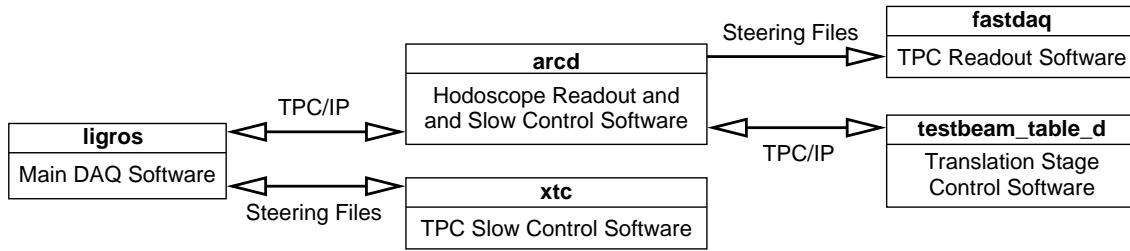
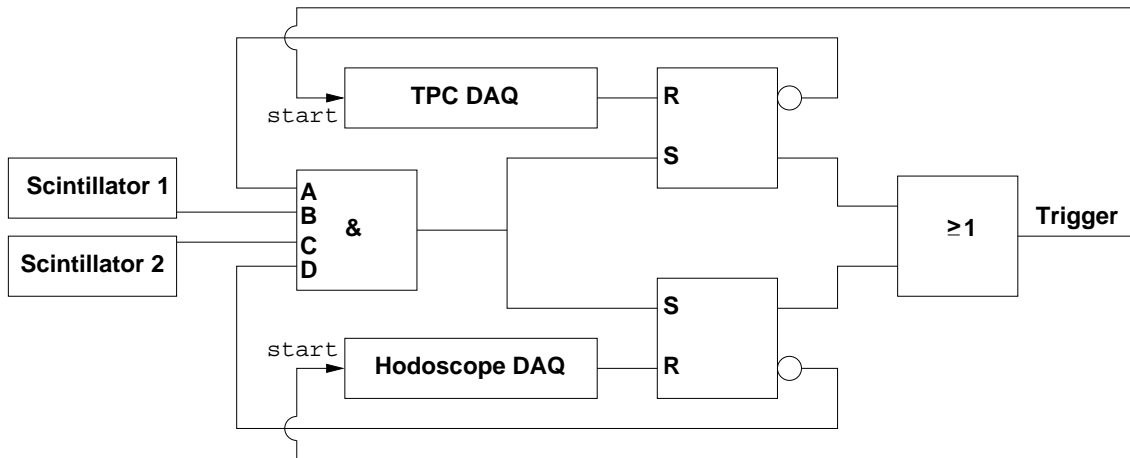Figure 6.8: Visualisation of the communication between the data acquisition and slow control software modules.

Figure 6.9: Scheme of the mutual trigger inhibit circuit.

6.2 Trigger Synchronisation

The TPC and the hodoscope are read out by two autonomous DAQ programs, `fastdaq` and `ligros`. To compare these two measurements, it has to be assured that the recorded trigger numbers are identical. This means that both systems have to be able to inhibit the trigger while an event is read out. The next trigger is only accepted if both systems are ready to record a new event. This is realised by two bistable multivibrators[3] (flip-flops) ⌷. The scheme of the trigger inhibit circuit is shown in figure 6.9.

The system is ready to accept a trigger if both flip-flops have been reset. This means the negated outputs (marked with ∘) are active (logic level 1). They are connected to the inputs **A** and **D** of a four-fold coincidence[4] ⌷. If there is a simultaneous signal on both scintillators, all inputs of the coincidence are active and the output goes to 1. This sets both flip-flops, which has two effects:

---

[3]A *bistable multivibrator* or *flip-flop* is a module with two inputs, `Set` and `Reset`. If `Set` is 1, the output is 1. This state is preserved until `Reset` becomes active and the output goes to 0. This state is also preserved until the flip-flop is set again (bistable).

[4]A coincidence is a logical `AND` gate. The output is 1 only if all the inputs are active.

1. The outputs of the flip-flops go to `1` as well as the output of the `OR` gate `≥1`. This is the trigger signal which starts both DAQ systems.

2. The negated flip-flop outputs go to `0` and the coincidence will give no more signals.

After the TPC DAQ is finished, it resets the corresponding flip-flop and input **A** of the coincidence goes back to `1`. The same happens accordingly for the hodoscope DAQ. After both flip-flops have been reset, the system is ready to accept the next trigger.

6.3 Calibration of the TPC in the Hodoscope

Both the TPC and the hodoscope provide independent measurements in their own coordinate system. As the hodoscope has the better spacial resolution, it is taken as the reference system and the TPC data is transformed into the hodoscope's coordinate system to compare results.

The TPC is treated as a rigid body, deformations and torsions are not considered. Therefore the calibration is a transformation from one Cartesian coordinate system into another. The TPC coordinate system has an offset in all three spatial directions and can be rotated around three axes with respect to the hodoscope. As the TPC measures the z coordinate as time, the drift velocity has to be known to calculate the actual drift distance. This results in seven parameters describing the calibration of the TPC in the hodoscope:

- Offset in the x direction (x_{off})

- Offset in the y direction (y_{off})

- Offset in the z direction (z_{off})

- Angle in the xy plane ($\Delta\phi_{xy}$)

- Angle in the zy plane ($\Delta\phi_{zy}$)

- Angle in the xz plane ($\Delta\phi_{xz}$)

- Drift velocity (v_{d})

In terms of these parameters, the transformation of the TPC data into the hodoscope's coordinate system can be written as

$$
\begin{pmatrix} x' \\ y' \\ z' \end{pmatrix} = \begin{pmatrix} x_{\text{off}} \\ y_{\text{off}} \\ z_{\text{off}} \end{pmatrix}
$$

$$
+ \begin{pmatrix} c_{xz} & 0 & s_{xz} \\ 0 & 1 & 0 \\ -s_{xz} & 0 & c_{xz} \end{pmatrix} \begin{pmatrix} 1 & 0 & 0 \\ 0 & c_{zy} & s_{zy} \\ 0 & -s_{zy} & c_{zy} \end{pmatrix} \begin{pmatrix} c_{xy} & s_{xy} & 0 \\ -s_{xy} & c_{xy} & 0 \\ 0 & 0 & 1 \end{pmatrix} \begin{pmatrix} x_{\text{TPC}} \\ y_{\text{TPC}} \\ v_{\text{d}}\, t_{\text{TPC}} \end{pmatrix} \tag{6.1}
$$

c_{xy} is short for $\cos \phi_{xy}$, s_{xy} for $\sin \phi_{xy}$. The same convention is used for ϕ_{zy} and ϕ_{xz}, respectively. This transformation defines the order of the rotations.[5] Note the sign of the sine which was chosen this way because of the left handed coordinate systems.

To determine the parameters, a χ^2 minimisation is performed which minimises the mean distance of the measured TPC points to the respective hodoscope track. For this purpose, special calibration runs are recorded, where the beam angle in the xy plane and the z coordinate are varied. This is necessary to guarantee sensitivity to all seven parameters. Each time the TPC position in the hodoscope is changed, a new calibration run has to be performed. The data presented in the following sections is an example for one of these calibration runs.

6.3.1 Pre-Calibration

To get a starting point for the minimisation, a pre-calibration is performed. This method only works for small angles between the TPC and the hodoscope coordinate system. The reason for this is the following: The first parameter to be applied in formula 6.1 is the drift velocity v_{d}, otherwise the rotations in the zy and xz plane cannot be calculated. However, in the pre-calibration, the drift velocity can only be determined after calculating y_{off}: v_{d} is calculated from the z coordinates of the TPC and the hodoscope, and since these are parameterised as a function of y, y_{off} has to be known to compare them. This problem can be solved by utilising the fact that the angles between the coordinate systems are small and so the rotations can be neglected in first approximation.

The pre-calibration only uses the four *track* parameters a, b, c and d from the TPC and the hodoscope, but does not use the information of the individual *points* measured by the TPC. There are four steps in the pre-calibration:

1. Determine $\Delta\phi_{xy}$

2. Determine x_{off} and y_{off}

3. Determine v_{d} and z_{off}

4. Determine $\Delta\phi_{zy}$

The third angle $\Delta\phi_{xz}$ cannot be calculated using only the track parameters, as the parametrisation only provides one angle in the xy and one in the zy plane.

Calculation of $\Delta\phi_{xy}$

The angle of a measured track in the xy plane is $\phi_{xy} = \arctan a$. The angle between the TPC and the hodoscope track is $\Delta\phi_{xy} = (\phi_{xy})_{\mathrm{hod}} - (\phi_{xy})_{\mathrm{TPC}}$. The mean $\Delta\phi_{xy}$ and its error as well as the width of the distribution are determined from a fit to the histogrammed data (figure 6.10). The Gaussian fit is applied in a range of ± 1.3 RMS

---

[5]The rotation matrices only commute in the small angle approximation. If the order of the matrices is fixed, the transformation is valid for all angles.
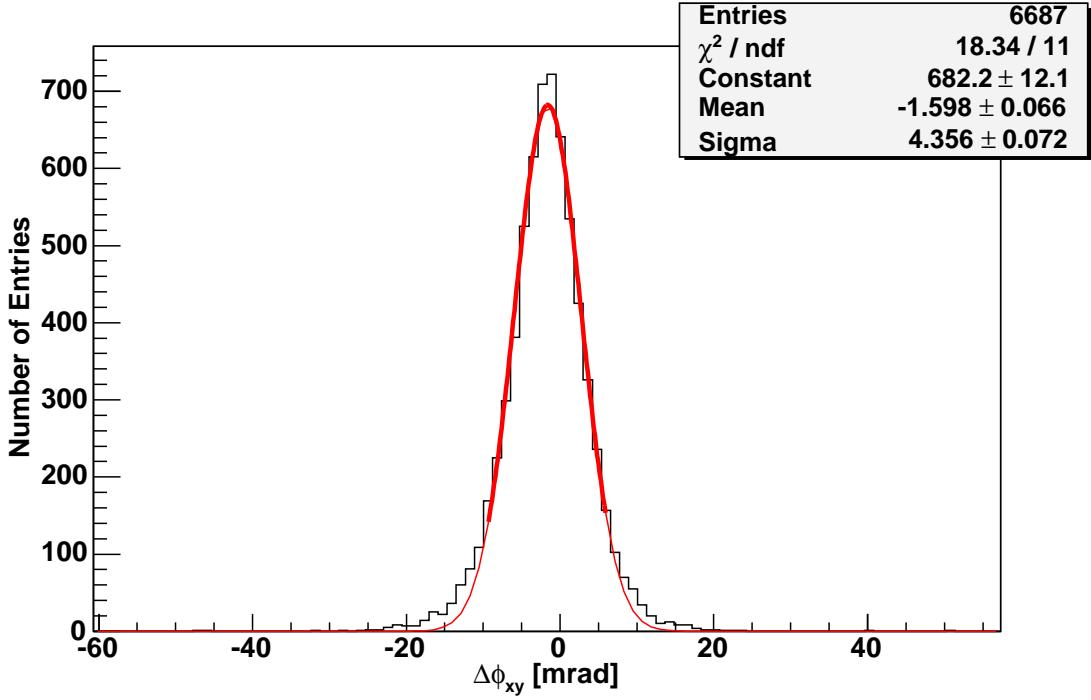
Figure 6.10: Distribution of the difference of the angles ϕ_{xy} measured with the hodoscope and the TPC.

around the arithmetic mean of the distribution.

In some cases the tracks in the TPC and the hodoscope do not match, for example if the particle hits a bad strip in the hodoscope, but there is noise in another channel of the same module. The matching is also wrong if the real track in the TPC can not be reconstructed, but there is an off-trigger track. To cut away these outliers, only the tracks within a 3 σ range around the mean value of the fit are flagged as valid and used in the next steps.

Calculation of the offsets x_{off} and y_{off}

After correcting the rotation $\Delta\phi_{xy}$, the slope a should be identical for the hodoscope and the TPC. The axis intercept b transforms as follows (see figure 6.11):

$$b_{\text{TPC}} = b_{\text{hod}} + a \cdot y_{\text{off}} + x_{\text{off}}$$

From this equation one can see that plotting the difference of b_{TPC} and b_{hod} against a is expected to give a straight line with a slope of y_{off} and an ordinate intercept x_{off}:

$$b_{\text{TPC}} - b_{\text{hod}} = a_{\text{hod}} \cdot y_{\text{off}} + x_{\text{off}}$$

In this case the value a is taken from the hodoscope, because it has a smaller angular spread than the TPC measurement. Figure 6.12 shows the distribution $b_{\text{TPC}} - b_{\text{hod}}$
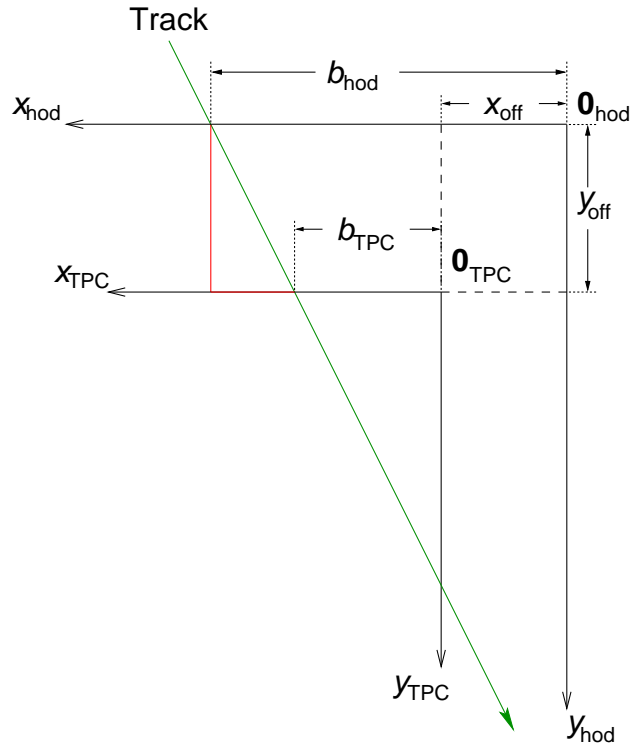
Figure 6.11: Illustration of the offsets between the TPC and the hodoscope coordinate system and the transformation of the track parameter b.

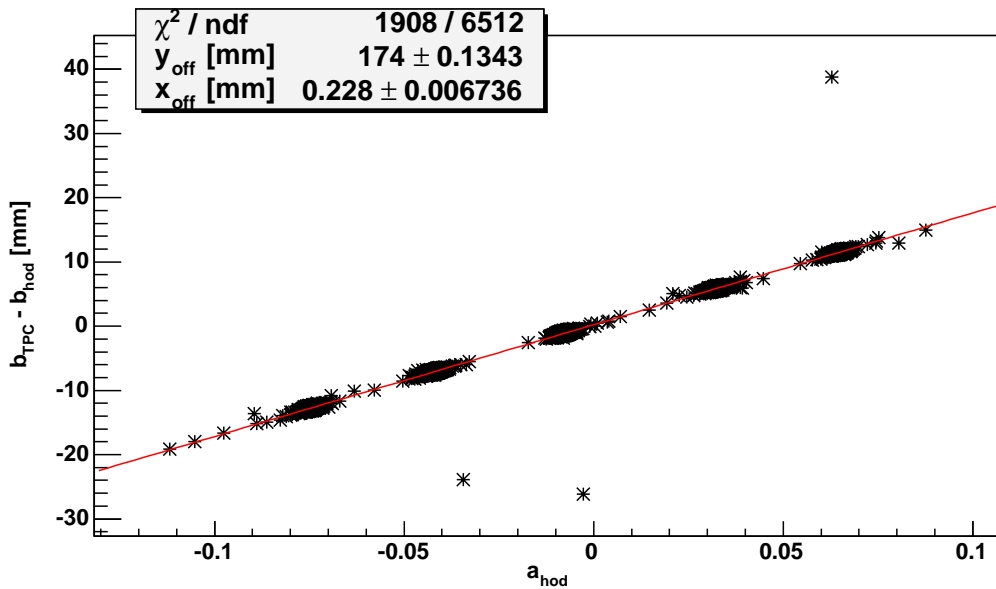Figure 6.12: $b_{\mathrm{TPC}} - b_{\mathrm{hod}}$ versus a. Mismatching of tracks between the hodoscope and the TPC causes tree outliers.
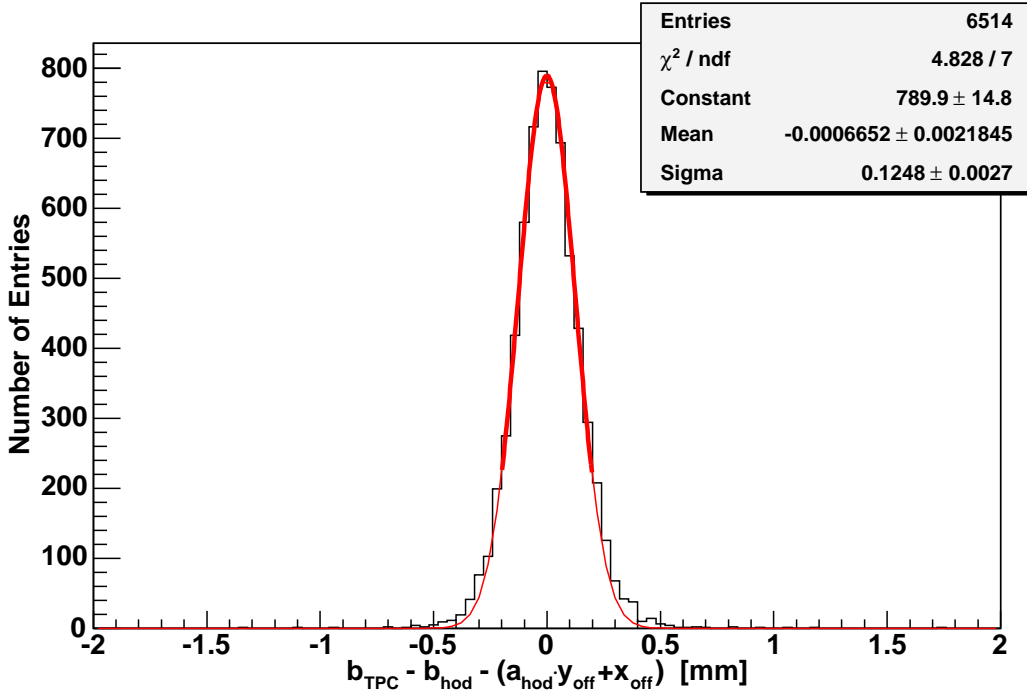
Figure 6.13: The distance of $b_{\text{TPC}} - b_{\text{hod}}$ to the fitted straight line.

versus a. To cover a sufficiently large range in a, special calibration measurements with five different angles have been run in the test beam. One can clearly see the five different values of a in the plot. Again, there are some outliers which are caused by non-matching tracks. To cut them away, the vertical distance of each point to the straight line, $b_{\text{TPC}} - b_{\text{hod}} - (a_{\text{hod}} \cdot y_{\text{off}} + x_{\text{off}})$, is histogrammed (figure 6.13). Again a Gaussian is fitted to the ± 1.3 RMS range and all tracks outside the $3\,\sigma$ range around the Gaussian's mean value are cut away. After applying this cut, the straight line is refitted (figure 6.14).

Calculation of the drift velocity and z_{off}

Now that y_{off} is known, one can calculate the z position of the TPC track at $y_{\text{hod}} = 0$:

$$\tilde{d}_{\text{TPC}} = c_{\text{TPC}} \cdot y_{\text{off}} + d_{\text{TPC}}$$

Note that $\tilde{d}_{\text{TPC}}$ is in units of time. Plotting d_{hod}, which is the z position of the hodoscope at $y = 0$, against $\tilde{d}_{\text{TPC}}$ is expected to yield a straight line with the drift velocity as slope and an ordinate intercept of z_{off} (figure 6.15). After a first fit, the tracks outside the $3\,\sigma$ range around the straight line are cut away again and v_{drift} and z_{off} are refitted.
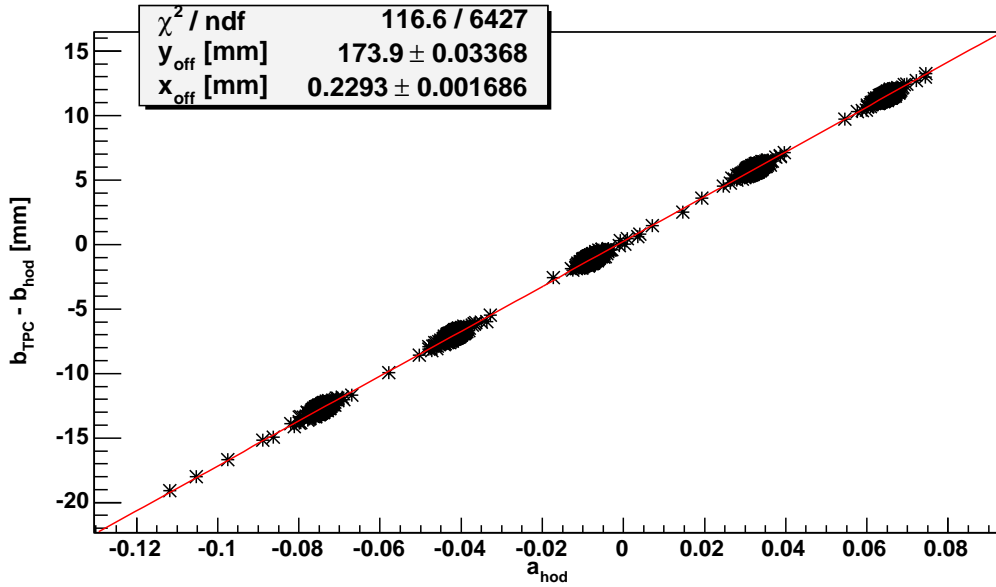
Figure 6.14: After cutting away the outliers, x_{off} and y_{off} are refitted.
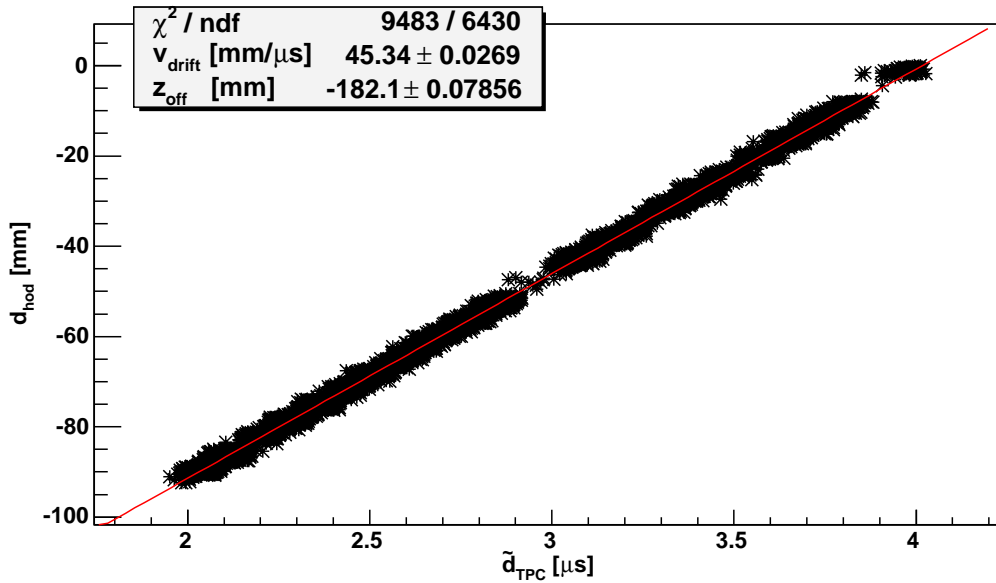

Figure 6.15: The z position at $y = 0$ in the hodoscope against the z coordinate from the TPC gives a straight line with the drift velocity as slope.
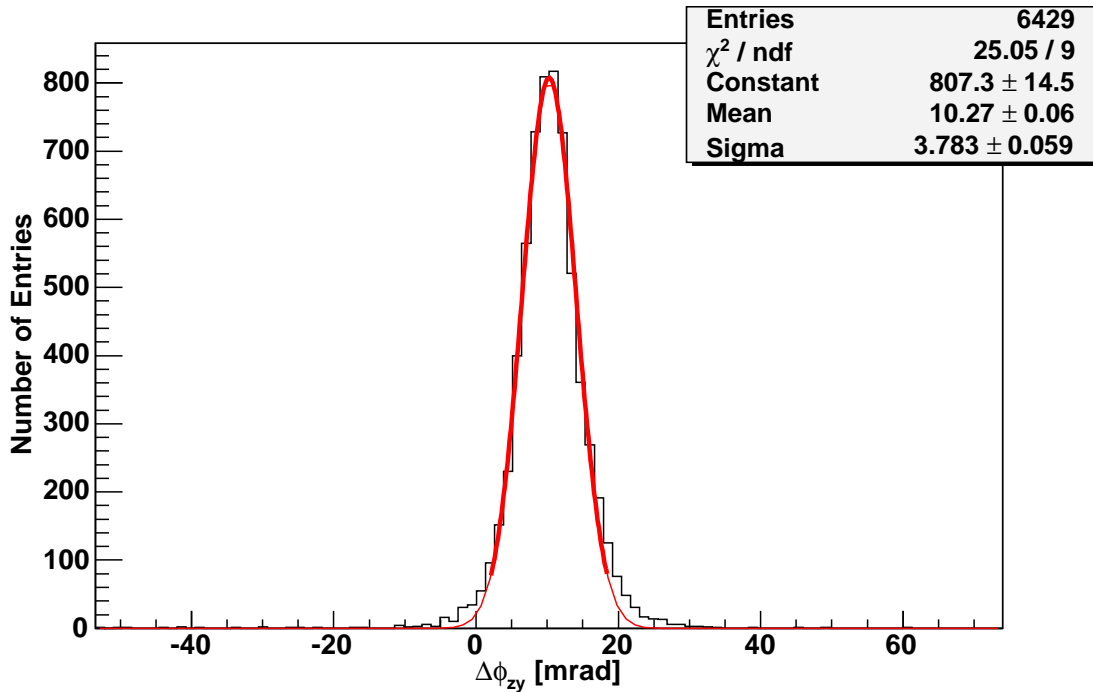
Entries	6429
χ^2 / ndf	25.05 / 9
Constant	807.3 ± 14.5
Mean	10.27 ± 0.06
Sigma	3.783 ± 0.059

Figure 6.16: Distribution of the difference of the angles ϕ_{zy} measured with the hodoscope and the TPC.

Calculation of $\Delta\phi_{zy}$

After applying the drift velocity, the last parameter of the pre-calibration, the angle $\Delta\phi_{zy}$, can be calculated. Like the angle in the xy plane, it is determined by fitting a Gaussian to the range of ± 1.3 RMS of the $\arctan(\phi_{zy})_{\text{hod}} - \arctan(\phi_{zy})_{\text{TPC}}$ distribution (figure 6.16). Again, only the tracks within the $3\,\sigma$ interval around the mean value are flagged as valid.

6.3.2 Final Calibration

In a last step x_{off}, y_{off}, z_{off}, v_{drift} and $\Delta\phi_{xz}$ are optimised simultaneously, using a χ^2 minimisation. A check of the track parameters after the calibration (see next section) has shown that the two remaining angles ϕ_{xy} and ϕ_{zy} are not determined well if included in the fit. The reason for this is the small dependence of the χ^2 function on these angles. The pre-calibration can measure angles more accurately because the rotation is done in the centre of the TPC, while the intercept parameter is determined in the upper layer of the hodoscope. This introduces a lever arm of approximately 170 mm, resulting in a good sensitivity to the angles. Thus, $\Delta\phi_{xy}$ and $\Delta\phi_{zy}$ are fixed to the values obtained from the pre-calibration.

The fit minimises the squared distance in the xz plane of each individual point measured in the TPC to the hodoscope track. As x and z are measured inde-

pendently, the variables are weighted separately with their respective errors. The function to be minimised is

$$\chi^2 = \sum_i \left[\left(\frac{x_i' - a_{\mathrm{hod}}\, y_i' - b_{\mathrm{hod}}}{(\sigma_x)_i} \right)^2 + \left(\frac{z_i' - c_{\mathrm{hod}}\, y_i' - d_{\mathrm{hod}}}{(\sigma_z)_i} \right)^2 \right]$$

where x_i', y_i' and z_i' are the coordinates of the TPC point in the hodoscope coordinate system and a_{hod}, b_{hod}, c_{hod}, d_{hod} are the track parameters measured by the hodoscope. $(\sigma_x)_i$ is the σ_x of the ith point. It consists of the errors in the TPC and the hodoscope: $\sigma_x = \sqrt{(\sigma_x)_{\mathrm{TPC}}^2 + (\sigma_x)_{\mathrm{hod}}^2}$. The error of the individual points cannot be determined well enough with this reconstruction method. Therefore the $(\sigma_x)_{\mathrm{TPC}}$ is taken from the reconstructed TPC track, which means it is the mean error of all the points on the specific track. This should be a good estimate for the individual $(\sigma_x)_{\mathrm{TPC}}$. The same holds for $(\sigma_z)_{\mathrm{TPC}}$, respectively.

For those measurements performed without ADC jitter correction, the error in the z direction is mainly determined by this jitter (see section 6.5). In this case the error of the hodoscope can be neglected and instead the statistical error of the jitter is taken, which is $\frac{t_{\mathrm{s}}}{\sqrt{12}} v_{\mathrm{drift}}$. t_{s} is the length of one time sample, 80 ns in our case. For the $\mathrm{Ar}/\mathrm{CO_2}/\mathrm{CH_4}$ 93/2/5 gas mixture with $v_{drift} = 45 \frac{\mathrm{mm}}{\mathrm{\mu s}}$ the error is $(\sigma_z)_{\mathrm{ADC}} \approx 1$ mm.

6.3.3 Accuracy of the Calibration

To verify the calibration and determine its precision two things can be checked:

1. The track parameters a, b, c and d have to be the same for the TPC and the hodoscope.

2. The residuals $\Delta x = x_{\mathrm{TPC}}' - a_{\mathrm{hod}} \cdot y_{\mathrm{TPC}}' - b_{\mathrm{hod}}$ and $\Delta z = z_{\mathrm{TPC}}' - c_{\mathrm{hod}} \cdot y_{\mathrm{TPC}}' - d_{\mathrm{hod}}$ must be distributed around zero.

This also has to hold for the measurements which are not used to generate the calibration, but a calibration from another measurement is applied. The following data is taken from such a measurement.

Test of the track parameters

Figures 6.17 and 6.18 show the difference between the track parameters of the TPC and the hodoscope in the xy and the zy plane, respectively. If the calibration is correct, they all should be distributed around zero. Instead of the difference of the slopes Δa the difference of the angles $\Delta \phi_{xy} = \arctan(a_{\mathrm{hod}}) - \arctan(a_{\mathrm{TPC}})$ is shown, because it is more intuitive.

The mean of the $\Delta \phi_{xy}$ distribution is off by -115 ± 91 µrad. Within the 10 cm large active area of the TPC, this causes a systematic shift of 12 µm between the first and the last measured point.
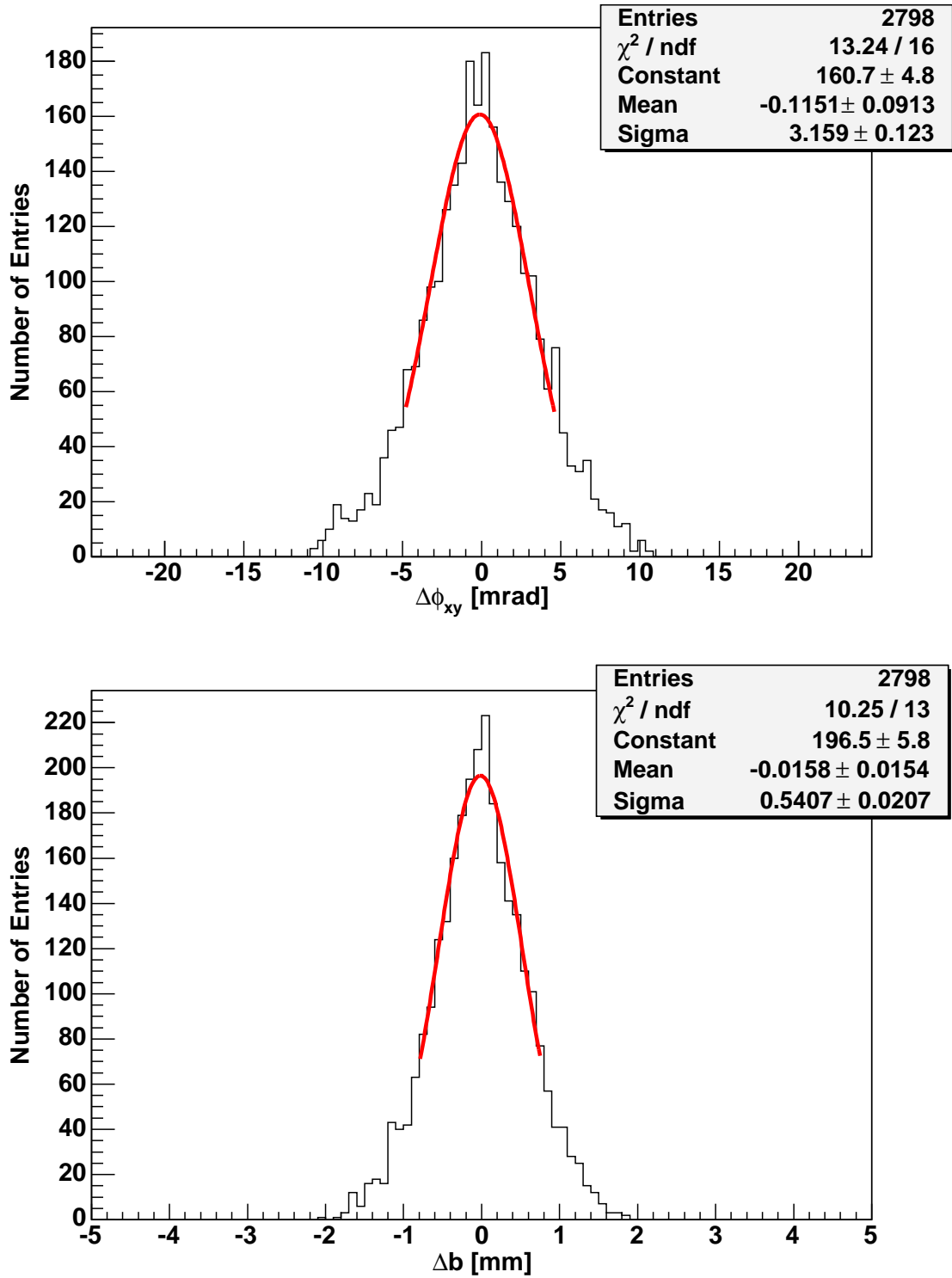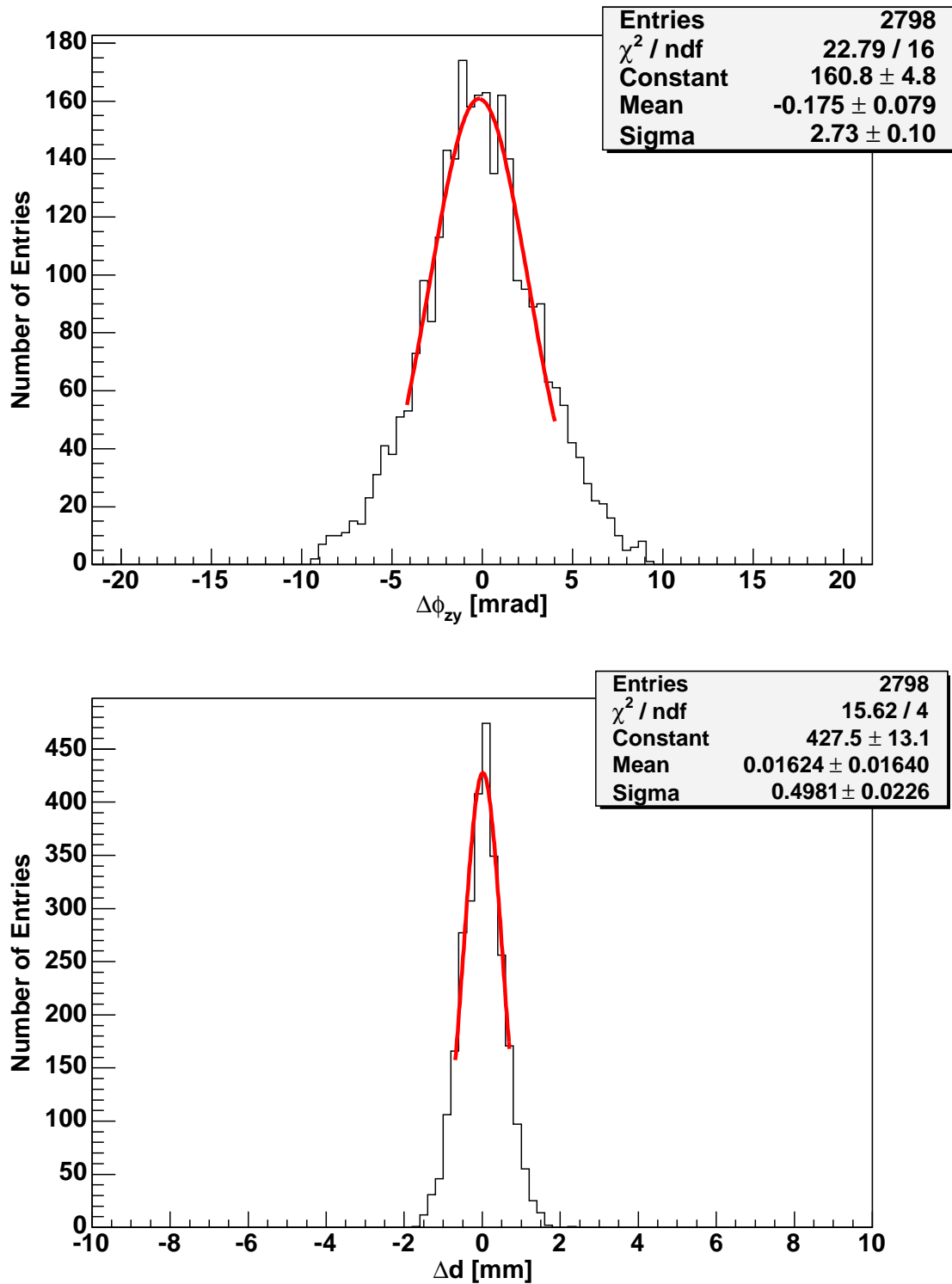
Figure 6.17: Difference of the angle in the xy plane ϕ_{xy} and the x axis intercept b between the hodoscope and the TPC after the calibration.

Entries	2798
χ^2 / ndf	22.79 / 16
Constant	160.8 ± 4.8
Mean	-0.175 ± 0.079
Sigma	2.73 ± 0.10

Entries	2798
χ^2 / ndf	15.62 / 4
Constant	427.5 ± 13.1
Mean	0.01624 ± 0.01640
Sigma	0.4981 ± 0.0226

Figure 6.18: Difference of the angle in the zy plane ϕ_{zy} and the z axis intercept d between the hodoscope and the TPC after the calibration.

The mean Δb is -16 ± 15 µm, which is compatible with zero. For $y_{\mathrm{off}} = 174$ mm and an angle $\Delta\phi_{xy} = -115$ µrad one expects an offset of 20 µm. This is because the rotation in the xy plane is performed around the TPC axis, and then b'_{TPC} is determined in the upper hodoscope module. So Δb systematically depends on $\Delta\phi_{xy}$. The same applies to Δd and $\Delta\phi_{zy}$.

$\Delta\phi_{zy}$ is off by -175 ± 79 µrad. This corresponds to a shift of 18 µm within the readout area of the TPC. Again, the difference in the axis intercepts is compatible with zero ($\Delta d = 16 \pm 16$ µm).

Test of the Residual Distributions

After applying the calibration, both the TPC and the hodoscope data are in the same coordinate system and can be compared directly. The distances of the measured x and z coordinates in the TPC to the corresponding point on the hodoscope track, i.e. the point with the same y coordinate, are depicted in figure 6.19. One can see that the residuals are nicely distributed around zero. The mean value in x is off by 3 µm, in z by 4 µm only. This shows that the calibration is working very well. The systematic deviations are much smaller than the resolution of the hodoscope (44 µm) and particularly than the resolution of the TPC.

6.4 Measurement of the Absolute TPC Position

Δz is not the absolute mechanical offset between the TPC and the hodoscope. The TPC measures the z coordinate in time. Only in the drift volume with its homogeneous electric field the relation $z = t \cdot v_{\mathrm{drift}}$ holds. But the time measured also contains the time the electrons need to pass the GEM structure, which even varies with the GEM settings, and a constant offset caused by the electronics.

One way to determine the real drift distance is measuring the position of the first GEM with the hodoscope. This can be done by looking at the "shadow" of the electrical shield on the hodoscope module behind the TPC if the readout structure is placed in the beam (see figure 6.20). The positron beam cannot penetrate the brass plate, so in the 3 mm wide area behind the shield there should be no signal in the hodoscope. Figure 6.21 shows the number of hits in the hodoscope for such a measurement. One can clearly see two gaps in the distribution. The dip from -60 to -57 mm is caused by the pickup board, the one from -54 to -49 mm by the brass shield.

To determine the centre of the shadow, the distribution is "inverted". To do so, all histogram values are subtracted from 50. The positive values are written to a new histogram, the negative ones are neglected. The mean value of the resulting distribution (figure 6.22) is -51.52 ± 0.03[6] mm. The width of the distribution is

---

[6]The given error is only the statistical error of the histogram. The accuracy of the z positions calculated later are limited by the repositioning precision of the TPC inside the hodoscope, which is about ± 1 mm.

Figure 6.19: Distributions of the residuals Δx and Δz (histograms normalised to one).
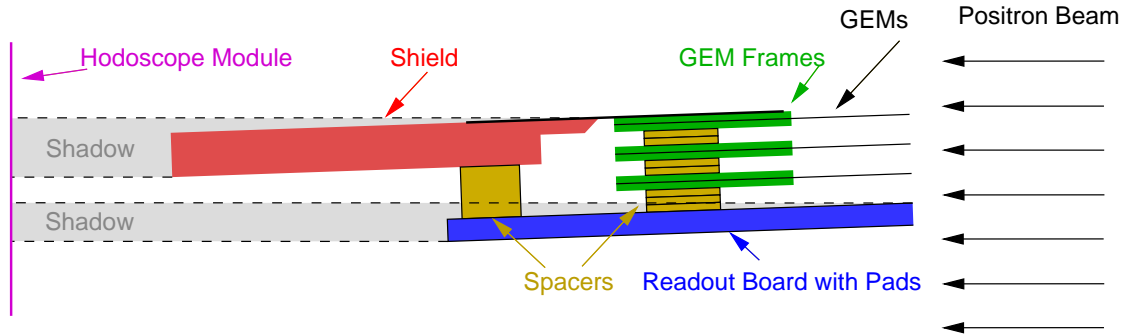
Figure 6.20: The readout structure in the positron beam. The positrons cannot penetrate the shield and the readout board, which causes "shadows" on the hodoscope module. As the readout structure is tilted by a small angle, the shadows are broadened a little bit.
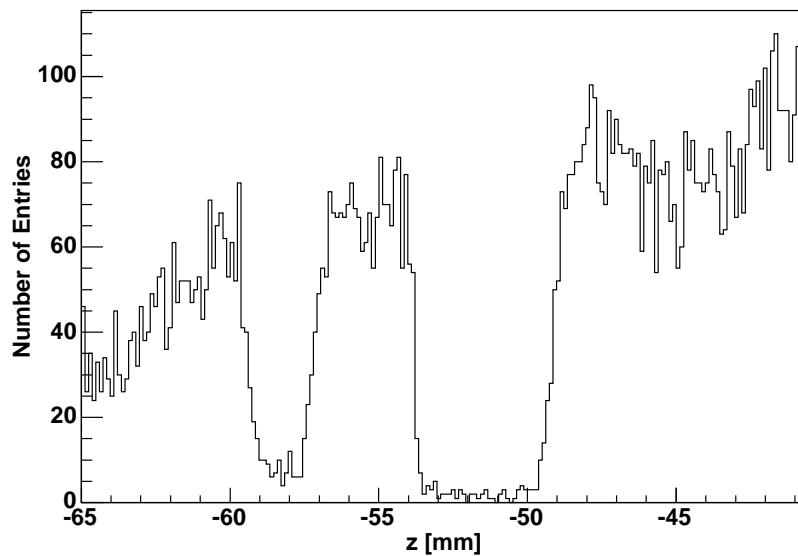

Figure 6.21: The number of hits in the hodoscope module behind the TPC with the readout structure placed in the beam. There are gaps in the distribution at the position of the readout board and of the brass shield.
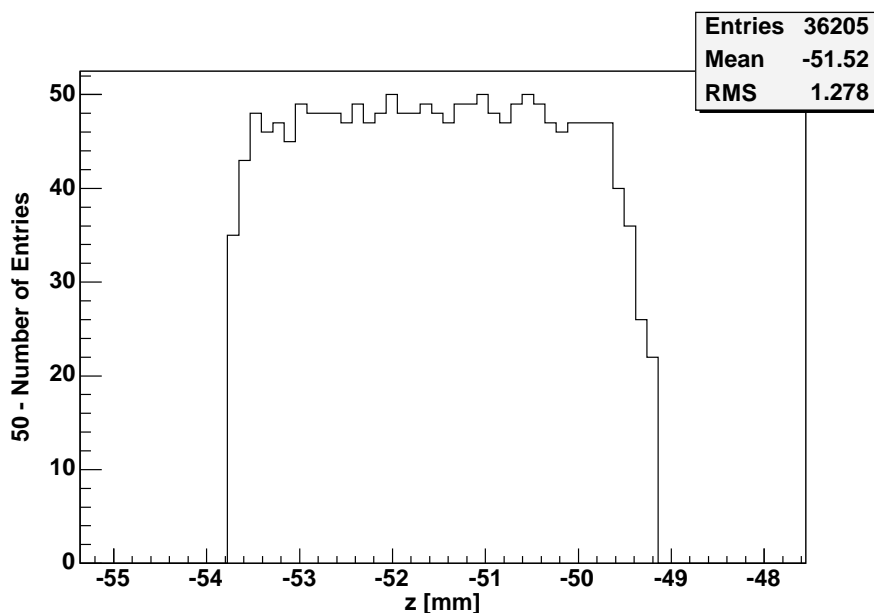
Figure 6.22: The "inverted shadow" of the shield allows to determine the centre of the shield in the hodoscope.

greater than the 3 mm thickness of the shield. This can be understood because the chamber is tilted by 10 mrad against the hodoscope. On the 227 mm diameter this broadens the shadow by 2 mm. However, it has no influence on its mean value. The first GEM has a mechanical offset of 1 mm with respect to the shield's centre. This means the position of the first GEM is -50.52 mm in hodoscope coordinates.

This method can only be used in the one special chamber positions where the shield is within the active area of the hodoscope. For the other chamber position the nominal mechanical offset in multiples of 60 mm is added. This is only accurate to a precision of about 1 mm. The time offset may vary from measurement to measurement due to the different amounts of time the electrons need to pass the GEM structure. It depends on the GEM setting and especially on the gas mixture. For the comparison of the TPC data with the hodoscope data this does not matter, it is calibrated away. But most plots in the following chapters show absolute drift distances. These values depend on this measurement and thus are only precise to ± 1 mm.

6.5 Test of the ADC Jitter Correction

The jitter between the trigger and the TPC clock as described in section 5.2 cannot be observed looking only at the TPC data. However, comparing with the hodoscope tracks, the offset of the TPC data becomes visible. The jitter shifts the measured TPC points uniformly within a range of one time sample, which should result in a rectangular shape. For the gas mixture used (Ar/CO2 98/2), which has a drift

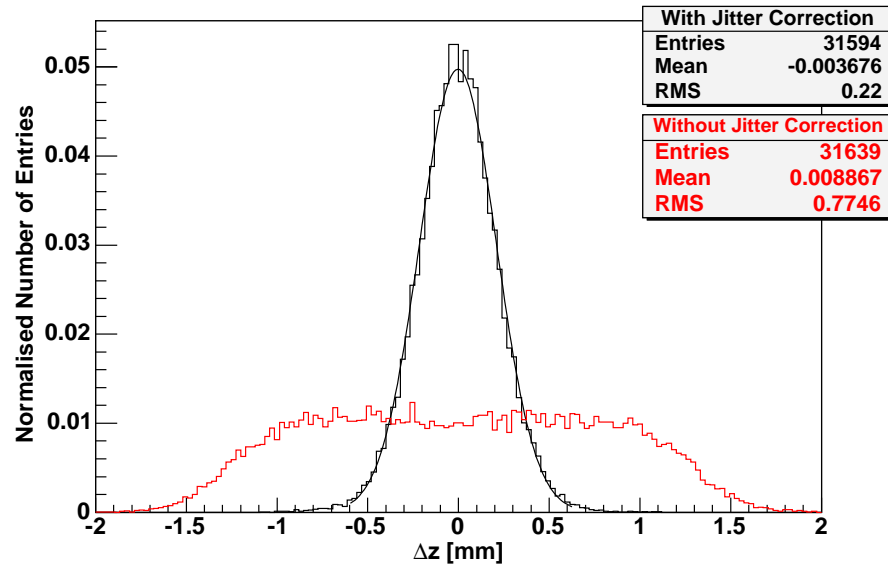Figure 6.23: The measured residuals in z with and without jitter correction (distributions normalised to one).

velocity of 36 mm/µs, the width of one time bin is 2.9 mm. The rectangular function is smeared with the resolution, which leads to a distribution reaching from -1.7 mm to $+1.7$ mm with a flat part from -0.9 mm to $+0.9$ mm in figure 6.23.

The distribution with jitter correction fits a Gaussian very well. This shows that the jitter correction is working and the spatial resolution of the TPC in the z direction can be measured using the hodoscope.

7 Field Homogeneity of the Field Cage

The field cage was designed to have an electric field homogeneity of better than 10^{-4}. The hodoscope provides the possibility to measure the field homogeneity by comparing the TPC tracks with an independent measurement.

7.1 Measurements of the Field Homogeneity

The field homogeneity in the z direction can be determined calculating the difference between the z coordinates measured by the TPC (affected by inhomogeneities) and the hodoscope (the coordinate assumed as correct):

$$\Delta z = z_{\mathrm{TPC}} - z_{\mathrm{hodoscope}}$$

The drift velocity depends on the electric field and thus on the z coordinate, if E changes with z. The drift time is $\int_0^z v_{\mathrm{drift}}(z')\,\mathrm{d}z'$. Knowing the dependence of the drift velocity on the electric field $v_{\mathrm{drift}}(E)$, one can calculate the field.

Figure 7.1 shows $v_{\mathrm{drift}}(E)$ as calculated by `Magboltz` [44]. To achieve maximum sensitivity for variations of the electric field, the measurements in this section have been performed at the steepest slope, which is at 80 V/cm for $\mathrm{Ar/CO_2/CH_4}$ 93/2/5. The gradient is $\frac{\mathrm{d}v_{\mathrm{drift}}}{\mathrm{d}E} = 0.32 \pm 0.01 \frac{\mathrm{mm/\mu s}}{\mathrm{V/cm}}$ at this point, the drift velocity is 23.45 mm/µs. As the variations of the field are small, the dependence is assumed to be linear.

7.1.1 Variation of the Shield Voltage

The position of the first GEM and the electrical shield are only known to ± 1 mm due to mechanical inaccuracies in the GEM stack. They are mainly caused by the manual glueing of the GEMs and the flection of the GEM frames. This mispositioning against the field cage causes distortions of the electric field near the readout plane. This can be adjusted by applying a voltage between the shield and the first strip of the field cage.

In the ideal case the upper side of the shield should be aligned to the middle of the first field strip (see figure 4.6). Due to some changes in the design, an offset of 1.5 mm was introduced between the shield and the first field strip. This results in a voltage difference of 12 V for a drift field of 80 V/cm. The voltage has been varied
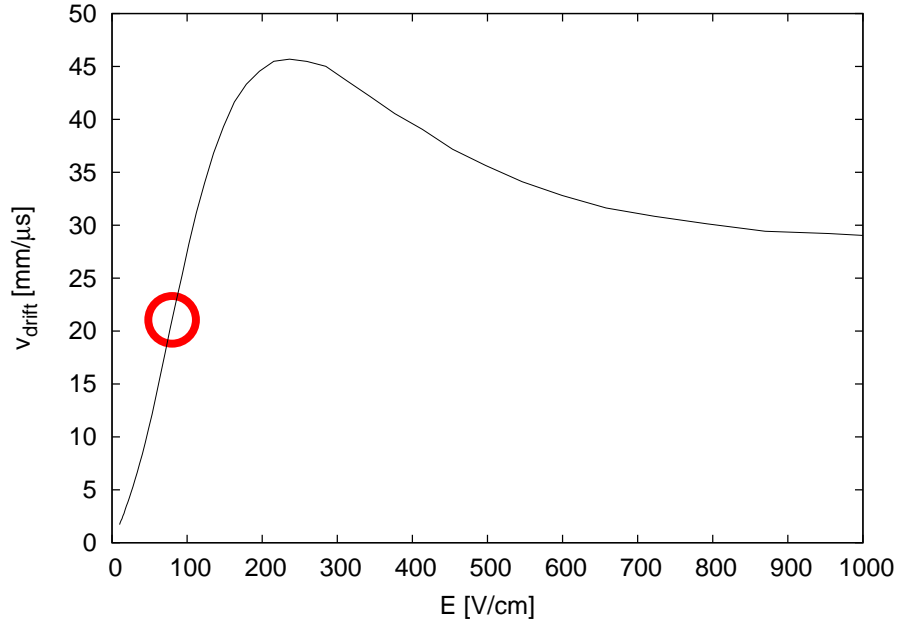
Figure 7.1: The drift velocity in dependence on the electric field for $Ar/CO_2/CH_4$ 93/2/5. The steepest slope is at 80 V/cm. (`Magboltz` [44] simulation).

in a range from 0 V to 24 V. Figure 7.2 shows the measured difference between the TPC and the hodoscope in z. The TPC position for all measurements is calibrated to the curve at 12 V, which is the nominal value, in the z range from 70 mm to 170 mm. This is why the respective curve is at $\Delta z = 0$.

One can see that all curves intersect at one point for zero drift distance. This is expected, as at $z = 0$ there is no difference between $t_{drift} = 0$ and $\frac{z}{v_{drift}}$, independently of the drift velocity. Hence the relative z position of the different curves is correct. However, the absolute is not, because the intercept point is at $\Delta z = 1$ mm and not at $\Delta z = 0$.

Without field distortions the distribution would be flat. All curves in figure 7.2 have a flat part in the central region of the TPC ($z = 70$–170 mm) and a slope near the readout. The one with 24 V offset has the lowest slope. Extrapolating the data, the curve should be flat for an offset of approximately 40 V, which corresponds to a mechanical offset of 3.5 mm. This is far beyond the mechanical displacement. As this effect is not understood, all following measurements have been performed with the nominal voltage of 12 V. An estimate of the resulting error is given in the next section.

7.1.2 Electrical Field Near the Readout Plane

Taking a closer look at Δz for a bias voltage of 12 V between the shield and the first field strip, one finds that the range up to 35 mm drift distance can be approximated
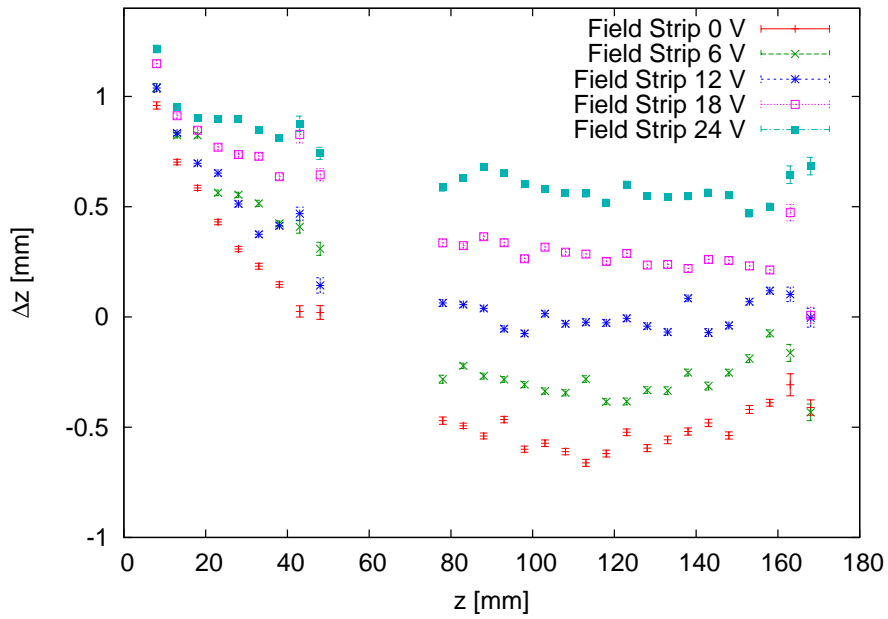
Figure 7.2: Offset between the measured z coordinates in the TPC and the hodoscope in dependence on the voltage difference between the shield and the first field strip. All curves have a flat part between 70 mm and 170 mm drift distance. This shows that the field in the middle of the chamber is homogeneous. The inhomogeneity near the readout structure depends on the voltage difference applied.
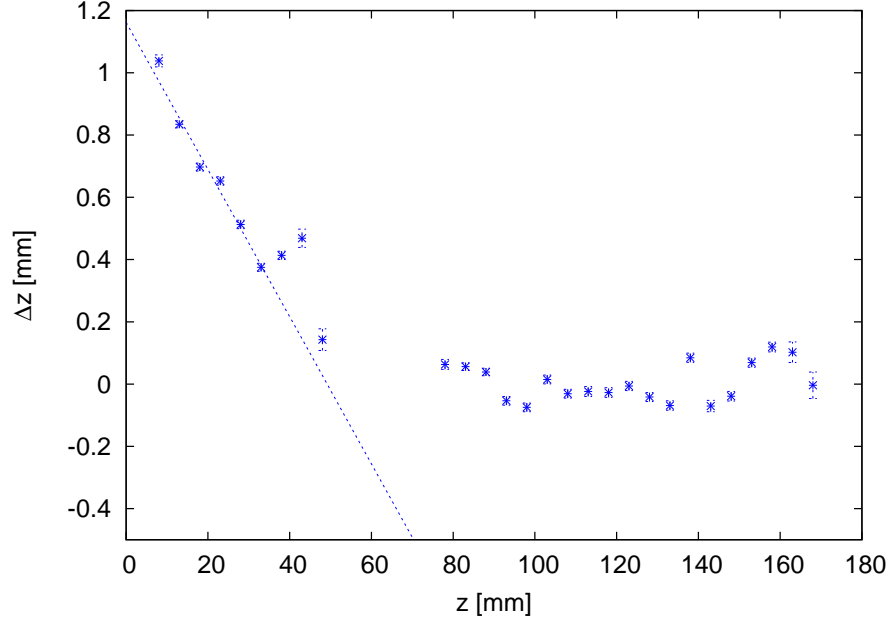
Figure 7.3: Δz for a voltage offset of 12 V between the shield and the first field strip.

by a straight line (figure 7.3). The slope of this straight line is $a = -0.0236 \pm 0.0019$. The change of the drift velocity is[1] $\Delta v_{\text{drift}} = a \cdot v_{\text{drift}} = 553 \pm 45 \frac{\mu m}{\mu s}$, which results in a field distortion of

$$\Delta E = \frac{\Delta v_{\text{drift}}}{\frac{dv_{\text{drift}}}{dE}} = 1.73 \pm 0.15 \; \frac{V}{cm}$$

This is 2.2 % of the 80 V/cm nominal field.

For drift distances larger than 70 mm, the field seems to be homogeneous. To get an estimate of the influence of 70 mm of inhomogeneous field which is off by 2.2 %, the simulated drift velocity has been approximated by a parabola near the maximum at 240 V/cm (see appendix C). From this parameterisation on finds $v_{\text{drift}}(240\frac{V}{cm}) = 45.746 \frac{mm}{\mu s}$ and $v_{\text{drift}}(234\frac{V}{cm}) = 45.716 \frac{mm}{\mu s}$. The difference of 0.03 $\frac{mm}{\mu s}$ assumed for a drift distance of 70 mm gives an offset of $\Delta z = \Delta v_{\text{drift}} \frac{z}{v_{\text{drift}}} = 46$ µm.

7.1.3 Field Homogeneity in the Central Region of the TPC

To determine the homogeneity in the central region of the TPC, the measurements with -12 V, -18 V and -24 V offset between the shield and the first field strip have been combined to improve the statistics. Only the data for $z = 70$–170 mm is used and has been recalibrated. The data for a bias of 0 V and 12 V has been omitted, because there is some influence of the inhomogeneity near the readout. Δz versus z is not completely flat for these measurements.

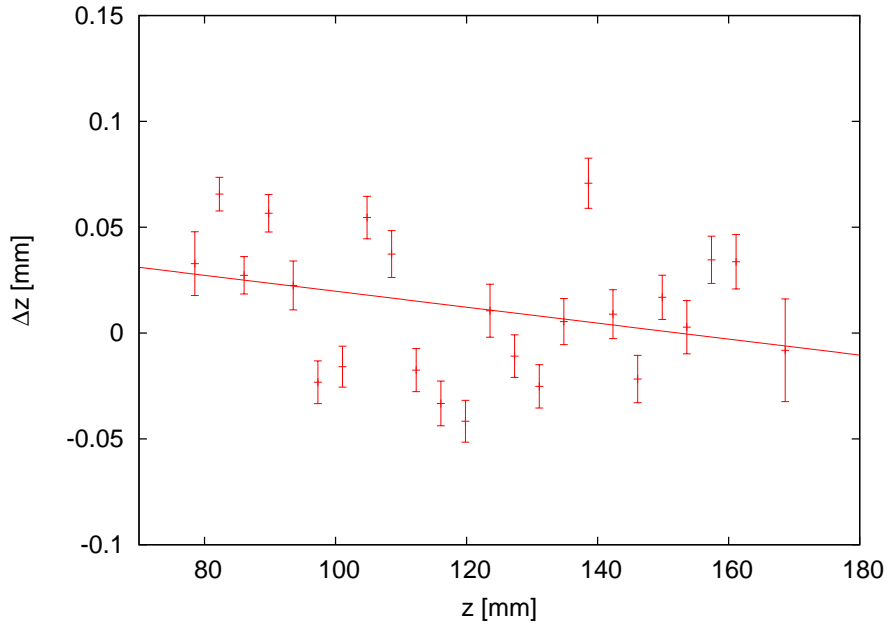[1] $\quad a = \dfrac{d\Delta z}{dz} = \dfrac{\frac{d\Delta z}{dt}}{\frac{dz}{dt}} = \dfrac{\Delta v_{\text{drift}}}{v_{\text{drift}}}$

Figure 7.4: Distance in the z direction between the TPC and the hodoscope measurement in the middle of the TPC.

Figure 7.4 shows the Δz distribution of the combined data. Fitting a straight line gives a slope of $(-3.8 \pm 2.8) \cdot 10^{-4}$. This is compatible with zero and shows that the calibration of the drift velocity is correct. But one can see that the straight line does not describe the data very well. The fluctuations are much larger than they should be according to the statistical errors. This can also be seen looking at the fit parameters. The reduced χ^2 is 10.0. The fluctuations can be interpreted as local field distortions.

As described in the previous section, the gradient of the Δz distribution is a measure for the field homogeneity. In this case the curve has been differentiated numerically, taking the gradient between two measured points. From this the field homogeneity has been calculated. It is shown in figure 7.5. Again, the fluctuations are larger than the statistical errors, but no systematic dependency on the drift distance is visible. The variance of the distribution is $8 \cdot 10^{-3}$. The resolution of this measurement does not suffice to determine the local field inhomogeneities, but one can give an upper limit of $8 \cdot 10^{-3}$. To verify the design goal of 10^{-4}, the measurement has to be improved. The correction of the jitter between the trigger and the TPC clock is needed to obtain a good time resolution, which is essential for this analysis. Unfortunately, the time marker for the jitter correction is not available for this measurement. Applying this correction will bring further improvements of the results. Increasing the statistics also helps to reduce the errors.
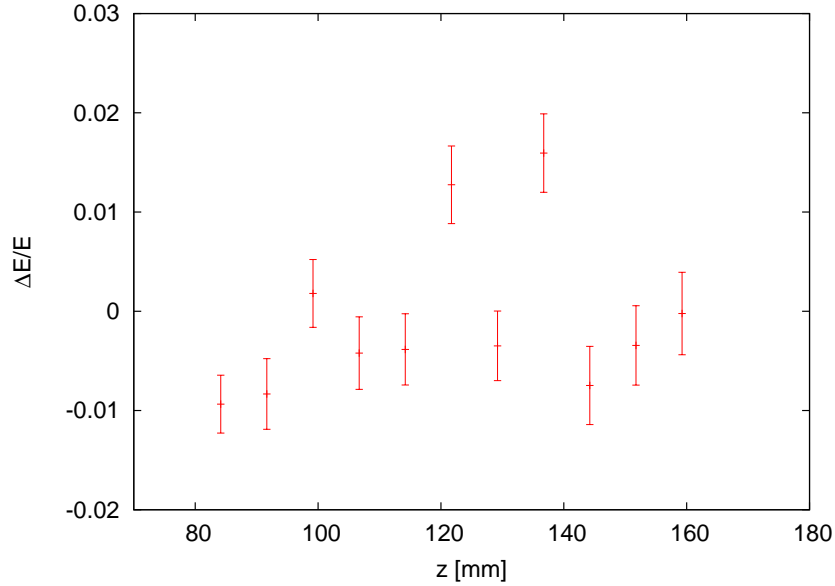
Figure 7.5: Deviations from the nominal field in the central TPC region.

7.2 Measurements at the Maximum Drift Velocity

Inhomogeneities in the electric field do not only change the field in z direction, but also introduce a transverse component of the field. Especially for measurements without magnetic field, where the drift lines follow the electric field, this transverse component causes distortions in the xy plane. The hodoscope provides reference measurements for the x and the z coordinates and allows to create distortion maps, which can be used to correct the TPC data and achieve a better resolution. The following measurements have been performed at an electric field of 240 V/cm, which corresponds to the maximum drift velocity.

7.2.1 Distortion Maps

To create distortion maps, the active volume of the chamber has been divided into 3D bins, 16 bins in x (one bin for two pads) and 15 bins in y (one for each row). In the z direction the positions have been chosen dynamically according to the z positions which were used during the test beam measurements. For each of these 3D bins, one histogram for Δx and one for Δz is filled. The mean values of these distributions are then filled into a 3D array. If the number of entries in a histogram is below 10, the distortion information for this grid point is flagged as invalid.

Distortions in x

Figure 7.6 shows the measured distortions Δx versus x and y at three different z positions: Near the readout, in the middle of the chamber and near the cathode.

There are two components in the distributions: A statistical one which causes a peak at the high-x edge of the distribution and one component which is growing with increasing drift distance. The latter is an indication of deviations caused by drift field distortions.

Distortions in z

The deviations in the z direction, shown in figure 7.7, have a characteristic shape: The maximum is at $y = -60$, the lowest part is around $y = 0$ at the low-x edge of the distribution. Unlike Δx, the Δz distribution does not change with the drift distance. This means the distortions are caused in the drift space near the readout or in the GEM structure. A strong indication for the latter is the fact that the deviations change with the GEM setting (figure 7.8).

7.2.2 Corrections

For each reconstructed point the correction is calculated using the next four grid points at the same y coordinate. The four corrections are weighted proportionally to their inverse distance to the measured point. As the reconstruction algorithm is row based, only one row is used for the distortion corrections and there is no interpolation in the y direction. Figures 7.9 and 7.10 show the distortions without correction and the remaining distortions after the correction, in the x and the z direction, respectively. The remaining mean distortion in x is 50 ± 8 µm, in z it is 81 ± 8 µm. This is below the respective single point resolution (best measured values: $s_x = 150$ µm, $s_z = 206$ µm, see section 8.2).

After applying the distortion corrections, the deviation distributions are significantly flattened, in the x as well as in the z direction.

7.2.3 Summary

Generating 3D distortion maps by measuring deviations between the TPC and the hodoscope allows systematic studies of the deviations' origin. The distortions of the drift field mainly have an impact on the x coordinate, because they introduce a transverse component of the electric field. This can be seen by the drift distance dependency of the x distortions. In the z direction, the deviations are not dependent on the drift distance. They originate from inhomogeneities in the GEM structure and vary with the GEM settings. The deviations in both directions are well reproducible and thus can be corrected for. As shown in figure 7.11 and 7.12 this correction really improves the spatial resolution. In the whole drift range, the spatial resolution s_x of the corrected data is about 11 µm better than for the non-corrected data. In the z direction the improvement depends on the drift distance. It reaches from more than 60 µm near the readout to less than 20 µm at $z \approx 220$ mm.
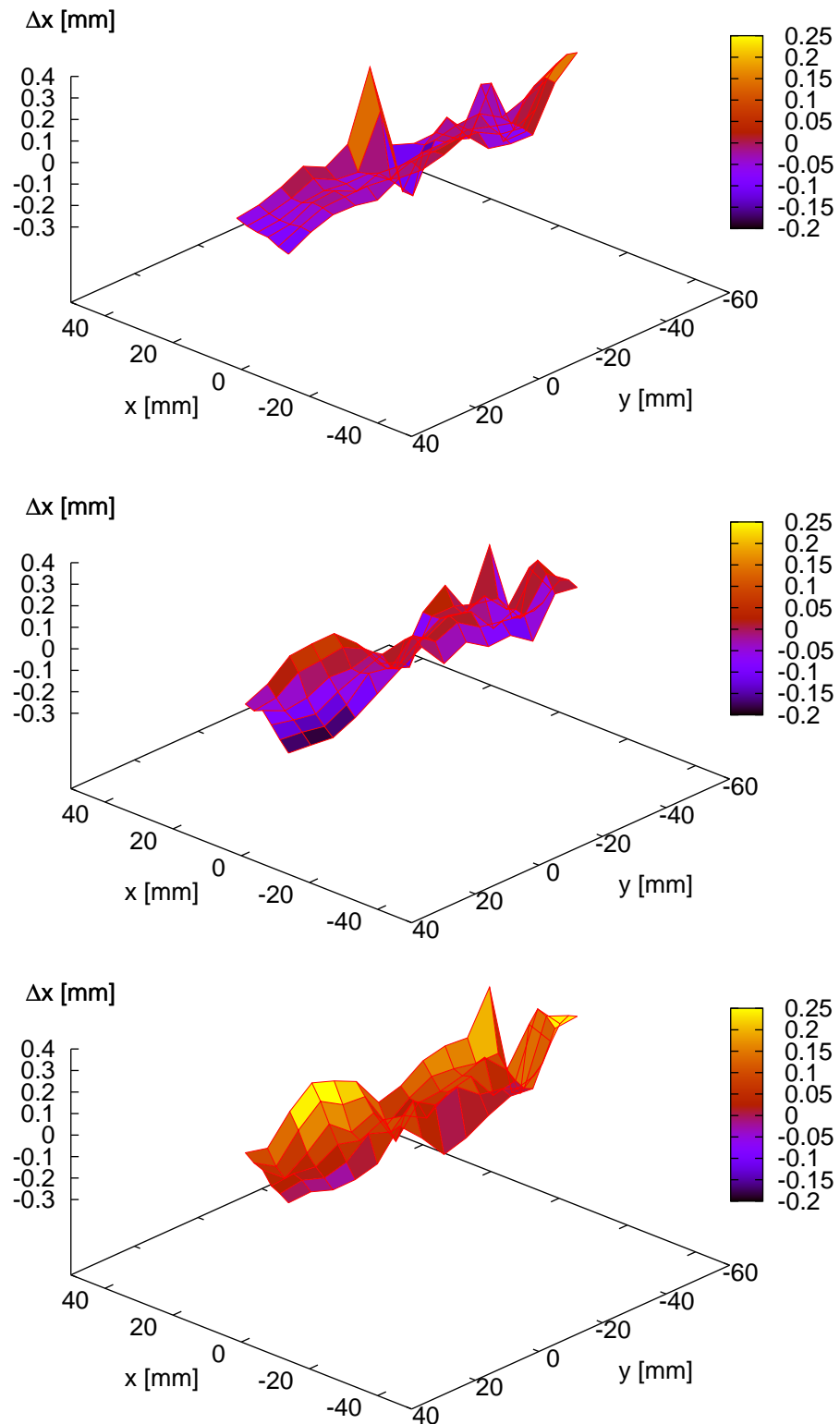
Figure 7.6: Distortions in x at 25 mm (top), 145 mm and 215 mm (bottom) drift distance.
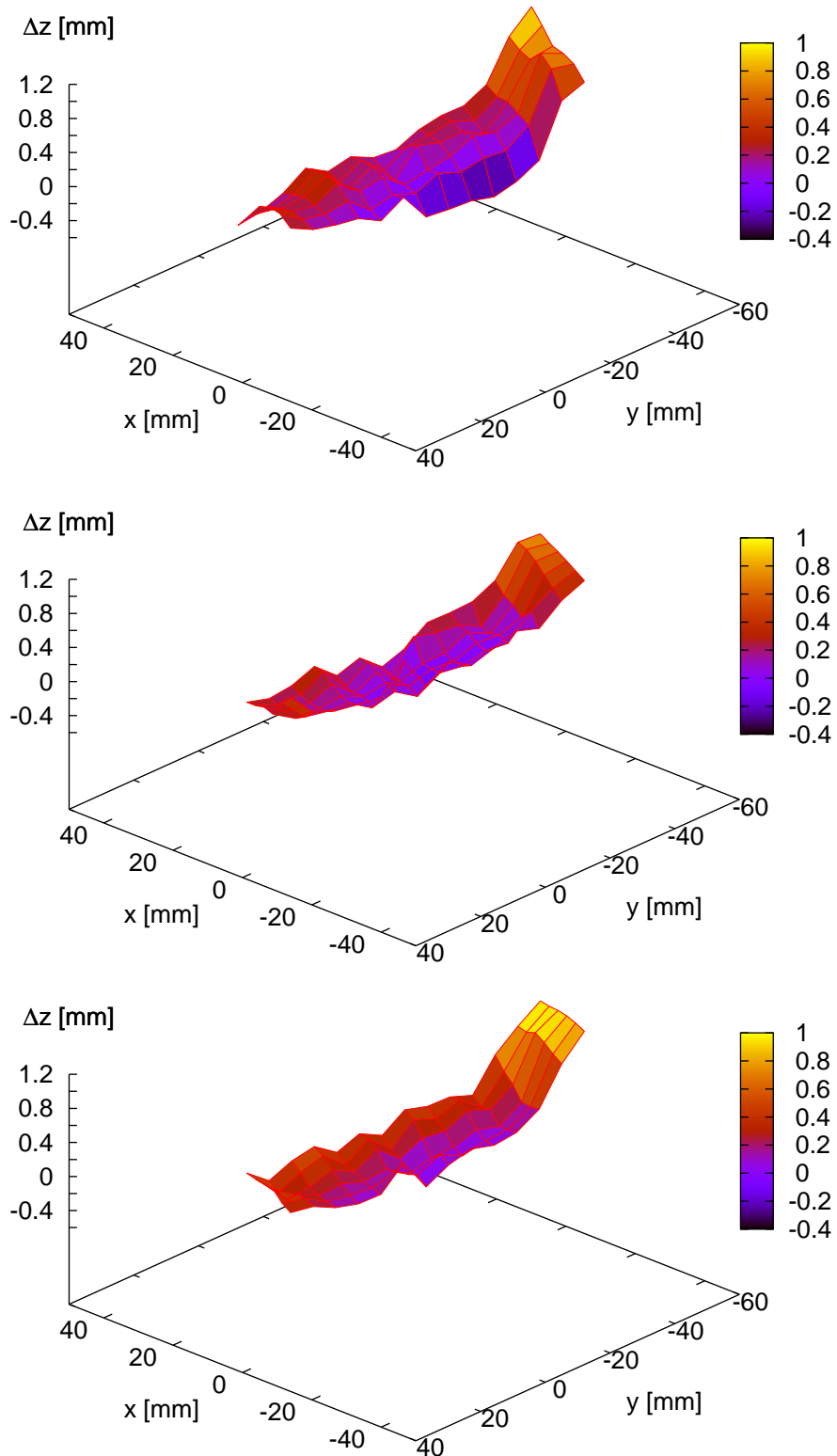
Figure 7.7: Distortions in z at 25 mm (top), 145 mm and 215 mm (bottom) drift distance.

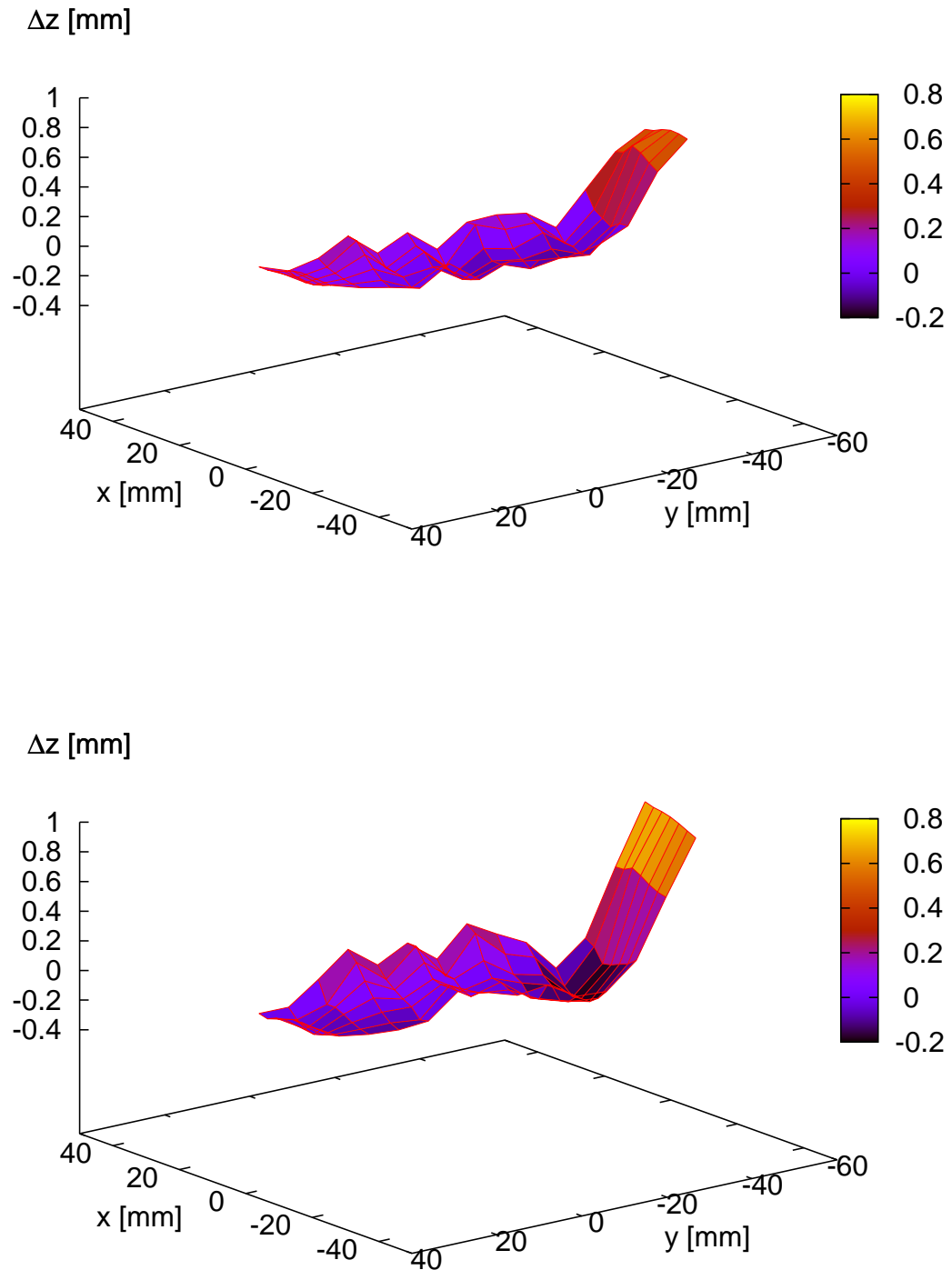Figure 7.8: Δz against xy in dependence on the GEM setting: The setting optimised to reduce ion backdrift (bottom) causes stronger deviations than the non-optimised one (top).
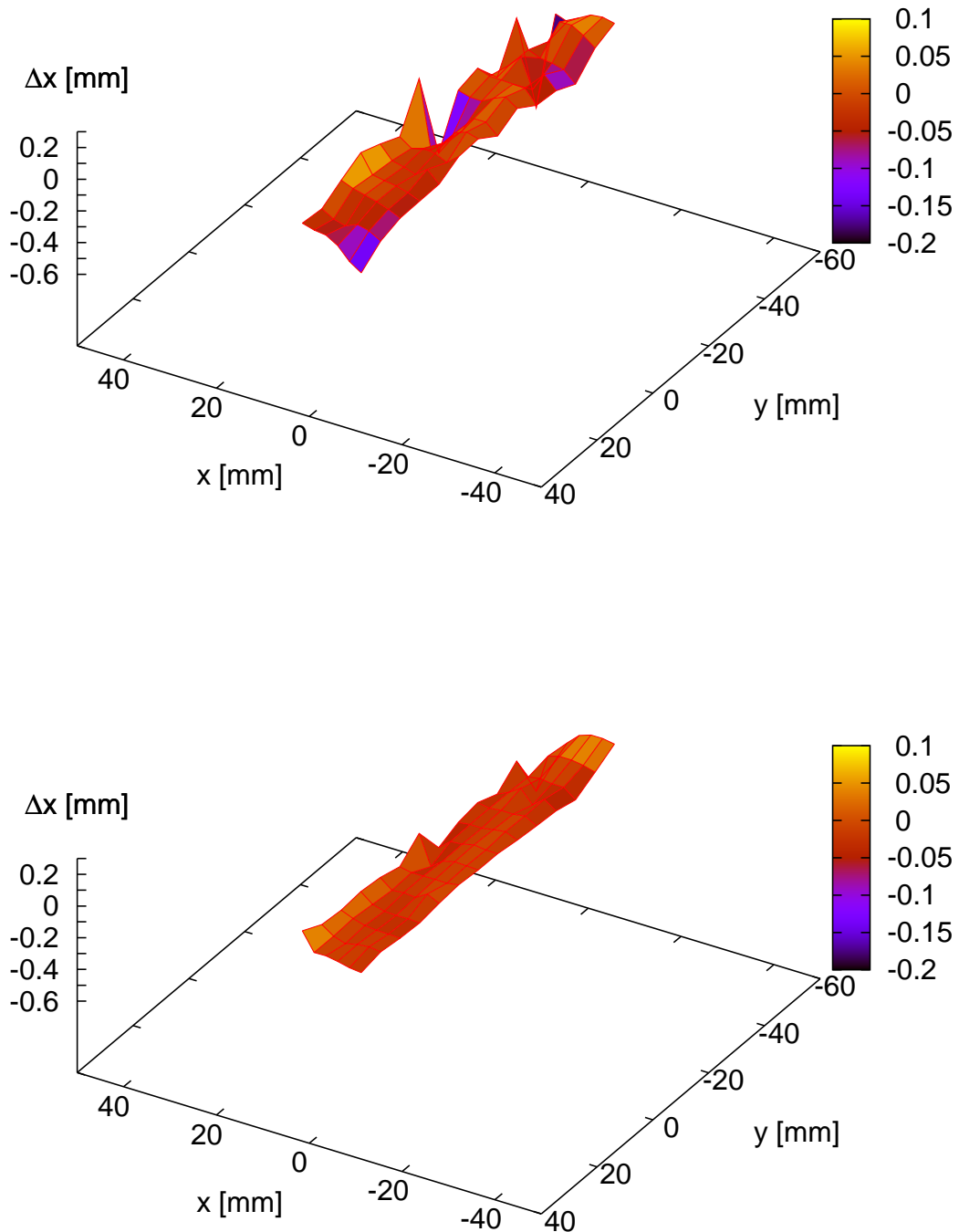
Figure 7.9: Δx before (top) and after (bottom) the distortion corrections.
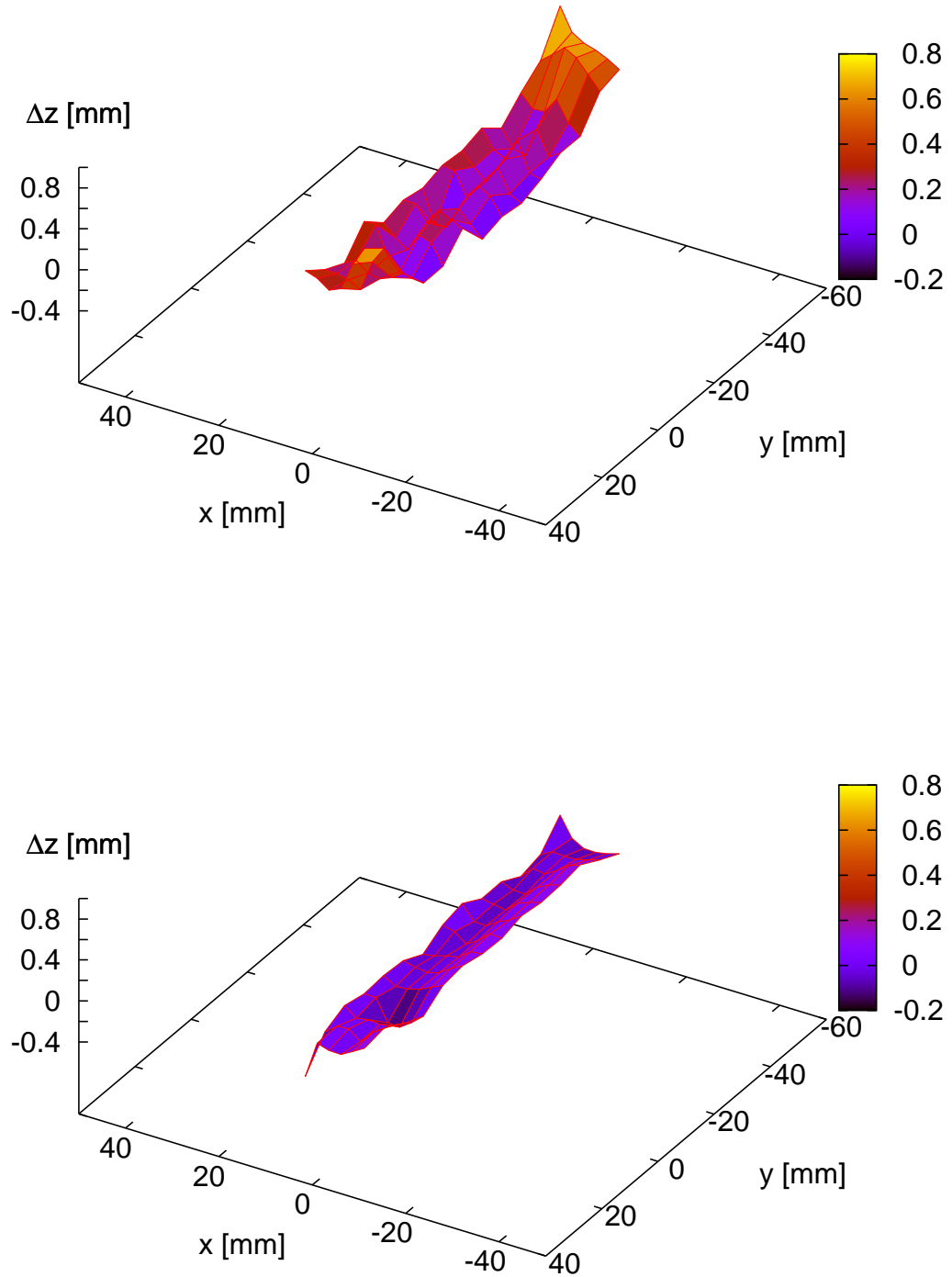
Figure 7.10: Δz before (top) and after (bottom) the distortion corrections.
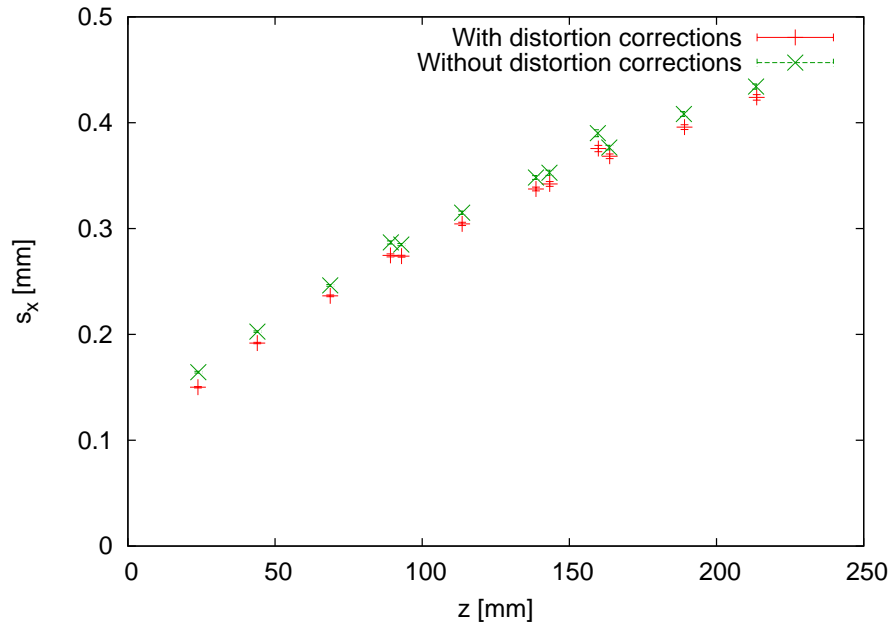
Figure 7.11: Spatial resolution in x with and without distortion corrections (in Ar/CO$_2$/CH$_4$ 93/2/5).
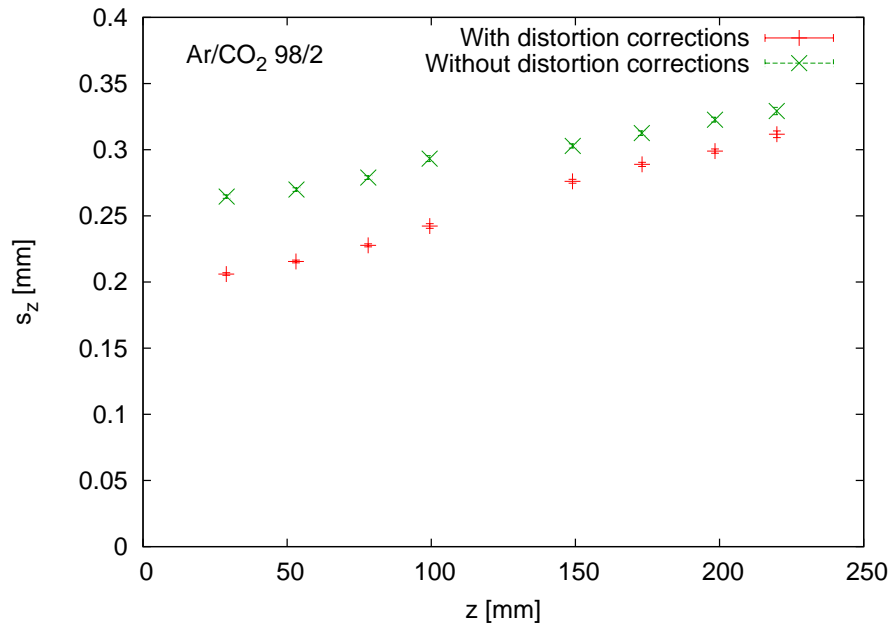
Figure 7.12: Spatial resolution in z with and without distortion corrections (in Ar/CO$_2$ 98/2).

8 Spatial Resolution

8.1 Definitions

Generally, the spatial resolution is defined as the mean distance of the reconstructed points to the real particle track. For the measurements with the hodoscope, its data is used as the "real" track. For the measurements performed at 4T magnetic field, no reference track is available, because the hodoscope does not fit into the magnet's bore. Here a different definition has to be used, which is based only on the TPC measurement. Both definitions will be introduced in the following sections.

As the reconstruction algorithm always sets the y position to the centre of the pad row, the error of the reconstructed points in y direction is set to zero. Below, only the resolutions in the x and the z direction are considered.

8.1.1 Definition 1: Spatial Resolution Measured With the Hodoscope

In the hodoscope, x and z are parameterised as a function of y ($x = a \cdot y + b$, $z = c \cdot y + d$). From these parameterisations, x and z in the hodoscope are determined using the y value of the measured TPC point. The residuals Δx and Δz are the distances between the TPC and the hodoscope measurement.

$$
\begin{aligned}
\Delta x &= x_{\text{tpc}} - x_{\text{hod}}(y_{\text{tpc}}) \\
&= x_{\text{tpc}} - a \cdot y_{\text{tpc}} - b
\end{aligned}
$$

$$
\begin{aligned}
\Delta z &= z_{\text{tpc}} - z_{\text{hod}}(y_{\text{tpc}}) \\
&= z_{\text{tpc}} - c \cdot y_{\text{tpc}} - d
\end{aligned}
$$

The widths of the Δx and Δz distributions correspond to the single point resolution in x and z, respectively. The distributions show long, non-Gaussian tails (see fig. 8.1). Hence the width of a Gaussian fitted to the centre of the distribution would yield too low values. Instead of the Gaussian sigma, the RMS of the distribution is used as spatial resolution s:

$$
\boxed{
\begin{aligned}
s_x &= RMS(\Delta x) \\
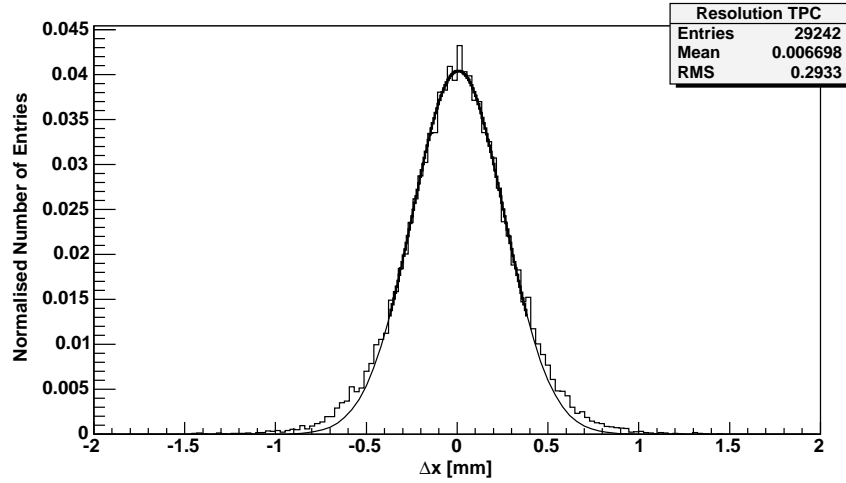s_z &= RMS(\Delta z)
\end{aligned}
}
$$

Figure 8.1: Distribution of the residuals Δx measured between the TPC and the hodoscope (histogram normalised to one).

To cut away outliers, a 5·RMS cut is applied recursively to the distribution. To give an error estimation, the statistical error of the RMS, i.e. its standard deviation is used.

In the example in figure 8.1, the width of the residual distribution is 293.3 ± 1.5 µm. The hodoscope itself has a limited resolution of 44 µm. Subtracting this value quadratically from the width of the residual distribution, the resolution of the TPC measured with the hodoscope yields $s_x = 290.0 \pm 1.5$ µm in this example.

8.1.2 Definition 2: Spatial Resolution Without Reference Track

For measurements without hodoscope, the individual points have to be compared to the reconstructed track. In this case, the particular point does influence the result of the track fit. The calculated RMS is a too optimistic value. To achieve an unbiased result, the point is excluded from the track and the track is refitted. However, if there is only a small number of reconstructed points, neglecting the point in the track reconstruction gives a too pessimistic estimate. This is the case for the prototype used in the present work. Therefore, for the resolution s the geometric mean of the two RMS values, calculated including and excluding the analysed point, is used.

$$s = \sqrt{RMS_{\text{in}} \cdot RMS_{\text{out}}}$$

This is expected to be a good estimate of the true resolution [69]. In this example, the resulting resolution is $s_x = \sqrt{249.2 \cdot 333.1}$ µm $= 288.1 \pm 0.8$ µm (figure 8.2). Comparing to the measurement with the hodoscope, which gives a resolution of 290.0 ± 1.5 µm, both results are in good agreement.

Without a magnetic field, this method to determine the resolution works well. But the widths of the charge clouds at 4 T are smaller than for the example shown.
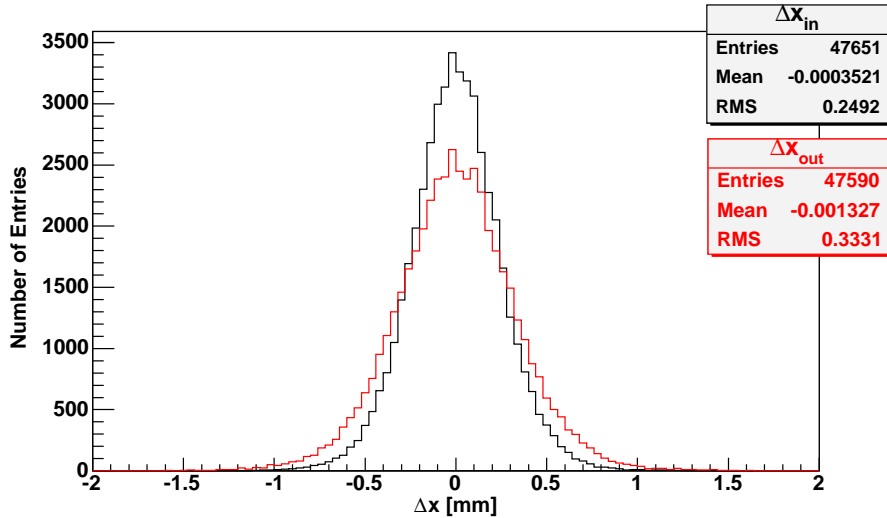
Figure 8.2: Distribution of the residuals with the specific point included (Δx_{in}) and excluded (Δx_{out}) in the track fit.

In this case the estimated resolution might be too optimistic, because the track is biased towards the reconstructed hits. This holds especially for the centre of gravity method, which pulls the points to the centre of the pad with the largest charge deposition. Since there is no hodoscope data avaliable for measurements in magnetic field, a detailed TPC simulation [70][71] is used to verify the method in this specific case and get an impression about the size of the bias. It simulates the generation of primary ionisation including clustering and delta electrons in the TPC. The diffusion of the produced electrons drifting to the readout plane is calculated and the amplification in the GEM stack is modelled, using in-depth studies of the charge transfer within a GEM structure [52]. Mapping the signal onto pads, taking into account the shaping of the electronics, generates a very realistic ADC response. The simulated data is subsequently reconstructed with the same software as the measured data from the prototype.

The reconstructed points are now compared with the reconstructed track and the Monte Carlo truth. One finds that the resolution determined by reconstruction only is about 7 µm too small (figure 8.3). Thus the measured resolution with respect to the reconstruction is a little bit underestimated due to the bias introduced by this method.

8.2 Measurements With the Hodoscope

For the measurements with the hodoscope there is always a reference track available. Hence the unbiased definition for the resolution s as described in 8.1.1 is used. All measurements were performed with a 1.5° angle of the particle track in the xy plane with respect to the y axis. The angle in the zy plane is always 0°.
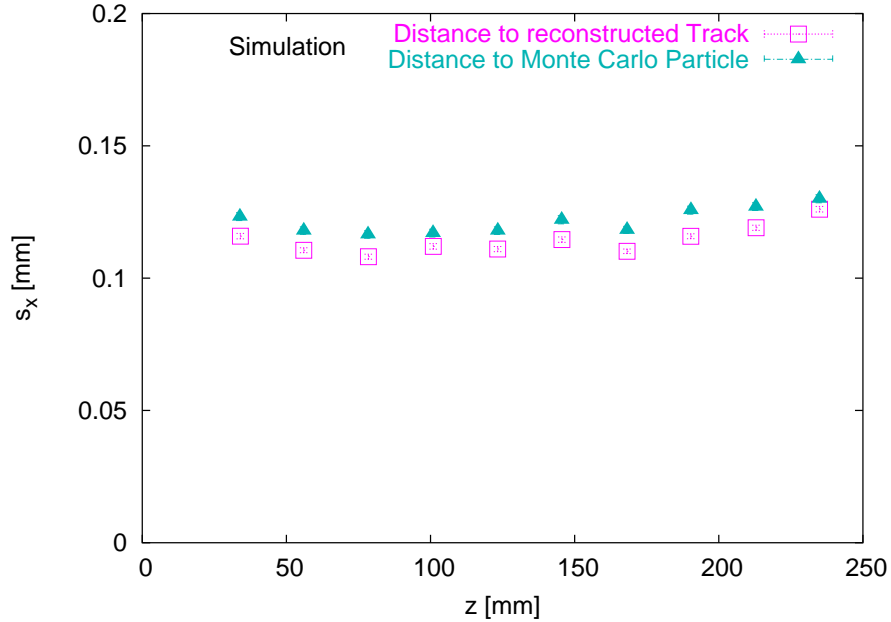
Figure 8.3: Resolution s_x of simulated data determined by reconstruction only and comparing to the Monte Carlo particle at 4 T magnetic field [70].

8.2.1 Spatial Resolution in x

Figure 8.4 shows the square of the resolution s_x against the drift distance. A linear rise of s_x^2 is observed. This effect is caused by the broadening of the charge cloud due to tranverse diffusion, which is not suppressed, as the measurement was performed without magnetic field. The best resolution is measured at a drift distance of 24 mm. It is found to be $s_x = 150 \pm 1$ µm. The ordinate intercept should be a measure of the intrinsic resolution without diffusion effects. Unfortunately, the measured s_x^2 values are large compared to the intercept and the slope of the straight line is relatively steep. As a result, the intercept is not a useful measure, as we will see in the next section.

Resolution for Different Gases

The test beam measurements were performed using several gas mixtures with different diffusion coefficients. As we have seen above, the spatial resolution in x without magnetic field is dominated by the diffusion. This should result in different resolutions for the different gases.

Most of the measurements were done with the mixture proposed in the technical design report (TDR) of the TESLA project [19], which is Argon mixed with 2% of carbon dioxide and 5% of methane ($Ar/CO_2/CH_4$ 93/2/5), referred to as "TDR gas" below. If not denoted otherwise, all measurements presented in this chapter were performed with the TDR gas mixture. The other gases used were Ar/CH_4 95/5 and Ar/CO_2 98/2. Especially the latter is an interesting mixture, as it does not contain
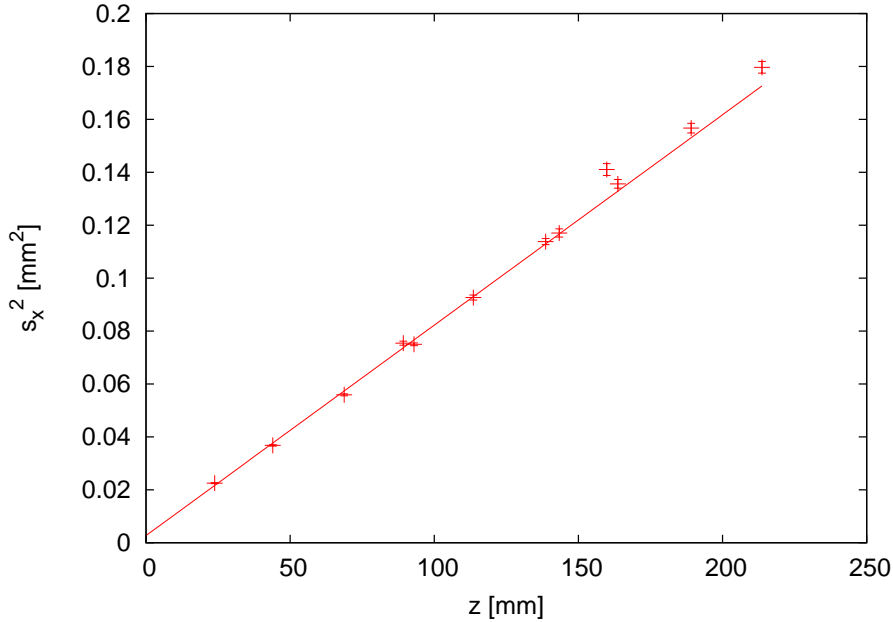
Figure 8.4: Square of the resolution s_x versus z.

hydrogen, which might cause problems due to a possibly high neutron background at the ILC.

Figure 8.5 shows the spatial resolution in the x direction achieved with the three gases. Again, the square of the resolution is plotted against the drift distance. As expected, the curve for Ar/CH_4 95/5, the gas with the largest transverse diffusion, has the steepest slope. But here the straight line does not fit the data. Due to the large diffusion in this gas, the charge is distributed across many pads, reducing the signal on each individual pad. The limited resolution of the ADC (8 bits) and the high thresholds cut away the tails of the distribution. This degrades the spatial resolution, especially for large drift distances. For Ar/CO_2 98/2 the measured points are in good agreement with a straight line, but the ordinate intercept is negative. This shows that the measurements reproduce the expected behaviour, but the determination of the intrinsic detector resolution from the ordinate intercept does not work. The best measured resolutions without a magnetic field (at $z \approx 25$ mm) are 150±1 µm for the TDR gas mixture, 180±1 µm for Ar/CO_2 98/2 and 242±1 µm for Ar/CH_4 95/5.

8.2.2 Spatial Resolution in z

Besides diffusion, the resolution in the drift direction additionally depends on the ADC's readout frequency and the pulse shaping of the preamplifiers. In this setup, the fast Preshape32 preamplifiers are operated together with 12.5 MHz ADCs. As a result, the pulses are only 2 or 3 time samples long (figure 8.6). In this case, the centre of gravity reconstruction method biases the mean value towards the centre
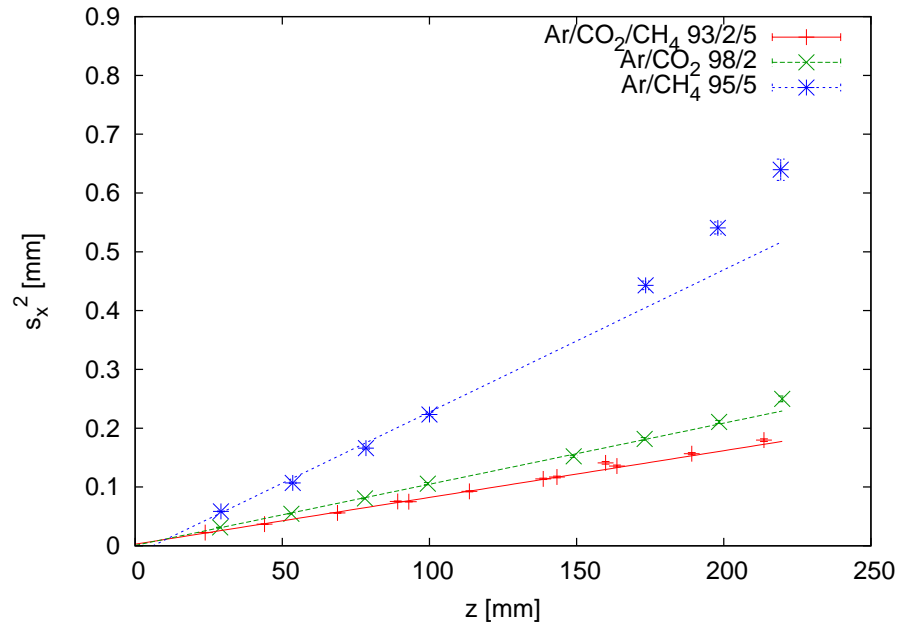
Figure 8.5: Square of the spatial resolution in x for different gases without magnetic field.
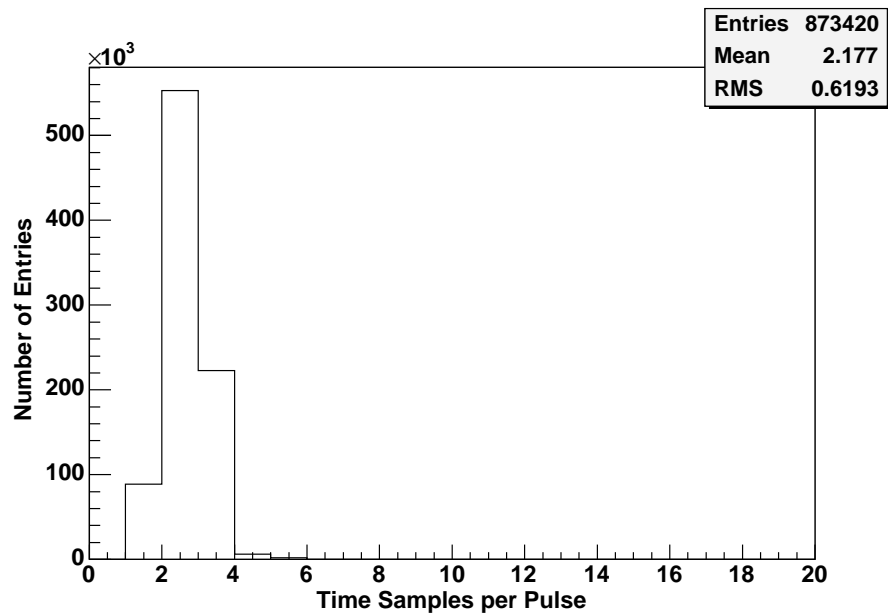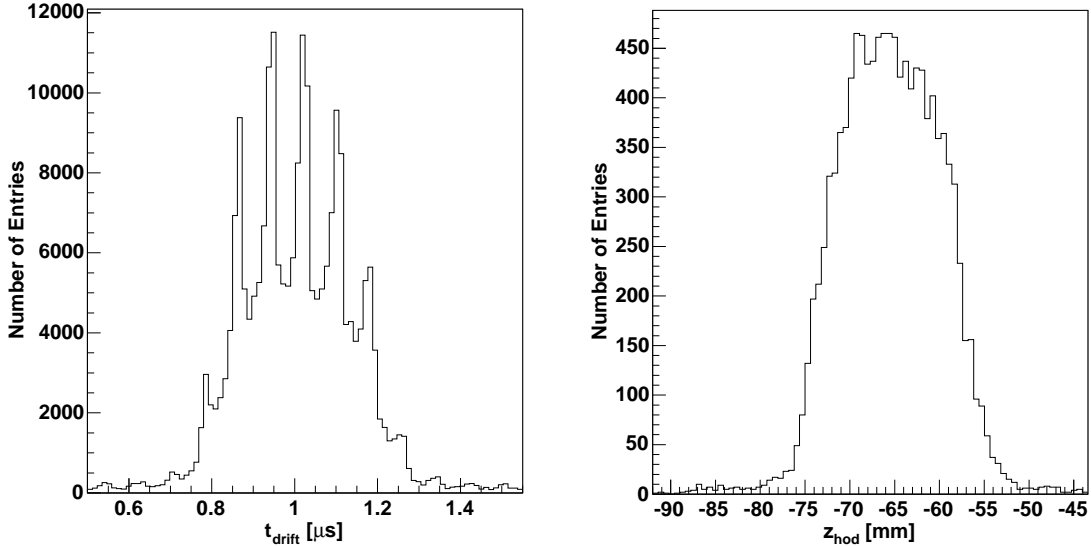

Figure 8.6: The mean length of a pulse is only 2.2 time samples.

(a) Beam profile in z measured with the TPC.

(b) Beam profile in z measured with the hodoscope.

Figure 8.7: The beam profile in z, measured with the TPC and the hodoscope.

of the time bin with the maximal charge. This effect can be seen when looking at the distribution of the reconstructed times in the TPC (figure 8.7(a)). In this measurement the chamber has not been moved within the test beam. Therefore, the measured z coordinates should show the beam profile. One observes a finger structure modulated onto the profile of the beam. The fingers have an interval of 80 ns, which is the length of one time sample.

To assure that the structure is not part of the actual beam profile, the same measurement performed with the hodoscope is shown in figure 8.7(b). One obtains a smooth profile and no fingers are observed.

The angle of the tracks in the zy plane is 0° in the test beam measurements and all pulses are at the same z coordinate. This causes the complete track to be biased, all points are shifted towards the centre of the same time bin. Therefore only the resolution determined using the hodoscope will give reliable results for the z direction. As shown in section 6.5, this does not work without correcting the jitter between the trigger and the TPC clock, which requires a time marker to be recorded together with the signal. However, the time marker is not available for the measurements with TDR gas. Therefore the following results are shown for the Ar/CO_2 98/2 mixture.

Figure 8.8 shows the squared z resolution against the drift distance. For small drift distances, one observes a deviation from the expected linear correlation. Here the resolution limit of this prototype setup is reached, mainly because of the short-
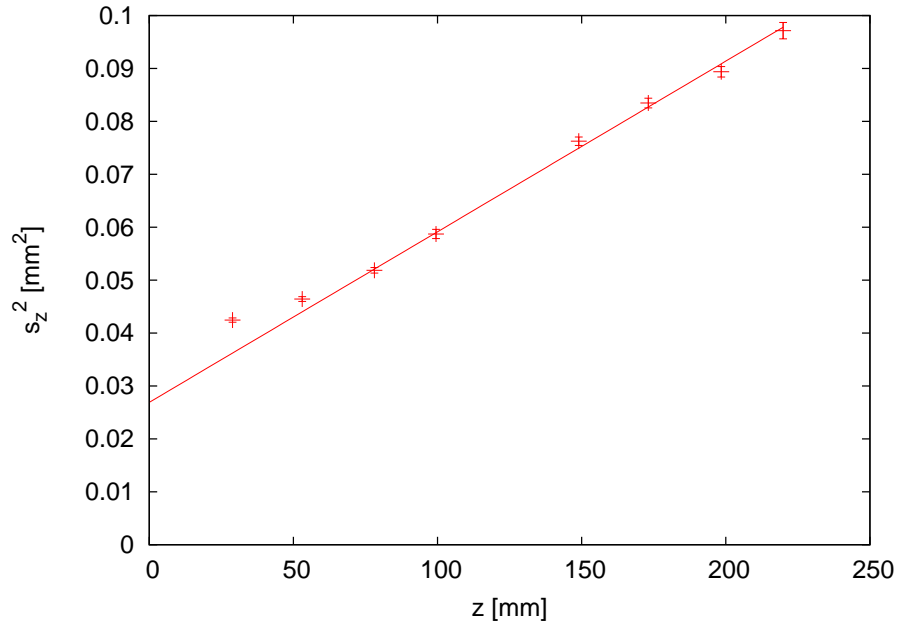
Figure 8.8: Resolution in the z direction in Ar/CO_2 98/2.

comings of the electronics used.

The best measured value at $z = 29$ mm is $s_z = 206 \pm 1$ µm. The slope of the straight line is smaller than for the x resolution shown in figure 8.5. This is expected, as the longitudinal diffusion is lower than the transverse diffusion. However, the longitudinal diffusion will not be reduced by a magnetic field along the drift direction. Therefore this measurement should give a good estimate for a large TPC. Extrapolating the straight line to 2.5 m drift distance yields a value of $s_z(2.5$ m$) = 913 \pm 12$ µm. This matches the requirements stated in the TESLA TDR [19]. Taking into account the shortcomings of the currently used ADCs and the simple centre of gravity reconstruction method, these results can even be improved with the final electronics and software.

8.2.3 Resolution for Different GEM Settings

The GEM settings optimised to suppress the ion backdrift (IB) have a very low field in the second transfer gap (see section 3.4.3 and reference [52]). Due to this low field the extraction from the second GEM is diminished and this could result in a reduced spatial resolution compared to the so-called standard setting, which has transfer fields of 2500 V/cm and the same voltage across all GEMs. Table 8.1 presents the GEM voltages and field settings. The setting optimised for minimal ion backdrift provides the same total gain as the standard setting, while the ion backdrift ι is reduced from 0.075 to 0.005. The optimised setting turned out to be quite instable in operation due to the high voltage at the third GEM and the very high induction field, so a third setting with more moderate settings was used for

Setting	U_{GEM1} [V]	E_{trans1} [V/cm]	U_{GEM2} [V]	E_{trans2} [V/cm]	U_{GEM3} [V]	E_{ind} [V/cm]
Standard	310	2500	310	2500	310	5000
IB optimised	313	6000	314	60	350	8000
IB optimised (moderate)	328	4000	328	100	340	6000

Table 8.1: Settings of the readout structure used for the test beam measurements.
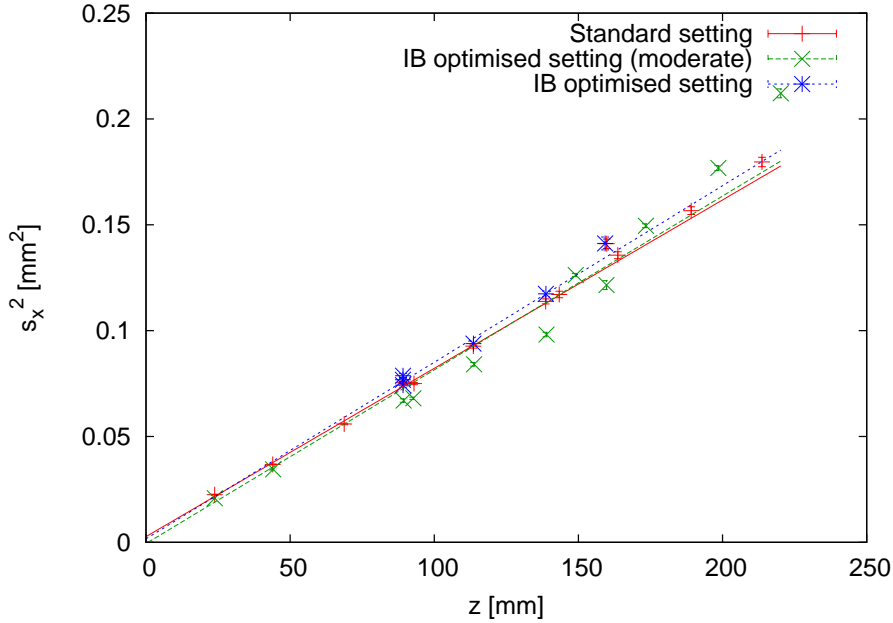
Figure 8.9: Square of the resolution s_x versus z in dependence on the GEM settings, measured in $Ar/CO_2/CH_4$ 93/2/5.

most of the measurements. According to the parametrisation in [52] this setting still provides a good ion backdrift suppression ($\iota = 0.012$) and works very reliably.

The spatial resolution in the x direction is shown in figure 8.9 for the three GEM settings. They all provide the same spatial resolution. This shows that the gas amplification in the first two GEMs provides enough electrons and the low extraction from the second GEM does not have a negative influence on the spatial resolution.

Spatial Resolution in z

The spatial resolution in the z direction depends on the GEM setting (figure 8.10). The values from the ion backdrift optimised setting are about 10 µm above those from the standard setting. This is caused by the smaller length of the peaks in the former one. Figure 8.11 shows the mean number of time samples per pulse. One can see that the pulse length is shorter for the ion backdrift optimised measurement, which is due to the fact that the fields between the GEMs cause smaller diffusion for
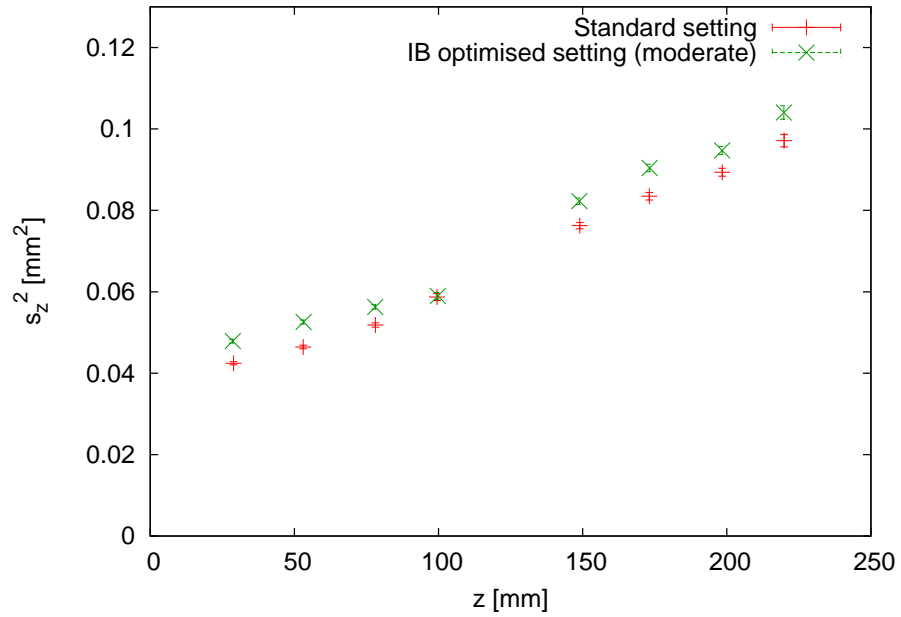
Figure 8.10: Resolution in the z direction in Ar/CO_2 98/2 gas for ion backdrift optimised and standard GEM settings.
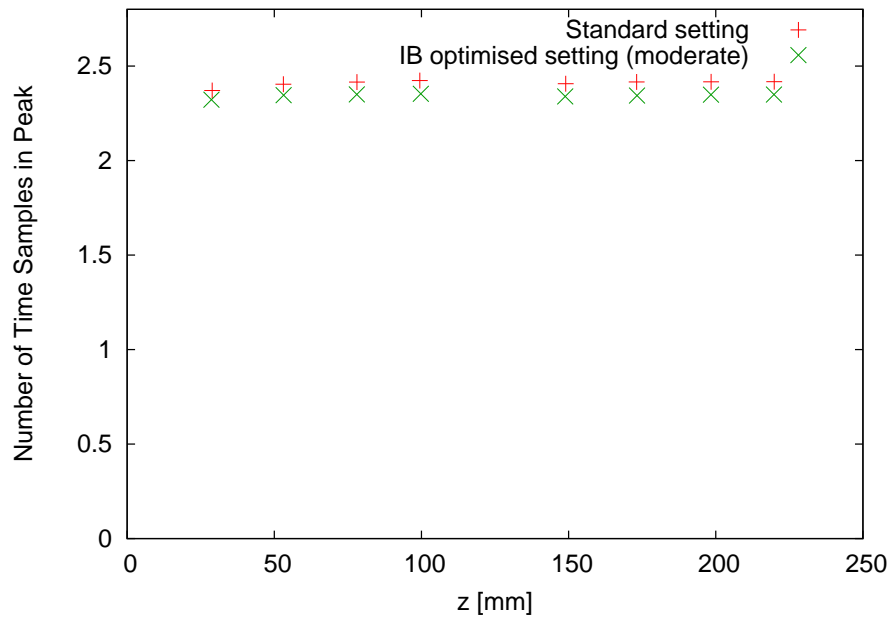

Figure 8.11: Lengths of the peaks measured with ion backdrift optimised and standard GEM settings in Ar/CO_2 98/2 .
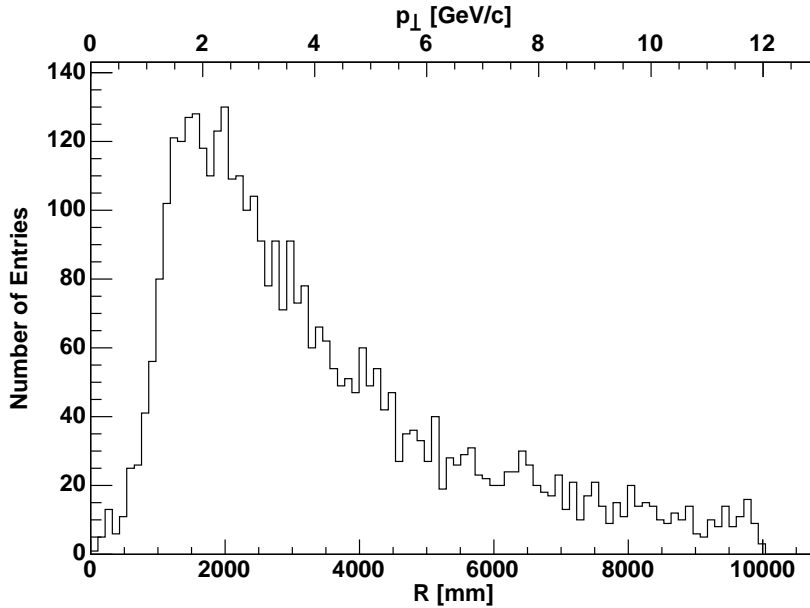
Figure 8.12: Radii and transverse momenta of the measured tracks in a 4 T magnetic field.

this setting. The bias of the centre-of-gravity-based reconstruction method is larger in this case, which affects the resolution.

Again, the ion backdrift optimised setting performs as well as the standard setting. The slightly degraded resolution in the time direction can be explained by the shortcomings of the reconstruction.

8.3 Measurements in a 4 T Magnetic Field

For the measurements in the 4 T magnet no reference track from the hodoscope is available. This means the resolution definition given in section 8.1.2 has to be used. To confirm that the track reconstruction works reliably, the radii of the measured tracks are shown in figure 8.12. One can see that the distribution is cut off for radii below ≈ 1000 mm. This corresponds very well to the estimated minimal radius of 900 mm due to the geometrical acceptance of the trigger system [62]. As the helix radius is proportional to the particle's transverse momentum $p_\perp$, this plot also represents a $p_\perp$ spectrum. All measured transverse momenta are above ≈ 1 GeV.

The spatial resolution s_x for both the optimised and the standard GEM settings is depicted in figure 8.13. As it is expected, the dependency on the drift distance due to transverse diffusion is much smaller than without magnetic field. A small rise for $z > 150$ mm can be seen for the standard setting, but the diffusion does not significantly limit the resolution. Like in the measurements at 0 T, the two settings do not differ very much. Both curves show a degradation for short drift distances. It is caused by the width of the electron cloud becoming small. As the current
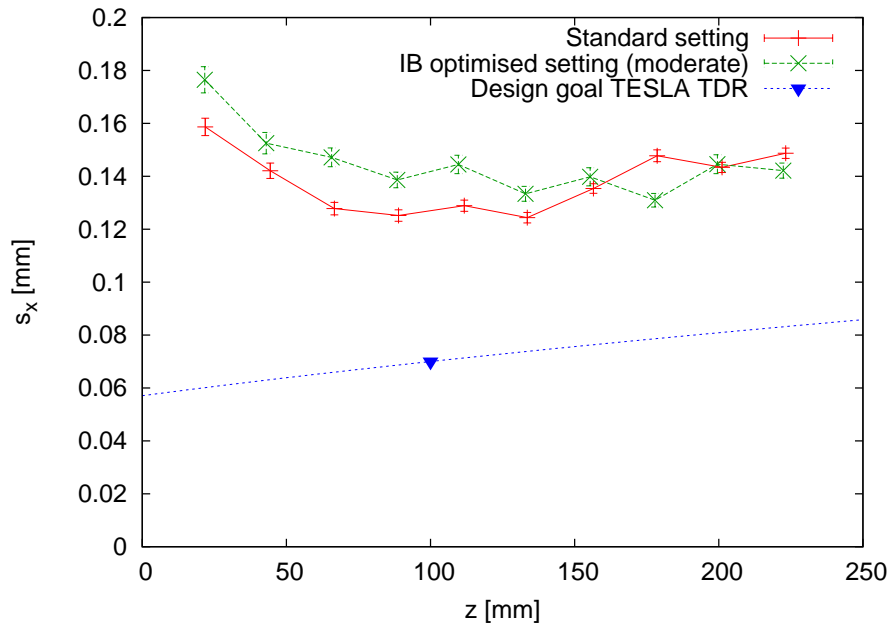
Figure 8.13: Resolution s_x versus z at 4 T magnetic field. The design goal is extrapolated from the values stated in the TESLA TDR [23]: $s_x = 0.07$ mm for $z = 100$ mm; $s_x = 0.19$ mm for $z = 2000$ mm.

reconstruction method does not use a pad response function, the bias of the TPC points is getting larger with decreasing width of the electron cloud (see appendix D).

This also explains why the standard setting gives a slightly better resolution in this area: The optimised setting has less diffusion in the transfer gaps and thus the width of the charge cloud is even smaller. Once again, the ion backdrift suppressing setting is disadvantaged by the reconstruction. However, the spatial resolution is not degraded significantly.

The best measured resolution is 124 ± 2 µm for the standard setting. This is almost a factor of two above the goal of 70 µm at 100 mm drift distance, as stated in the TESLA TDR [23]. But the data is not corrected for field distortions, as there is no reference track for the measurements in magnetic field. Applying the corrections determined at 0 T could not improve the resolution. This is not surprising, as the field inhomogeneity near the readout structure described in section 7.1.2 introduces $E \times B$ effects and the electrons are deflected in a different direction. Hence a first step to improve the resolution is to enhance the field homogeneity by correcting the alignment of field cage and gas amplification structure. The simultaneous operation of a TPC and a hodoscope in a magnetic field is planned for a large TPC prototype which is currently designed at DESY Hamburg as part of the EUDET detector R&D project [72].

9 Conclusion

A TPC is proposed as the main tracking device in three of the four concept studies for an ILC detector. To achieve the required spatial resolution, micro pattern gas detectors like GEMs and Micromegas are studied as gas amplification structures.

This thesis presents measurements with a TPC prototype, equipped with a triple GEM readout structure. It was operated in a silicon strip hodoscope at the DESY test beam facility. The hodoscope has a spatial resolution of 44 µm, which is better than the anticipated resolution of the TPC. The reference measurements with the hodoscope allow an accurate determination of the drift velocity and the absolute drift distance.

The alignment of the TPC and the hodoscope is determined from the data taken during dedicated calibration runs. After the calibration, the relative positioning is known within 3 µm in the x and 4 µm in the z direction.

By comparison with the hodoscope measurement, the homogeneity of the TPC's electric field has been determined. It was found that there is a deviation of 2.2 % from the nominal field near the readout. In the central region of the TPC no systematic deviation was found. However, there are fluctuations of $\Delta E/E = 8 \cdot 10^{-3}$ whose origin could not be established. To verify the design goal of $\Delta E/E \leq 10^{-4}$ the measurement has to be improved.

Distortion maps have been created from the systematic deviations between the TPC and the hodoscope measurements. It was found that the deviations in x direction are dependent on the drift distance and thus originate from distortions of the drift field. The deviations in z direction are mainly created within the GEM stack, as they are independent of the drift distance, but depend on the voltage settings of the GEMs. Correcting for the systematic distortions reduces the deviations to 50 ± 8 µm in the x and 81 ± 8 µm in the z direction, which is below the single point resolution of the TPC.

The spatial resolution has been measured for different gases. As the measurements were performed without magnetic field, the resolution is mainly determined by the diffusion. The best measured value is $s_x = 150 \pm 1$ µm for $Ar/CO_2/CH_4$ 93/2/5, which is the gas with the lowest transverse diffusion at 0 T.

As an example for a gas without hydrogen atoms in the quencher, Ar/CO_2 98/2 has been tested. This gas allows a stable operation of the TPC, although the fraction of quencher is only 2 %. It could be an interesting mixture if it turns out to be crucial to avoid hydrogen in the quencher gas because of neutron background. The best spatial resolution achieved with this gas mixture is $s_x = 180 \pm 1$ µm.

The measured spatial resolution in z for a drift distance of 10 cm is 246 ± 2 µm, which is far below the anticipated resolution of 600 µm for this drift distance, as

stated in the TESLA TDR. The fast preamplifiers which have been used together with the comparatively slow ADCs introduce a systematic bias. With enhanced electronics, the z resolution can even be improved.

GEM settings to minimise the backdrift of ions into the drift volume have been tested. It was suspected that these settings might degrade the spatial resolution due to a very low transfer field between two of the GEMs. The measurements show that this is not the case. The slightly degraded resolution in z can be explained by shortcomings of the electronics used.

The best resolution measured in a 4 T magnetic field is 124 ± 2 µm. As expected there is no significant degradation due to diffusion within the 260 mm drift distance for these measurements. However, the resolution is almost a factor of two larger than the TESLA design goal of 70 µm at 100 mm drift distance. The reason is that this data was not corrected for field distortions. The deviations near the readout plane and within the GEM stack introduce $E \times B$ effects, which degrade the resolution. To improve the results, these distortions have to be understood and eliminated first. Again the ion backdrift optimised GEM settings showed good performance. The slightly degraded resolution can be explained by the resolution limit due to the pad size used.

GEMs are promising candidates for gas amplification structures in TPCs, providing good ion backdrift suppression without degrading the spatial resolution. To reach the resolution required by the physics needs of the ILC, the field distortions have to be controlled and corrected. This is one of the tasks of a large TPC prototype currently under construction at DESY. It will allow simultaneous measurements with a TPC and a hodoscope in magnetic fields at a test beam facility.

A Chamber Settings and Gases

The following tables give an overview of the gases, magnetic fields and electrical settings of the TPC used for the measurements presented in the referenced figures. The gas mixture $Ar/CO_2/CH_4$ 93/2/5 was proposed in the TDR of the TESLA project and will be referred to as "TDR" gas below. Ar/CH_4 95/5 usually is called "P5". Ar/CO_2 98/2, also known as "Sagox 2", is abbreviated with "Sx2".

Chapter 5

Fig.	Gas	B [T]	E_{drift} [V/cm]	U_{GEM1} [V]	E_{trans1} [V/cm]	U_{GEM2} [V]	E_{trans2} [V/cm]	U_{GEM3} [V]	E_{ind} [V/cm]
5.3	TDR	0	240	310	2500	310	2500	310	5000

Chapter 6

Fig.	Gas	B [T]	E_{drift} [V/cm]	U_{GEM1} [V]	E_{trans1} [V/cm]	U_{GEM2} [V]	E_{trans2} [V/cm]	U_{GEM3} [V]	E_{ind} [V/cm]
6.10	TDR	0	240	310	2500	310	2500	310	5000
6.12	TDR	0	240	310	2500	310	2500	310	5000
6.13	TDR	0	240	310	2500	310	2500	310	5000
6.14	TDR	0	240	310	2500	310	2500	310	5000
6.15	TDR	0	240	310	2500	310	2500	310	5000
6.16	TDR	0	240	310	2500	310	2500	310	5000
6.17	Sx2	0	180	315	2500	315	2500	315	5000
6.18	Sx2	0	180	315	2500	315	2500	315	5000
6.19	Sx2	0	180	315	2500	315	2500	315	5000
6.23	Sx2	0	180	315	2500	315	2500	315	5000

A Chamber Settings and Gases

Chapter 7

Fig.	Gas	B [T]	E_{drift} [V/cm]	U_{GEM1} [V]	E_{trans1} [V/cm]	U_{GEM2} [V]	E_{trans2} [V/cm]	U_{GEM3} [V]	E_{ind} [V/cm]
7.2	TDR	0	80	310	2500	310	2500	310	5000
7.3	TDR	0	80	310	2500	310	2500	310	5000
7.4	TDR	0	80	310	2500	310	2500	310	5000
7.5	TDR	0	80	310	2500	310	2500	310	5000
7.6	TDR	0	240	310	2500	310	2500	310	5000
7.7	TDR	0	240	310	2500	310	2500	310	5000
7.8	Sx2	0	180	315	2500	315	2500	315	5000
	Sx2	0	180	315	4000	315	100	340	6000
7.9	TDR	0	240	310	2500	310	2500	310	5000
7.10	TDR	0	240	310	2500	310	2500	310	5000
7.11	TDR	0	240	310	2500	310	2500	310	5000
7.12	Sx2	0	180	315	2500	315	2500	315	5000

Chapter 8

Fig.	Gas	B [T]	E_{drift} [V/cm]	U_{GEM1} [V]	E_{trans1} [V/cm]	U_{GEM2} [V]	E_{trans2} [V/cm]	U_{GEM3} [V]	E_{ind} [V/cm]
8.1	TDR	0	240	328	4000	328	100	340	6000
8.2	TDR	0	240	328	4000	328	100	340	6000
8.4	TDR	0	240	310	2500	310	2500	310	5000
8.5	TDR	0	240	310	2500	310	2500	310	5000
	Sx2	0	180	315	2500	315	2500	315	5000
	P5	0	90	315	2500	315	2500	315	5000
8.6	TDR	0	240	310	2500	310	2500	310	5000
8.7(a)	TDR	0	240	310	2500	310	2500	310	5000
8.8	Sx2	0	180	315	2500	315	2500	315	5000
8.9	TDR	0	240	310	2500	310	2500	310	5000
	TDR	0	240	313	6000	314	60	350	8000
	TDR	0	240	328	4000	328	100	340	6000
8.10	Sx2	0	180	315	2500	315	2500	315	5000
	Sx2	0	180	315	4000	315	100	340	6000
8.11	Sx2	0	180	315	2500	315	2500	315	5000
	Sx2	0	180	315	4000	315	100	340	6000
8.12	TDR	4	240	310	2500	310	2500	310	5000
8.13	TDR	4	240	310	2500	310	2500	310	5000
	TDR	4	240	300	4000	300	100	340	6000

B Data Structures and Classes

B.1 Raw Data Format

The raw data file format is a simple binary data format. Its file header contains only one byte, describing the number of TPDs used. After the file header, the events are written consecutively. The event size depends on the number of TPDs n. Each event has a time stamp (long integer with big-endian byte order) and 512 bytes per channel, 64 channels per TPD.

File Header		
Number of Bytes	Type	Description
1	unsigned char	Number of TPDs (n)

Event		
Number of Bytes	Type	Description
4	unsigned long	Unix time
$n \cdot 64 \cdot 512$	unsigned char	Raw data of all channels

B.2 Zero Suppressed Raw Data (ZSR)

The zero suppressed raw data (ZSR) format is a binary data format with big-endian byte order. The file starts with a file header, followed by the events. Each event consists of an event header, followed by the hit data.

File Header		
Number of Bytes	Type	Description
4	unsigned long	Length of header in bytes (incl. these 4)
1	unsigned char	Number of TPDs (n)
$n \cdot 64 \cdot 8$	2 · float	Pedestals and sigma of pedestals
1	unsigned char	Cut for threshold (number of sigmas)
1	unsigned char	Type of checksum (0 = nr. of bytes, 1 = crc32)

Event Header		
Number of Bytes	Type	Description
1	unsigned char	NULL byte for syncing (0x0)
4	unsigned long	Checksum
1	unsigned char	NULL byte for syncing (0x0)
4	unsigned long	Unix time
4	unsigned long	Microseconds of Unix time
4	unsigned long	Trigger number
2	unsigned short	Number of hits

Hit		
Number of Bytes	Type	Description
2	unsigned short	Channel number
1	unsigned char	Number of time samples (s)
2	unsigned short	First time sample
s	unsigned char	Sampled data

B.3 Peaks

Each peak corresponds to one hit on a specific channel. The peaks do not contain a channel number, but are saved in a channel class which contains the channel number and an array of peaks.

TPCPeak			
Type	Name	Description	Unit
int	SumQ	Sum of charge in peak	ADC counts
int	EdgeQ	First ADC value above threshold	ADC counts
int	MaxQ	Maximum ADC value in peak	ADC counts
float	AvTime	Average time of peak	Time samples
int	EdgeTime	Time of first bin above threshold	Time samples
int	MaxTime	Time of maximum ADC value	Time samples
int	PeakWidth	Width of peak	Time Samples
int	NumberOfParticles	Number of Particles that contributed to peak (simulation)	
int	ParticleNr	Particle number of first generator particle (simulation)	

B.4 Points

TPCPoint			
Type	Name	Description	Unit
float	X	x coordinate	mm
float	Y	y coordinate	mm
float	Z	z coordinate	mm or µs
float	Q	Charge	ADC counts
int	NPads	Number of pads that contributed to point	
float	SigmaX	Error on the x coordinate	mm
float	SigmaZ	Error on the z coordinate	mm
int	QualityFlags	Quality flags of the point	

B.5 Straight Tracks

The straight line describing the track is parameterised by the slope and an axis intercept in the xy and in the zy projection.

TPCTrack			
Type	Name	Description	Unit
int	NTrackPoints	Number of points on the track	
TPCPOINT[ ]	TrackPoints	Array of TPCPOINTs on the track	
float	a	Slope in the xy projection	
float	b	x axis intercept in the xy plane	mm
float	c	Slope in the zy projection	1 or µs/mm
float	d	z axis intercept in the zy plane	mm or µs
float	SigmaX	Mean x distance of the measured points to the straight line	mm
float	SigmaZ	Mean z distance of the measured points to the straight line	mm
int	FitAlgorithm	Number of fit algorithm used	
int	FitQuality	Status flag for the fit quality	
int	BadPointsMask	Bit mask describing which point flags to be taken into account	
int	NValidPoints	Number of points which are valid according to BadPointsMask	

(a) Projection of a helix onto the xy plane.

(b) Projection of a helix onto the sz plane.
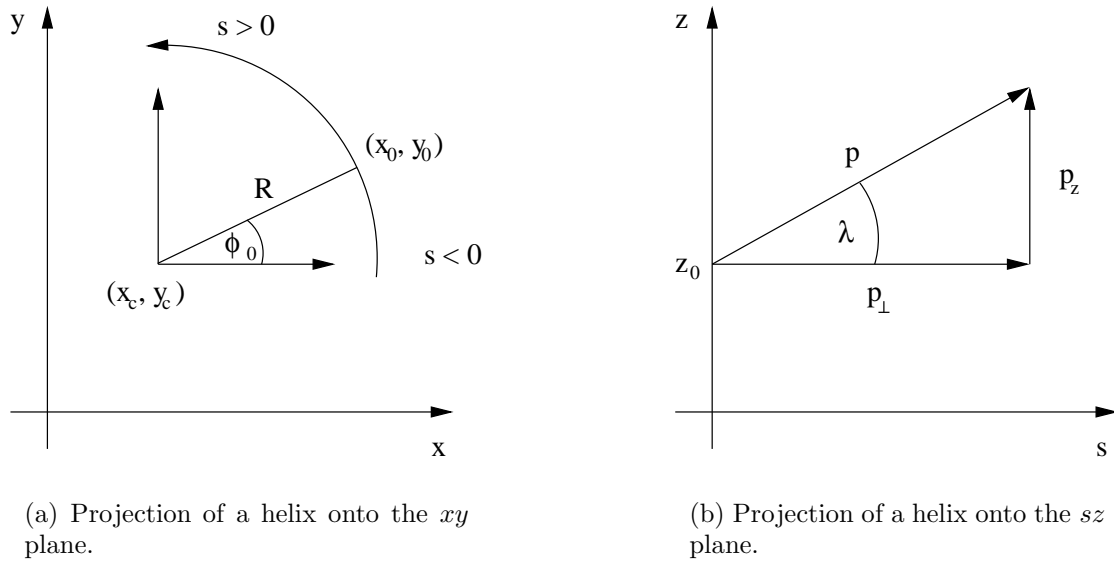
Figure B.1: Visualisation of the helix parameters.

B.6 Helixes

The helix parameters were chosen according to [73]:

$$
\begin{aligned}
x(s) &= x_0 + \frac{1}{|\kappa|}\left[\cos\left(\phi_0 + s\kappa\cos\lambda\right) - \cos\phi_0\right] \\
y(s) &= y_0 + \frac{1}{|\kappa|}\left[\sin\left(\phi_0 + s\kappa\cos\lambda\right) - \sin\phi_0\right] \\
z(s) &= z_0 + s\sin\lambda
\end{aligned}
$$

The helix is parameterised along its path length s. Its parameters are visualised in figure B.1. TPCHelixTrack is derived from TPCTrack, so all the track properties like the number of points, the points array, fit quality etc. are available.

TPCHelixTrack			
Type	Name	Description	Unit
double	X_0	x coordinate of the starting point	mm
double	Y_0	y coordinate of the starting point	mm
double	Z_0	z coordinate of the starting point	mm or µs
double	Kappa	Signed curvature of the helix ($1/|\kappa|$=R)	1/mm
double	Lambda	Dip angle in the sz plane, i. e. $\arctan\left(p_z/p_\perp\right)$	rad[1]
double	Phi_0	Azimuth angle of the starting point w. r. t. the helix axis	rad

---

[1] If the z coordinate of the track is given in µs, the unit of λ is undefined. In calculations usually $\tan(\lambda)$ is used, which then is in units of µs/mm.

C Parametrisation of the Drift Velocity
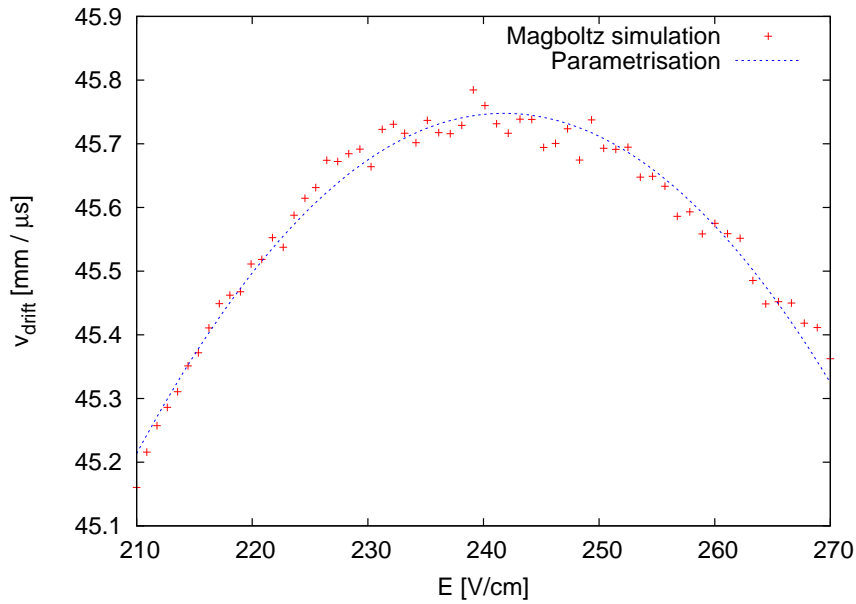
Figure C.1: The drift velocity of TDR gas around its maximum at 240 V/cm has been approximated by a parabola.

The dependence of the drift velocity on the electric field is small at the maximum of the drift velocity. To get an estimate of the influence of small field distortions in the spatial resolution, the drift velocity of TDR gas has been simulated in the area around 240 V/cm. In the range from 210 V/cm to 270 V/cm the distribution can be approximated by a parabola (figure C.1).

$$v_{\mathrm{drift}}(E) = aE^2 + bE + c$$

The fitted parameters are:

$$a \;=\; -53.0 \cdot 10^{-5} \pm 1.2 \cdot 10^{-5} \, \frac{\mathrm{mm}}{\upmu\mathrm{s}} \left(\frac{\mathrm{V}}{\mathrm{cm}} \right)^{-2}$$

$$b \;=\; 0.256 \pm 0.006 \, \frac{\mathrm{mm}}{\upmu\mathrm{s}} \left(\frac{\mathrm{V}}{\mathrm{cm}} \right)^{-1}$$

$$c \;=\; 14.8 \pm 0.7 \, \frac{\mathrm{mm}}{\upmu\mathrm{s}}$$

C Parametrisation of the Drift Velocity

D Bias of the Centre of Gravity Method

Throughout the present work all data has been reconstructed calculating the centre of gravity of the measured signals. This method introduces a bias, as mentioned several times. As an example, this effect is studied for a charge cloud being recorded on a pad plane.

The charge cloud with the total charge Q is mapped onto the pads. The charge density function is assumed to be Gaussian shaped:

$$\rho(x) = \frac{Q}{\sigma\sqrt{2\pi}}e^{-\frac{(x-\mu)^2}{2\sigma^2}}$$

The resulting charge deposition on pad number i is

$$q_i = \int\limits_{x_{\min_i}}^{x_{\max_i}} \rho(x)\,\mathrm{d}x = \frac{1}{2}\left(\mathrm{erf}\left(\frac{x_{\max_i} - \mu}{\sqrt{2}\sigma}\right) - \mathrm{erf}\left(\frac{x_{\min_i} - \mu}{\sqrt{2}\sigma}\right)\right)$$

$x_{\min_i}$ is the left edge of the pad, $x_{\max_i}$ the right one. The distribution of the charge across the pads is usually referred to as *pad response*. The density distribution and the pad response are shown in figure D.1.

From the pad response the sought-after coordinate has to be calculated. In this case it is the mean value of the Gaussian distribution μ. The reconstruction method used in this work calculates the centre of gravity of the charge:

$$\bar{x} = \frac{\sum\limits_i q_i x_i}{\sum\limits_i q_i}$$

x_i is the centre of pad number i. If the width σ of the charge distribution is significantly smaller than the pad width, $\bar{x}$ is biased towards the centre of the pad which received the largest amount of charge. The reconstructed coordinate versus the centre of the original charge distribution is shown in figure D.2. One can see that the bias is largest for small widths of the charge cloud. With increasing width, the function approaches a straight line. If the charge distribution is broad enough to deposit a significant amount of charge on at least four or five pads, the bias is negligible.

To reconstruct the correct coordinate from the pad response for the case that two or three pads are hit, the charge distribution function has to be known. The real
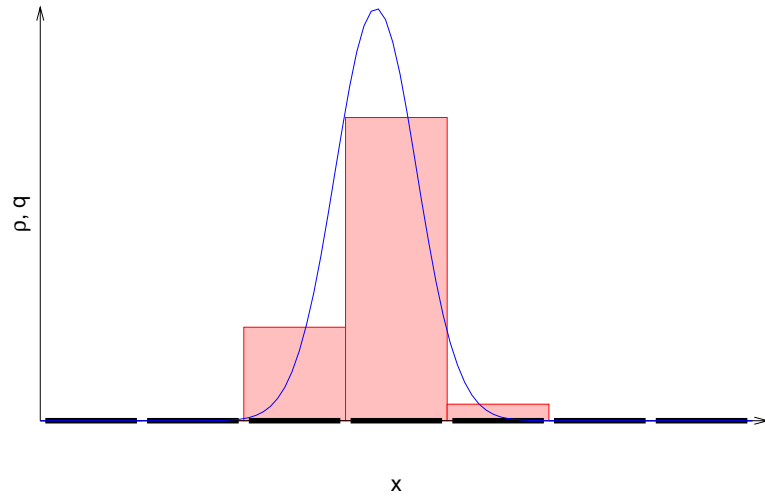
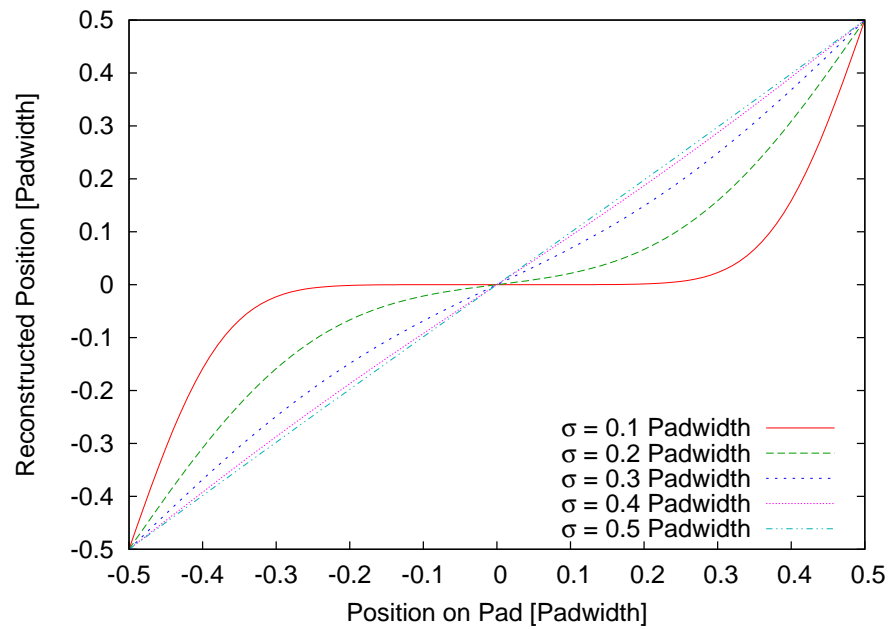Figure D.1: A Gaussian distribution and its integral on each pad.

Figure D.2: The reconstructed coordinate versus the original position in dependence on the width of the charge cloud.

pad response function is more complicated than the integral shown above. On the one hand, the charge is not Gaussian distributed, due to statistical fluctuations in the gas amplification of a GEM stack. On the other hand the signal is sampled using an ADC, which has a limited resolution and a threshold to cut away noise. This also cuts off part of the signal.

A bias due to the centre of gravity reconstruction method always occurs if a distribution is mapped into discrete bins. For instance if a pulse is sampled with an ADC, the signal is binned into time slices. If the signal has a length of only two or three time samples, the reconstructed time is biased towards the centre of the bin with the largest ADC value. This leads to a dependence on the phase between signal and ADC clock, as shown in section 8.2.2.

D Bias of the Centre of Gravity Method

Bibliography

[1] David Griffiths. *Introduction to Elementary Particles*. Wiley, 1987.

[2] Michael E. Peskin and Daniel V. Schroeder. *An Introduction to Quantum Field Theory*. Addison Wesley, 1995.

[3] E. Abers and B. Lee. Gauge theories. *Phys. Rept.*, 9:1–2, November 1973. doi:10.1016/0370-1573(73)90027-6.

[4] S. L. Glashow. Partial symmetries of weak interactions. *Nucl. Phys.*, 22:579–588, 1961. doi:10.1016/0029-5582(61)90469-2.

[5] Abdus Salam and J. C. Ward. Electromagnetic and weak interactions. *Phys. Lett.*, 13:168–171, 1964.

[6] Steven Weinberg. A model of leptons. *Phys. Rev. Lett.*, 19:1264–1266, 1967. doi:10.1103/PhysRevLett.19.1264.

[7] W.-M. Yao et al. Review of Particle Physics. *Journal of Physics G*, 33, 2006. http://pdg.lbl.gov/, doi:10.1088/0954-3899/33/1/001.

[8] M. C. Gonzalez-Garcia and Y. Nir. Neutrino masses and mixing: Evidence and implications. *Reviews of Modern Physics*, 75:345, 2003. oai:arXiv.org:hep-ph/0202058.

[9] Y. Ashie et al. Evidence for an oscillatory signature in atmospheric neutrino oscillation. *Phys. Rev. Lett.*, 93:101801, 2004. oai:arXiv.org:hep-ex/0404034.

[10] A. Tapper. High Q^2 neutral current cross sections in e+p DIS. Talk given at the 12th International Workshop on Deep Inelastic Scattering, Strbske Pleso, Slovakia, 2004.

[11] Peter W. Higgs. Broken symmetries, massless particles and gauge fields. *Phys. Lett.*, 12:132–133, 1964. doi:10.1016/0031-9163(64)91136-9.

[12] Peter W. Higgs. Broken symmetries and the masses of gauge bosons. *Phys. Rev. Lett.*, 13(16):508–509, Oct 1964. doi:10.1103/PhysRevLett.13.508.

[13] Peter W. Higgs. Spontaneous symmetry breakdown without massless bosons. *Phys. Rev.*, 145(4):1156–1163, May 1966. doi:10.1103/PhysRev.145.1156.

Bibliography

[14] R. Barate et al. Search for the standard model higgs boson at lep. *Phys. Lett.*, B565:61–75, 2003. doi:10.1016/S0370-2693(03)00614-2.

[15] Howard E. Haber and Gordon L. Kane. The search for supersymmetry: Probing physics beyond the standard model. *Phys. Rept.*, 117:75, 1985. doi:10.1016/0370-1573(85)90051-1.

[16] Hans Peter Nilles. Supersymmetry, supergravity and particle physics. *Phys. Rept.*, 110:1, 1984. doi:10.1016/0370-1573(84)90008-5.

[17] Koya Abe et al. GLC Project Report, May 2003. http://lcdev.kek.jp/RMdraft/.

[18] The LNC Design Group. Zeroth-Order Design Report for the Next Linear Collider, 1996. NBNL-5424, SLAC-R-474, UCRL-ID-124161, UC-414.

[19] TESLA technical design report, 2001. DESY 2001-011, ECFA 2001-209.

[20] International Technology Recommendation Panel. Executive summary, 2004. http://www.interactions.org/pdf/ITRPexec.pdf.

[21] ILC Global Design Effort. *The International Linear Collider Baseline Configuration Document*, 2006.
http://www.linearcollider.org/wiki/doku.php?id=bcd:bcd_home.

[22] TESLA technical design report, part III "Physics at an e^+e^- Linear Collider", 2001. DESY 2001-011, ECFA 2001-209, oai:arXiv.org:hep-ph/0106315.

[23] TESLA technical design report, part IV "A Detector for TESLA", 2001. DESY 2001-011, ECFA 2001-209.

[24] P. Le Du et al. Detector Outline Document for the Fourth Concept Detector ("4th") at the International Linear Collider, 2006. http://www.physics.iastate.edu/getfiles/1965.pdf.

[25] GLD : a large detector concept study for ILC. http://ilcphys.kek.jp/gld/.

[26] GLD Concept Study Group. *GLD Detector Outline Document, Version 1.2*, July 2006. oai:arXiv.org:physics/0607154.

[27] The LDC web site. http://www.ilcldc.org/.

[28] LDC Working Group. *Detector Outline Document for the Large Detector Concept*, July 2006. http://www.ilcldc.org/documents/dod/.

[29] Silicon Detector Design Study. http://www-sid.slac.stanford.edu/.

[30] T. Abe et al. *SiD Detector Outline Document*, May 2006. http://hep.uchicago.edu/~oreglia/siddod.pdf.

[31] A Fourth Concept Detector. http://www.4thconcept.org/.

[32] Chris Bowdery, editor. *The ALEPH Handbook.* CERN, 1995. http://aleph.web.cern.ch/aleph/handbook/.

[33] P. A. Aarnio et al. The delphi detector at lep. *Nucl. Instrum. Meth.*, A303:233–276, 1991. doi:10.1016/0168-9002(91)90793-P.

[34] M. Anderson et al. The star time projection chamber: A unique tool for studying high multiplicity events at rhic. *Nucl. Instrum. Meth.*, A499:659–678, 2003. doi:10.1016/S0168-9002(02)01964-2.

[35] Y. Giomataris, P. Rebourgeard, J. P. Robert, and Georges Charpak. Micromegas: A high-granularity position-sensitive gaseous detector for high particle-flux environments. *Nucl. Instrum. Meth.*, A376:29–35, 1996. doi:10.1016/0168-9002(96)00175-1.

[36] F. Sauli. Gem: A new concept for electron amplification in gas detectors. *Nucl. Instrum. Meth.*, A386:531–534, 1997. doi:10.1016/S0168-9002(96)01172-2.

[37] The T2K ND280 TPC Group. T2K ND280 TPC technical design report. in preparation.

[38] D. R. Nygren. The time projection chamber: A new 4 pi detector for charged particles. PEP-0144.

[39] W. Blum and L Rolandi. *Particle Detection with Drift Chambers.* Springer-Verlag, 1993.

[40] Claus Grupen. *Teilchendetektoren.* BI-Wissenschaftsverlag, 1993.

[41] C. Ramsauer. Über den Wirkungsquerschnitt der Gasmoleküle gegenüber langsamen Elektronen. *Annalen der Physik*, 66:546, 1921.

[42] W. P. Allis and P. M. Morse. Theorie der Streuung langsamer Elektronen an Atomen. *Zeitschrift für Physik A*, 70:567, 1931.

[43] M. Gruwè. Gas studies for a TPC of a detector for the future Linear Collider TESLA, 1999. LC-DET-1999-003-TESLA.

[44] Stephen Biagi. *Magboltz: Transport of electrons in gas mixtures.* http://consult.cern.ch/writeup/magboltz/.

[45] COMSOL Multiphysics. http://www.comsol.com/products/multiphysics/.

[46] Homepage of the Gas Detectors Development Group at CERN. http://gdd.web.cern.ch/GDD/.

Bibliography

[47] Rob Veenhof. *Garfield - simulation of gaseous detectors.* http://consult.cern.ch/writeup/garfield/.

[48] P. Colas, I. Giomataris, and V. Lepeltier. Ion backflow in the Micromegas TPC for the future linear collider. *Nucl. Instrum. Meth.*, A535:226–230, 2004. doi:10.1016/j.nima.2004.07.274.

[49] M. Killenberg et al. Charge transfer and charge broadening of gem structures in high magnetic fields. *Nucl. Instrum. Meth.*, A530:251–257, 2004. doi:10.1016/j.nima.2004.04.241.

[50] Blanka Sobloher. *Simulationsstudien zu GEM-Folien für die Auslese einer TPC.* Diploma thesis, RWTH Aachen, 2002. http://www.physik.rwth-aachen.de/group/IIIphys/TPC/.

[51] M. Killenberg et al. Modelling and measurement of charge transfer in multiple GEM structures. *Nucl. Instrum. Meth.*, A498:369–383, 2003. doi:10.1016/S0168-9002(02)02079-X.

[52] Sven Lotze. *Ion Backdrift Minimisation in a GEM-Based TPC Readout.* PhD thesis, RWTH Aachen, 2006. urn:nbn:de:hbz:82-opus-14999.

[53] Sabine Blatt. *Konstruktion und Inbetriebnahme eines Feldkäfigs für eine TPC.* Diploma thesis, RWTH Aachen, 2004. http://www.physik.rwth-aachen.de/group/IIIphys/TPC/.

[54] M. Raymond et al. *PreShape32 User Manual, Version 1.1*, Mai 1995.

[55] Creative Electronics Systems S. A., Geneva. *VFI 9214 VICbus to FASTBUS Interface, User's Manual ver. 1.1.*

[56] Andreas Nowak. *HV Channel Control Class, Version 1.2.* III. Physikalisches Institut, RWTH Aachen, 1999.

[57] Sensirion AG. *SHT1x/SHT7x Humidity & Temperature Sensor*, 2003. http://www.sensirion.com/.

[58] Fujikura Ltd. *XFPM, FXAM Data Sheet*, 2004. http://www.fujikura.co.jp/.

[59] F. Beißel. *Cooli — Cold Box Control Serial Interface, Version 2.0 Draft.* RWTH Aachen, 2003.

[60] Manuel Giffels. *Entwicklung der Auslesesoftware für den Kalibrationsteststand einer TPC.* Diploma thesis, RWTH Aachen, 2005. http://www.physik.rwth-aachen.de/group/IIIphys/TPC/.

[61] Peter Wienemann. Private communication.

[62] Matthias Enno Janssen. *Resolution studies of a time projection chamber using a GEM gas amplification system. (In German).* Diploma thesis, DESY, 2004. DESY-THESIS-2004-049.

[63] Rene Brun and Fons Rademakers. *The ROOT System Homepage.* http://root.cern.ch/.

[64] W. Walcher. *Praktikum der Physik.* Teubner Taschenbücher Physik, 1994.

[65] M. Axer, F. Beißel, C. Camps, V. Commichau, and K. Hangarter. *ARC — A very simple to use* **A***PV* **R***eadout* **C***ontroler.* RWTH Aachen, 2002. http://www.physik.rwth-aachen.de/group/IIIphys/CMS/tracker/manuals/arc.pdf.

[66] F. Beißel. *DEPP Version 1.0.* RWTH Aachen, 2002. http://www.physik.rwth-aachen.de/group/IIIphys/CMS/tracker/en/silicon/hvboard.html.

[67] Gordon Kaussen. *Aufbau eines Hodoskops aus Siliziumstreifendetektoren.* Diploma thesis, RWTH Aachen, 2005. http://www.physik.rwth-aachen.de/group/IIIphys/TPC/.

[68] *DESY Test Beam Homepage.* http://testbeam.desy.de/.

[69] R. K. Carnegie, M. S. Dixit, J. Dubeau, D. Karlen, J. P. Martin, H. Mes, and K. Sachs. Resolution studies of cosmic-ray tracks in a TPC with GEM readout. *NUCL.INSTRUM.METH.A*, 538:372, 2004. doi:10.1016/j.nima.2004.08.132.

[70] Astrid Münnich. *TPCGEMSimulation.* RWTH Aachen, http://www.physik.rwth-aachen.de/group/IIIphys/TPC/en/software/.

[71] Astrid Münnich. *Simulation Studies for a High Resolution Time Projection Chamber at the International Linear Collider.* PhD thesis, RWTH Aachen, in preparation.

[72] EUDET: Detector R&D towards the International Linear Collider. http://www.eudet.org/.

[73] Brian Lasiuk, Dan Lyons, and Thomas Ullrich. Track parametrisation. Technical report, Physics Department, Yale University, February 1998.

Bibliography

Acknowledgements

Lebenslauf

Martin Killenberg

Persönliche Daten:

Geburtsdatum	27. 10. 1974
Geburtsort	Soest

Schulbildung:

1981 bis 1985	Grundschule Hirschberg
1985 bis 1994	Gymnasium der Stadt Warstein
	Schulabschluss Abitur

Wehrdienst:

1994 bis 1995	Grundwehrdienst im
	Transportbataillon 801 Lippstadt

Studium:

1995 bis 2002	Physikstudium an der RWTH Aachen
	Abschluss Diplom
	Diplomarbeit: „*Inbetriebnahme und Datenauslese einer TPC*"
2002 bis 2006	Promotionsstudium an der RWTH Aachen